PDRs4All III: JWST's NIR spectroscopic view of the Orion Bar

Els Peeters, Emilie Habart, Olivier Berné, Ameek Sidhu, Ryan Chown, Dries van de Putte, Boris Trahin, Ilane Schroetter, Amélie Canin, Felipe Alarcón, et al.

A&A, 685, A74 (2024)
https://doi.org/10.1051/0004-6361/202348244

Astronomy & Astrophysics

PDRs4All

III. JWST's NIR spectroscopic view of the Orion Bar★

Els Peeters[1,2,3], Emilie Habart[4], Olivier Berné[5], Ameek Sidhu[1,2], Ryan Chown[1,2], Dries Van De Putte[6], Boris Trahin[4], Ilane Schroetter[5], Amélie Canin[5], Felipe Alarcón[7], Bethany Schefter[1,2], Baria Khan[1], Sofia Pasquini[1], Alexander G. G. M. Tielens[8,9], Mark G. Wolfire[9], Emmanuel Dartois[10], Javier R. Goicoechea[11], Alexandros Maragkoudakis[12], Takashi Onaka[13,14], Marc W. Pound[9], Sílvia Vicente[15], Alain Abergel[4], Edwin A. Bergin[7], Jeronimo Bernard-Salas[16,17], Christiaan Boersma[12], Emeric Bron[18], Jan Cami[1,2,3], Sara Cuadrado[11], Daniel Dicken[19], Meriem Elyajouri[4], Asunción Fuente[20], Karl D. Gordon[6,21], Lina Issa[5], Christine Joblin[5], Olga Kannavou[4], Ozan Lacinbala[22], David Languignon[18], Romane Le Gal[23,24], Raphael Meshaka[4,18], Yoko Okada[25], Massimo Robberto[6,26], Markus Röllig[27,28], Thiébaut Schirmer[4,29], Benoit Tabone[4], Marion Zannese[4], Isabel Aleman[30,31,32], Louis Allamandola[12,33], Rebecca Auchettl[34], Giuseppe Antonio Baratta[35], Salma Bejaoui[12], Partha P. Bera[12,33], John H. Black[29], Francois Boulanger[36], Jordy Bouwman[37,38,39], Bernhard Brandl[8,40], Philippe Brechignac[10], Sandra Brünken[41], Mridusmita Buragohain[42], Andrew Burkhardt[43], Alessandra Candian[44], Stéphanie Cazaux[45], Jose Cernicharo[11], Marin Chabot[46], Shubhadip Chakraborty[47,48], Jason Champion[5], Sean W. J. Colgan[12], Ilsa R. Cooke[49], Audrey Coutens[5], Nick L. J. Cox[16,17], Karine Demyk[5], Jennifer Donovan Meyer[50], Sacha Foschino[5], Pedro García-Lario[51], Maryvonne Gerin[52], Carl A. Gottlieb[53], Pierre Guillard[54,55], Antoine Gusdorf[36,52], Patrick Hartigan[56], Jinhua He[57,58,98], Eric Herbst[59], Liv Hornekaer[60], Cornelia Jäger[61], Eduardo Janot-Pacheco[62], Michael Kaufman[63], Sarah Kendrew[64], Maria S. Kirsanova[65], Pamela Klaassen[19], Sun Kwok[66], Álvaro Labiano[67], Thomas S.-Y. Lai[68], Timothy J. Lee[12,†], Bertrand Lefloch[69], Franck Le Petit[18], Aigen Li[70], Hendrik Linz[71], Cameron J. Mackie[72,73], Suzanne C. Madden[74], Joëlle Mascetti[75], Brett A. McGuire[50,76], Pablo Merino[77], Elisabetta R. Micelotta[78], Karl Misselt[79], Jon A. Morse[80], Giacomo Mulas[99,5], Naslim Neelamkodan[81], Ryou Ohsawa[82], Roberta Paladini[68], Maria Elisabetta Palumbo[35], Amit Pathak[83], Yvonne J. Pendleton[84], Annemieke Petrignani[85], Thomas Pino[10], Elena Puga[64], Naseem Rangwala[12], Mathias Rapacioli[86], Alessandra Ricca[12,3], Julia Roman-Duval[6], Joseph Roser[3,12], Evelyne Roueff[18], Gaël Rouillé[61], Farid Salama[12], Dinalva A. Sales[87], Karin Sandstrom[88], Peter Sarre[89], Ella Sciamma-O'Brien[12], Kris Sellgren[90], Sachindev S. Shenoy[91], David Teyssier[51], Richard D. Thomas[92], Aditya Togi[93], Laurent Verstraete[4], Adolf N. Witt[94], Alwyn Wootten[50], Nathalie Ysard[4], Henning Zettergren[92], Yong Zhang[95], Ziwei E. Zhang[96], and Junfeng Zhen[97]

(Affiliations can be found after the references)

Received 12 October 2023 / Accepted 22 December 2023

ABSTRACT

Context. JWST has taken the sharpest and most sensitive infrared (IR) spectral imaging observations ever of the Orion Bar photodissociation region (PDR), which is part of the nearest massive star-forming region the Orion Nebula, and often considered to be the 'prototypical' strongly illuminated PDR.

Aims. We investigate the impact of radiative feedback from massive stars on their natal cloud and focus on the transition from the H II region to the atomic PDR – crossing the ionisation front (IF) –, and the subsequent transition to the molecular PDR – crossing the dissociation front (DF). Given the prevalence of PDRs in the interstellar medium and their dominant contribution to IR radiation, understanding the response of the PDR gas to far-ultraviolet (FUV) photons and the associated physical and chemical processes is fundamental to our understanding of star and planet formation and for the interpretation of any unresolved PDR as seen by JWST.

Methods. We used high-resolution near-IR integral field spectroscopic data from NIRSpec on JWST to observe the Orion Bar PDR as part of the PDRs4All JWST Early Release Science programme. We constructed a 3″ × 25″ spatio-spectral mosaic covering 0.97–5.27 μm at a spectral resolution R of ∼2700 and an angular resolution of 0.075″–0.173″. To study the properties of key regions captured in this mosaic, we extracted five template spectra in apertures centred on the three H_2 dissociation fronts, the atomic PDR, and the H II region. This wealth of detailed spatial-spectral information was analysed in terms of variations in the physical conditions–incident UV field, density, and temperature – of the PDR gas.

★ Full Table 3, a table with line intensities for the five template spectra (Table B.1), and the five template spectra are available at the CDS via anonymous ftp to cdsarc.cds.unistra.fr (130.79.128.5) or via https://cdsarc.cds.unistra.fr/viz-bin/cat/J/A+A/685/A74

† Tim Lee sadly passed away on Nov. 3 2022.

Results. The NIRSpec data reveal a forest of lines including, but not limited to, He I, H I, and C I recombination lines; ionic lines (e.g. Fe III and Fe II); O I and N I fluorescence lines; aromatic infrared bands (AIBs, including aromatic CH, aliphatic CH, and their CD counterparts); pure rotational and ro-vibrational lines from H_2; and ro-vibrational lines from HD, CO, and CH^+, with most of them having been detected for the first time towards a PDR. Their spatial distribution resolves the H and He ionisation structure in the Huygens region, gives insight into the geometry of the Bar, and confirms the large-scale stratification of PDRs. In addition, we observed numerous smaller-scale structures whose typical size decreases with distance from θ^1 Ori C and IR lines from C I , if solely arising from radiative recombination and cascade, reveal very high gas temperatures (a few 1000 K) consistent with the hot irradiated surface of small-scale dense clumps inside the PDR. The morphology of the Bar, in particular that of the H_2 lines, reveals multiple prominent filaments that exhibit different characteristics. This leaves the impression of a 'terraced' transition from the predominantly atomic surface region to the CO-rich molecular zone deeper in. We attribute the different characteristics of the H_2 filaments to their varying depth into the PDR and, in some cases, not reaching the C^+/C/CO transition. These observations thus reveal what local conditions are required to drive the physical and chemical processes needed to explain the different characteristics of the DFs and the photochemical evolution of the AIB carriers.
Conclusions. This study showcases the discovery space created by JWST to further our understanding of the impact radiation from young stars has on their natal molecular cloud and proto-planetary disk, which touches on star and planet formation as well as galaxy evolution.

Keywords: techniques: spectroscopic – HII regions – photon-dominated region (PDR) – infrared: ISM – ISM: individual objects: Orion Bar

1. Introduction

Massive stars output enormous amounts of radiative and mechanical energy into the interstellar medium (ISM) during their main sequence lifetimes. This energy injection shapes the global properties of the ISM, such as its structure, thermal balance, chemistry, and ionisation state. Negative stellar feedback plays a critical role in secular galaxy evolution as it suppresses star formation (Williams & McKee 1997; Hopkins et al. 2012; Kim et al. 2013), while positive stellar feedback results in swept-up gas and dust from which future stars can form (e.g. Elmegreen & Lada 1977; Preibisch & Zinnecker 1999; Koenig et al. 2008; Kirsanova et al. 2008; Ojha et al. 2011; Egorov et al. 2014, 2017).

This radiative and mechanical feedback from massive stars ionises their natal molecular cloud and creates an H II region. Photodissociation regions[1] (PDRs) are the transition from this H II region to the cold molecular cloud. While extreme-ultraviolet (EUV) radiation (>13.6 eV) dominates the photoionised layers, the stellar far-ultraviolet (FUV) radiation (6–13.6 eV) drives the physical and chemical processes in PDRs (Tielens & Hollenbach 1985a,b).

Most of the interaction between massive stars and their surroundings occurs in PDRs. While PDRs were initially associated with young massive stars (Tielens & Hollenbach 1985a), PDRs are also found in the diffuse ISM (Wolfire et al. 2003), reflection nebulae (e.g. Burton et al. 1990; Sheffer et al. 2011), planetary nebulae (Bernard-Salas & Tielens 2005), surfaces of proto-planetary disks (Vicente et al. 2013), pillars (McLeod et al. 2015), globules (Reiter et al. 2019), and molecular clouds. PDRs produce a significant fraction of the ISM radiative emission of galaxies, in particular in star-forming galaxies, (ultra-)luminous IR galaxies (ULIRGs), and galactic nuclei. The neutral ISM and most of the molecular ISM, where most of the ISM mass is found, does indeed reside in PDRs (Wolfire et al. 2022). Consequently, understanding PDRs is a key prerequisite for understanding star and planet formation and the large-scale ecology of the ISM of galaxies and its relationship to galaxy evolution.

The large-scale PDR structure is stratified with temperatures decreasing from 10^4 at the front surface of the PDR to a few hundreds of Kelvin in the atomic PDR, and, crossing the H_2 dissociation front, to a few tens of Kelvin deep into the molecular PDR. While models have been very successful in explaining the observed large-scale structure of PDRs (Tielens & Hollenbach 1985b; Sternberg & Dalgarno 1989; Abgrall et al. 1992; Le Bourlot et al. 1993; Röllig et al. 2007; Wolfire et al. 2022), recent high-angular resolution Atacama large millimeter/submillimeter array (ALMA) and Keck observations have revealed a varying PDR front and highly structured PDR (Goicoechea et al. 2016; Habart et al. 2023). The highly structured nature of the molecular PDR layers betrays the dynamic action of the evaporation flow that advects material from the molecular cloud, through the PDR and the ionisation front, into the ionised gas (Bertoldi & Draine 1996; Störzer & Hollenbach 1998; Henney et al. 2007). Hence, observations at a high angular resolution are required to resolve the small-scale structure to fully understand the processes responsible for shaping PDRs.

Observations at infrared (IR) wavelengths are key in understanding PDRs. Infrared spectra of PDRs are indeed extremely rich – they feature a plethora of strong H I recombination lines, fine-structure lines from atomic and ionised gas, rotational and ro-vibrational emission from H_2 and other small molecules, as well as broad emission bands commonly referred to as aromatic infrared bands (AIBs), all superimposed on undulating continuum emission. We note that some of this emission originates in the photoionised regions along the line of sight, rather than the PDR itself. This spectral diversity provides ample diagnostics to characterise the physical and chemical anatomy of PDRs and to characterise the photochemical evolution of molecules and dust (e.g. Marconi et al. 1998; Luhman et al. 1998; Walmsley et al. 2000; Sheffer et al. 2011; Pilleri et al. 2012; Habart et al. 2023). However, past IR observations had an insufficient angular resolution to resolve the small-scale structure of PDRs or were limited by the spectral resolution and/or wavelength coverage or both. The unprecedented capabilities of JWST allow, for the first time, for high spatial resolution (0.075″ to 0.173″) to be combined with medium spectral resolution and large IR wavelength coverage for PDR studies. Such observations thus provide the critical PDR diagnostics at an angular resolution that enables the highly structured PDR anatomy to be probed and the intricate combination of physical, chemical, and dynamical processes at play in shaping the PDR anatomy to be investigated.

[1] Also sometimes called 'photon-dominated regions' (e.g. Sternberg & Dalgarno 1995).

The PDRs4All Early Release Science (ERS) programme (ID1288)[2] fully exploits JWST's angular resolution by observing the nearest massive star-forming region, the Orion Nebula, in the NIRCam and MIRI imaging mode and NIRSpec and MIRI spectral mapping mode (Berné et al. 2022). This unique data set will serve as the reference data set for PDRs in the next decades and will facilitate the interpretation of numerous JWST observations. Indeed, given the prevalence of PDRs in the Universe and the strong IR emission of PDRs, much of the emission (to be) observed by JWST is from (unresolved) PDRs.

This work presents the first analysis of the PDRs4All NIRSpec data set and accompanies the PDRs4All NIRCam and MIRI imaging paper (Habart et al. 2024), the NIRSpec proplyd paper (Berné et al. 2024), the MIRI MRS PAH paper (Chown et al. 2024), and the MIRI MRS gas lines paper (Van De Putte et al. 2024). This paper is organised as follows. First, we describe the characteristics of the PDR, the Bar, as deduced from earlier studies in Sect. 2. This is followed by a description of the observations, data reduction and flux measurements in Sect. 3. A spectral inventory and line intensity list are given in Sect. 4.1 and Appendix B. Then, we discuss the spatial variation of gas and dust tracers and thus the PDR structure and anatomy in Sect. 5. We analyse the H I and He I recombination lines, the fluorescence lines, and the H_2, C I , and AIB emission to determine the physical conditions in the Bar in Sect. 6. Last, we discuss the Bar's structure in Sect. 7 and give a summary and conclusions in Sect. 8.

2. Bar

The Bar is a rim of the Orion molecular cloud core (OMC-1), the closest site of ongoing massive star-formation[3] (e.g. Genzel & Stutzki 1989; Bally 2008). The Bar is often referred as the 'Bright Bar' or 'Orion Bar' (e.g. Elliott & Meaburn 1974; Tielens et al. 1993; O'Dell et al. 2020). In the following, we name it the 'Bar'. The outskirts of OMC-1 are primarily illuminated by strong UV radiation from the O7V-type star θ^1 Ori C (Sota et al. 2011), the most massive star of the Trapezium cluster at the centre of the Orion Nebula and ∼2′ north-east of the Bar (e.g. Stacey et al. 1993; Luhman et al. 1994; O'Dell 2001; Goicoechea et al. 2015). Intense ionising radiation and strong winds from θ^1 Ori C (two main forms of stellar feedback in the region; Güdel et al. 2008; Pabst et al. 2019) power and shape the Orion Nebula, which is a blister H II region that is eating its way into the natal molecular cloud (located behind the cluster in our line of sight). The strong stellar UV radiation has carved out a large cavity in the background molecular cloud, where the inner concave regions tilt to form the Bar (e.g. O'Dell 2001).

The Bar historically refers to the elongated rim near the ionisation front (IF) that separates the edge of the molecular cloud from the surrounding H II region, with $n_e \simeq 5{\times}10^3$ cm^{-3} and $T_e \simeq 9{\times}10^3$ K at the IF (e.g. Weilbacher et al. 2015). The UV radiation impinging on the IF is (1–4)×10^4 times the mean interstellar field (e.g. Marconi et al. 1998). Some areas of the Bar may also be illuminated by the O5V-type star θ^2 Ori A, on the near side of the cluster (O'Dell et al. 2017). Beyond the IF, only far-UV (FUV) photons with energies below 13.6 eV pervade the Bar. This marks the beginning of the PDR. Because of its high temperatures and nearly edge-on orientation on the sky, the Bar shines at all wavelengths from optical to radio. Indeed, this PDR is the prototypical source to study the physical and chemical stratification caused by strong FUV radiation (e.g. Tielens et al. 1993; Hogerheijde et al. 1995; Jansen et al. 1995; van der Wiel et al. 2009).

The first layers of the Bar PDR are predominantly neutral and atomic, meaning [H] > [H_2] ≫ [H^+] (van der Werf et al. 2013; Henney 2021). The so-called 'atomic PDR' zone presents a plethora of IR atomic emission lines from low ionisation potential elements (recombination lines, forbidden lines, etc.; e.g. Walmsley et al. 2000). This warm (several hundred K) and moderately dense (n_H of a few 10^4 cm^{-3}) gas is mainly heated by photoelectrons ejected from Polycyclic Aromatic Hydrocarbons (PAHs), and mainly cooled by far-IR (FIR) [C II] 158 µm and [O I] 63 µm fine-structure lines (e.g. Tielens et al. 1993; Herrmann et al. 1997; Bernard-Salas et al. 2012; Ossenkopf et al. 2013). In addition, this extended atomic PDR zone coincides with the peak of very bright AIB emission (e.g. Bregman et al. 1989; Sellgren et al. 1990; Tielens et al. 1993; Giard et al. 1994; Knight et al. 2021).

At about 15″ (∼0.03 pc) from the IF, the flux of FUV photons is sufficiently attenuated that most of the hydrogen becomes molecular. This position marks the critical H/H_2 transition zone, the dissociation front (DF). The DF displays several IR rotational H_2 and the HI 21 cm emission lines (e.g. Parmar et al. 1991; van der Werf et al. 1996, 2013; Allers et al. 2005; Shaw et al. 2009). In addition, H_2 lines from FUV-pumped vibrationally excited levels up to $v = 14$ are detected (Luhman et al. 1994; Kaplan et al. 2017, 2021). Reactive molecular ions such as CH^+, SH^+, CO^+ or OH^+ start to form close to the DF (e.g. Stoerzer et al. 1995; Fuente et al. 2003; Nagy et al. 2013; van der Tak et al. 2013; Goicoechea et al. 2017). The first steps of PDR chemistry are triggered by the presence of vibrationally excited H_2, whose internal energy overcomes the endoergicities and energy barriers of key gas-phase reactions (e.g. Goicoechea & Roncero 2022) and, thus, initiates the formation of molecular hydrides (e.g. Tielens & Hollenbach 1985a; Sternberg & Dalgarno 1995; Agúndez et al. 2010).

The transition from C^+ to C to CO is expected to take place beyond the DF, where the PDR becomes mostly molecular. That is, [H_2] ≫ [H]. However, observations have not accurately settled the exact position of the C^+/C/CO transition zone (e.g. Tauber et al. 1995; Wyrowski et al. 1997; Cuadrado et al. 2019; Salas et al. 2019). The CO gas temperature just beyond the DF is $T_k \simeq 200$–300 K (Habart et al. 2010; Joblin et al. 2018) and decreases further into the molecular cloud. This confirms the presence of a sharp (gas and dust) temperature gradient from the H II region interface to the molecular cloud interior (Arab et al. 2012; Salgado et al. 2016). Despite the strong irradiation conditions, the so-called 'molecular PDR' ($n_H \simeq 10^5$-10^6 cm^{-3}) shows a rich chemical composition, including a large variety of small hydrocarbons and complex organic species (e.g. Hogerheijde et al. 1995; Simon et al. 1997; Peeters et al. 2004; Leurini et al. 2006; Cuadrado et al. 2015, 2017). Dense clumps ($n_H \simeq 10^7$ cm^{-3}) with angular sizes of ∼5″ (∼2000 au) are known to exist deeper inside the Bar (e.g. Tauber et al. 1994; van der Werf et al. 1996; Young Owl et al. 2000; Lis & Schilke 2003). However, it is not clear whether these clumps will ultimately form stars and whether smaller (sub-arcsecond) clumps can exist closer to the DF (e.g. Gorti & Hollenbach 2002;

[2] https://pdrs4all.org

[3] The most commonly adopted distance to the Bar is 414 pc (Menten et al. 2007) although recent GAIA observations suggest slightly lower values (Kounkel et al. 2018; Großschedl et al. 2018). We refer to Habart et al. (2024) for a discussion. In this paper we adopt a distance of 414 pc. Hence, 1″ roughly corresponds to 0.002 pc.

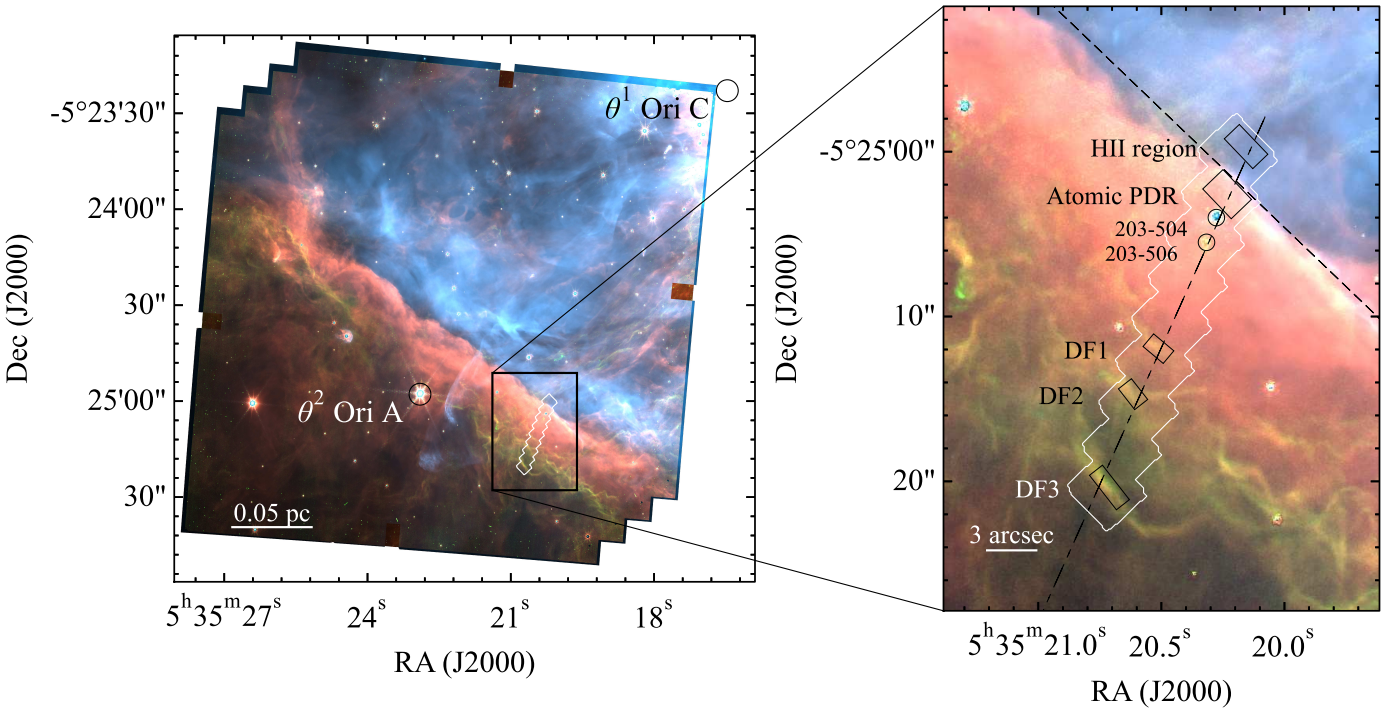

Fig. 1. Composite NIRCam image of the Bar showing the NIRSpec mosaic footprint (white boundary). The composite image is composed of F335M (AIB emission) in red, F470N-F480M (H_2 emission) in green, and F187N (Paschen α emission) in blue (Habart et al. 2024). Bright stars θ^1 Ori C and θ^2 Ori A are indicated with black circles in the left panel. In the right panel the five black boxes indicate the apertures used to extract our five template spectra. The dot-dashed line indicates the cut perpendicular to the Bar (position angle, PA, of 155.79°), while the dashed line indicates the position of the ionisation front in the NIRSpec FOV (PA=46.21°). The protoplanetary disks 203–504 and 203–506 are indicated with black circles.

Andree-Labsch et al. 2017). If they exist, additional heating by collisional de-excitation of vibrationally excited H_2 will keep their irradiated surfaces very hot, at several thousands K (e.g. Burton et al. 1990).

Unfortunately, most of our knowledge of the Bar comes from modest angular resolution observations (~5″–40″), especially at FIR to radio wavelengths, that do not spatially resolve the main transition zones of the PDR. Consequently, their fundamental structures: homogeneous versus clumpy, physical conditions, chemical composition, and role of dynamical effects are not fully known. ALMA provided the first ~1″ resolution images of the CO and HCO^+ emission (Goicoechea et al. 2016). Instead of an homogeneous PDR with well-defined and spatially separated H/H_2 and C^+/C/CO transition zones, ALMA revealed rich small-scale structures (akin to filaments and globulettes), sharp-edges, and uncovered the molecular emission from a protoplanetary disk (203–506; Bally et al. 2000; Champion et al. 2017). Even spatially sharper IR photometric images with the Keck telescope (using adaptative optics) uncovered the presence of not a single, but several small-scale photodissociation fronts (Habart et al. 2023). Our JWST/NIRSpec integral field observations across the Bar, from the H II region to the main molecular dissociation fronts (and including the protoplanetary disks 203–504 and 203–506), represent the first sub-arcsecond spectroscopic study of this prototypical PDR. This study complements our first JWST photometric images of the Bar (Habart et al. 2024), which show an unprecedented view of the region, revealing very complex small-scale PDR structures, and ridges, and a 3D terraced distribution of multiple dissociation fronts that contrasts with the classical 1D view of the H/H_2 and C^+/C/CO transition zones of a PDR.

3. Observations, data reduction, and analysis

3.1. Observations

The observations are part of the Early Release Science programme PDRs4All: Radiative feedback from massive stars (ID: 1288, PIs: Berné, Habart, Peeters; Berné et al. 2022)[4]. We obtained our observations using the NIRSpec instrument (Jakobsen et al. 2022) onboard the JWST (Gardner et al. 2006) in the integral field unit (IFU) mode (Böker et al. 2022), which provides spatially resolved imaging spectroscopy. This resulted in a 9 × 1 mosaic covering 3″ × 25″ and centred on position α(J2000) = 05 35 20.4749, δ(J2000) = –05 25 10.45 with a position angle (PA) of 43.74° in the 0.97–5.27 μm range at a angular resolution of 0.075″ to 0.173″ and with a pixel size of 0.1″×0.1″. The field of view (FOV) of the NIRSpec mosaic is shown in Fig. 1. We also obtained background observations using a single pointing centred on position α(J2000) = 05 27 19.400, δ(J2000) = –05 32 04.40. For our science and background observations, we used the three high spectral resolution, R~2700, gratings (G140H, G235H, and G395H) covering the wavelength range from 0.97 to 5.27 μm, the NRSRAPID readout mode (as this mode is appropriate for bright sources), and a 4-point dither pattern. To quantify the leakage of the Micro-Shutter Array (MSA), we used the most accurate strategy for taking imprint exposures to date, that is we obtained imprint exposures with the same exposure time as the science (and background) exposures at all dither positions. Five groups per integration with one integration per exposure are used, for a total on-source integration time of 257.7 s.

[4] DOI: 10.17909/pg4c-1737.

3.2. Data reduction

We download the uncalibrated Level 1 science and background NIRSpec IFU data from the MAST portal. We reduce the data using the JWST Science Calibration Pipeline (version 1.10.2.dev26+g8f690fdc) and context jwst_1084.pmap of the Calibration References Data System (CRDS). First, we perform detector-level corrections on science, background, and imprint exposures in the Detector 1 step. Then we correct the resulting rate files for $1/f$ noise correction using the algorithm provided by the helpdesk. The algorithm measures the pattern in the unilluminated pixels in a given rate file using a column-by-column rolling median basis and subtracts it from the data in the illuminated pixels of that file. These cleaned rate files are then used as input for calibrations of individual exposures in the Spec 2 step. Finally, we combine all exposures to build cubes in Spec 3. We note that we disabled the outlier detection step in Spec 3 because it introduces artefacts and removed bright lines from our data. Lastly, we point out that we reduce the data of each pointing in a given spectral segment separately, yielding 27 spectral cubes from 9 pointings in three spectral segments at the end of the Spec 3 step of the pipeline.

While the pipeline is able to produce a mosaic that combines all pointings over the full wavelength range, this results in some undesirable artefacts such as stripes near pointing edges. By building the mosaic outside of the pipeline, we can apply calibration factors to single-segment cubes (to improve the overall flux calibration), and we can specify precisely how we want to deal with overlapping data (spatially and spectrally).

Starting with spectral cubes generated by the JWST pipeline, we create the final mosaic using the following approach.

1. We use the Astropy-affiliated package for image reprojection `reproject`, and the `reproject.find_optimal_celestial_wcs` routine on all of the 27 input cubes (9 pointings, 3 segments each) to determine the World Coordinate System (WCS) information and array shape of the final cube.
2. Next, we use `reproject.reproject_exact` to reproject every wavelength-plane of these 27 cubes to the final cube shape and WCS.
3. A physical gap between NIRSpec's detectors leads to a gap of missing wavelengths in each IFU cube (for details see Böker et al. 2022). The wavelength gap spans bluer wavelengths in the northern part of each pointing and smoothly shifts to redder wavelengths towards the southern part of each pointing. As best as possible, we use data from adjacent pointings to fill in these gaps. For spaxels that are covered by two partially overlapping pointings, we coadd the overlapping spectra unless one of the spaxels is either missing flux, or is within a 9-pixel distance from the respective pointing edge (a 9 pixel distance was chosen to avoid edge effects). If a spaxel fills in flux that is missing from an overlapping spaxel due to a wavelength gap, we use `specutils.manipulation.FluxConservingResampler` to resample the fluxes onto the wavelength grid of the cube where flux is missing. We resample onto the wavelength grid of the pointing with missing flux because the number of spaxels that require interpolation is a small minority of the total number of spaxels, and because all spaxels in the mosaic need to be on the same wavelength grid – only spaxels from the cube that are affected by the wavelength gap need to be dealt with separately. As a consequence, not all pixels in the extraction aperture contribute at a given wavelength in the wavelength gap region. For cases where one of the two spatially overlapping spaxels is within 9 pixels of the edge of its respective pointing while that of the other pointing is not, the spaxel that is closer to the edge of its pointing is ignored – at that location, the mosaic contains the spaxel that is further from its pointing edge.
4. We then ensure that the NIRSpec flux calibration is accurate by computing synthetic NIRCam images from the NIRSpec cubes, then reproject background-subtracted NIRCam images onto the NIRSpec pixel grid, and then compare the synthetic NIRCam flux against the true NIRCam flux in each pixel. Similar to the cross-calibration method between imaging and IFU observations of Kraemer et al. (2022) using *Spitzer*/IRAC and *Spitzer*/IRS data, we perform a linear regression on the pixel-by-pixel synthetic NIRCam flux vs. true NIRCam flux. The best-fit slope of this relationship (for each NIRCam filter) is our estimate of the cross-calibration factor between NIRCam and NIRSpec. The best-fit parameters are tabulated in Table A.1 (see Chown et al., in prep., for details).
5. We then multiply the G235H and G395H NIRSpec mosaics and their uncertainties by their respective calibration factors. Since we do not have background-subtracted NIRCam data in any filters that overlap with the G140H wavelength range, we are unable to assess the flux calibration of that segment in the same way. We multiply the G140H mosaic by the calibration factor for the G235H segment. We tested an approach where each G140H spaxel was scaled to match the flux in the overlapping G235H spaxel, but we found this approach to be unreliable due to the presence of data reduction-related artefacts.

The applied reduction process produces very high quality data. However, after processing the raw data, some artefacts remain in the data. The remaining artefacts that are present include:

1. Bright circular artefacts that are localised in wavelength (a few spectral bins) and in position (roughly circular, a few pixels wide, and in the same positions on the detector).
2. Vertical stripes at the edge of each pointing (N-NW to S-SE direction) with lower flux, likely due to the fact that a path loss correction using flight data cannot be performed using the available reference files.
3. A sinusoidal wave pattern in the uncertainty data of the three segments.
4. Fluxes within a few wavelength bins of a gap are generally unreliable.
5. A roughly sinusoidal wave pattern in the surface brightness and/or broad absorption/emission features in gratings G140H and G235H in the NRS2 detector[5]. As these are not present in the grating covering the subsequent wavelength range in the NRS1 detector, this is likely residual $1/f$ noise (the effects of $1/f$ noise are more pronounced on the NRS2 detector compared to the NRS1 detector).

We mask out the bright circular artefacts, and replace bad data from vertical stripes with better data when co-adding adjacent pointings as mentioned above[6].

We extract spectra in five apertures (Fig. 1 and Table A.2) by applying a 3-σ cut to remove bad data and calculating the inverse-variance weighted average of spaxels within each aperture. We use five large extraction apertures positioned in front of the ionisation front (IF), at the peak of the PAH emission, and at the three H/H_2 dissociation fronts (DF 1, DF 2, DF 3) in the

[5] The NRS1 (NRS2) detector covers wavelengths below (beyond) the wavelength gap in each segment.
[6] See acknowledgments for data availability.

mosaic. The resulting spectra thus serve as templates for the H II region, the atomic PDR and the molecular PDR. In addition, to measure quantities from weaker lines as a function of distance from θ^1 Ori C, we spatially rebin the spectral mosaic to a 2×2 spaxels scale prior to fitting the lines.

3.3. Flux measurements

We measure the flux of selected emission lines by fitting a Gaussian line profile of a fixed full width at half maximum (FWHM) set by the spectral resolution at that wavelength. We determine the spectral resolution by using the resolution curves for the G140H, G235H, and G395H gratings given in the Jdox[7]. Before performing a fit, we subtract a linear continuum. We visually select a wavelength range for continuum determination that is devoid of emission lines. Given the presence of artefacts in the data set and the fact that the wavelength range for fitting is very small, we find that subtracting an offset for the continuum instead of a linear continuum works better when measuring fluxes across the entire spectral map. Lines located on top of the strong 3.3 μm AIB are fit after removal of the AIB emission (see Sect. 6.6.1 for details). Given the large number of lines present in the template spectra (~600), we model the continuum using a non-linear iterative peak-clipping algorithm[8] to provide the fluxes for the entire line inventory (see Appendix B). In the 3–3.7 μm region, we use the fit to the AIB emission instead as the continuum.

For the uncertainties on the measured fluxes, we use the flux uncertainties from the Gaussian fit of the line which takes into account the uncertainties on the surface brightness provided by the data reduction pipeline. We note that the uncertainties resulting from the pipeline are too low and therefore, the quoted flux uncertainties likely underestimate the true uncertainties. In addition, uncertainties in the continuum determination are not included[9]. To assess the influence of the artefacts on the line fluxes, we compare selected line fluxes with their corresponding NIRCam filter combination (see Habart et al. 2024, their Fig. 11) and conclude that the agreement with NIRCam is excellent. Indeed, despite remaining systematic artefacts in the data set, the change in intensities of Br α, Pa α, [Fe II] at 2.1644 μm, H_2 0–0 S(9), H_2 1–0 S(1), and total AIB emission across the PDR matches their spatial behaviour as observed by NIRCam very well. In addition, the Br α, Pa α, H_2 0–0 S(9), and total AIB emission agree within 3% on the absolute scale with their corresponding (continuum subtracted) NIRCam filter (note the AIB filter does not require continuum subtraction). Deviations are larger for the [Fe II] at 2.1644 μm, and H_2 1–0 S(1) emission as these transitions do not dominate the emission captured by the corresponding (continuum subtracted) NIRCam filter[10].

4. Spectral inventory

4.1. Template spectra of the Bar

The five template spectra probing the H II region, the atomic PDR, and the molecular PDR (see Sect. 3.2) are shown in Fig. 2 and in more detail with line labels in Fig. B.1. These 0.97–5.27 μm near-IR (NIR) spectra reveal a spectacular richness of spectral lines and bands on top of weak continuum emission (see Table B.1 for full inventory and line intensities). In particular at the shortest wavelengths, numerous (blended) emission lines are present to the point of the line confusion limit.

Across the mosaic, H I recombination lines are detected from the Paschen series (up to principal quantum number $n_u = 7$ in all template spectra) and the Bracket, Pfund, Humphreys, and $n_l = 7$ series (up to $n_u = 25$–40 in the molecular PDR; $n_u = 45$–50 in the H II region and atomic PDR). We also detect numerous He I recombination lines as well as emission lines from Fe II and Fe III, C I recombination lines, O I and N I fluorescent emission, the Si II, P II, and K III emission line(s), and the [Kr III] 2.1986 μm transition. In addition to atomic and ionic lines, the NIR spectra of the Bar show many high-energy ro-vibrational lines from simple molecules (H_2, HD, CO, and CH^+). These lines are generally faint and become apparent deeper inside the molecular layers of the PDR (DF 1, DF 2, and DF 3 templates), where most of the hydrogen is locked up in H_2.

The molecular emission is dominated by a forest of H_2 lines from vibrationally excited bands ($v = 1$–0, $v = 2$–1, etc.), with detections up to $v = 6$. Kaplan et al. (2021) previously reported on the detection of some of these lines (in the 1.45–2.45 μm range) from ground-based observations at higher spectral resolution than NIRSpec (R~45 000), but at significantly lower angular resolution (0.3″ pixel scale). These vibrationally excited levels are populated by far-UV (FUV) pumping in the Lyman and Werner bands of H_2, followed by radiative and collisional de-excitation (Black & Dalgarno 1976; Sternberg & Dalgarno 1989; Burton et al. 1990). Interestingly, we also detect ro-vibrational lines of the HD isotopologue in the $v = 1$–0 band at ~2.6 μm (the R branch, Figs. 3, B.1).

In addition, we detect high-J H_2 pure rotational lines in the ground vibrational state, up to $v = 0$–0 $S(19)$, involving very high-energy rotational levels; $E_u/k \simeq 30{,}000$ K. Moreover, we report on the first detection of H_2 pure rotational lines within the vibrationally excited states $v = 1$ (up to $v = 1$–1 $S(17)$) and $v = 2$ ($v = 2$–2 $S(13)$). These highly excited rotational levels are populated by the radiative and collisional de-excitation of FUV-pumped levels.

Quite unexpectedly we report on the first detection, towards an interstellar PDR, of the CO $v = 1$–0 and $v = 2$–1 bands centred at 4.7 μm (Fig. 3). Detected ro-vibrational lines are faint but seen up to high J values. This implies that rotational levels within the vibrational state $v = 2$, with energies of about $E/k \simeq 7000$ K, are populated in the PDR. These are substantially higher energies than those of the highest-J pure rotational line ($v = 0$–0, $J = 23$–22) detected in the far-IR ($E_u/k \simeq 1500$ K; Joblin et al. 2018).

Concerning other hydride molecules previously detected in the Bar through rotational spectroscopy of the $v = 0$ state (e.g. Gerin et al. 2016), we detect CH^+ $v = 1$–0 ro-vibrational lines at ~3 μm (see spectroscopic analysis in Changala et al. 2021). Far-IR pure rotational lines of CH^+ up to $v = 0$–0, $J = 5$–6 were first detected by Nagy et al. (2013) at the much lower (~10″) angular resolution with the Herschel space telescope. Here we detect CH^+ $v = 1$–0 ro-vibrational lines towards both the atomic PDR and the molecular PDR (DF 1, DF 2, and DF 3; Fig. 4). This likely indicates that small molecular fractions of H/H_2 are enough to form sufficient CH^+ and to excite the $v = 1$–0 band through chemical formation pumping (CH^+ is a very reactive molecular ion; e.g. Nagy et al. 2013; Godard & Cernicharo 2013). The NIR CH^+ $v = 1$–0 band has stronger P-branch

[7] https://jwst-docs.stsci.edu/jwst-near-infrared-spectrograph/nirspec-instrumentation/nirspec-dispersers-and-filters

[8] Statistics-sensitive Non-linear Iterative Peak-clipping algorithm from pybaseline https://pybaselines.readthedocs.io/en/latest/

[9] In case of continuum determination using a non-linear iterative peak-clipping algorithm, the uncertainties are asymmetric with the upper bound being larger than the lower bound.

[10] See acknowledgements for data availabillity of all maps and profiles along the NIRSpec cut.

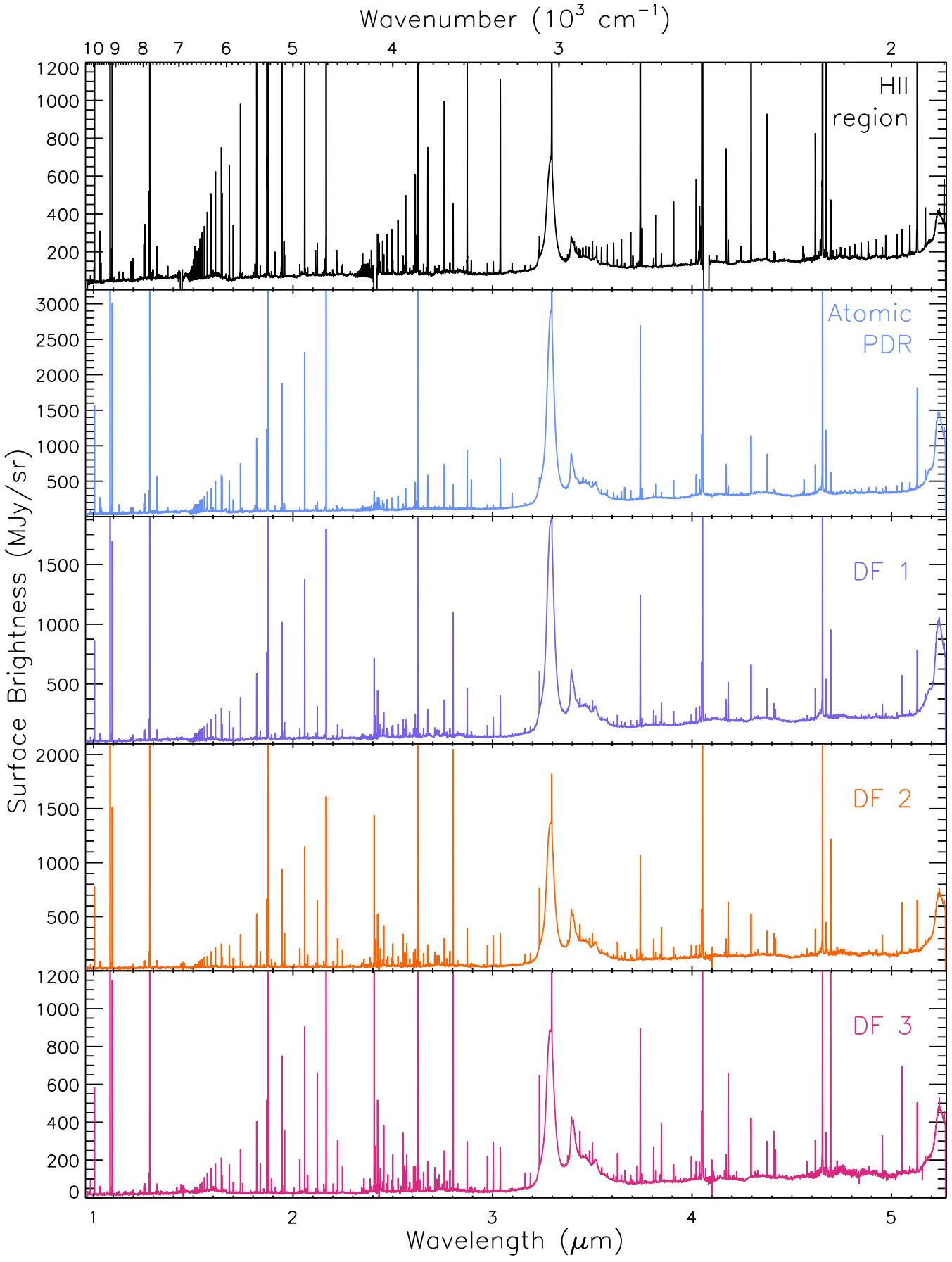

Fig. 2. Template spectra representing, from top to bottom, the H II region, the atomic PDR, and the dissociation fronts DF 1, DF 2, and DF 3.

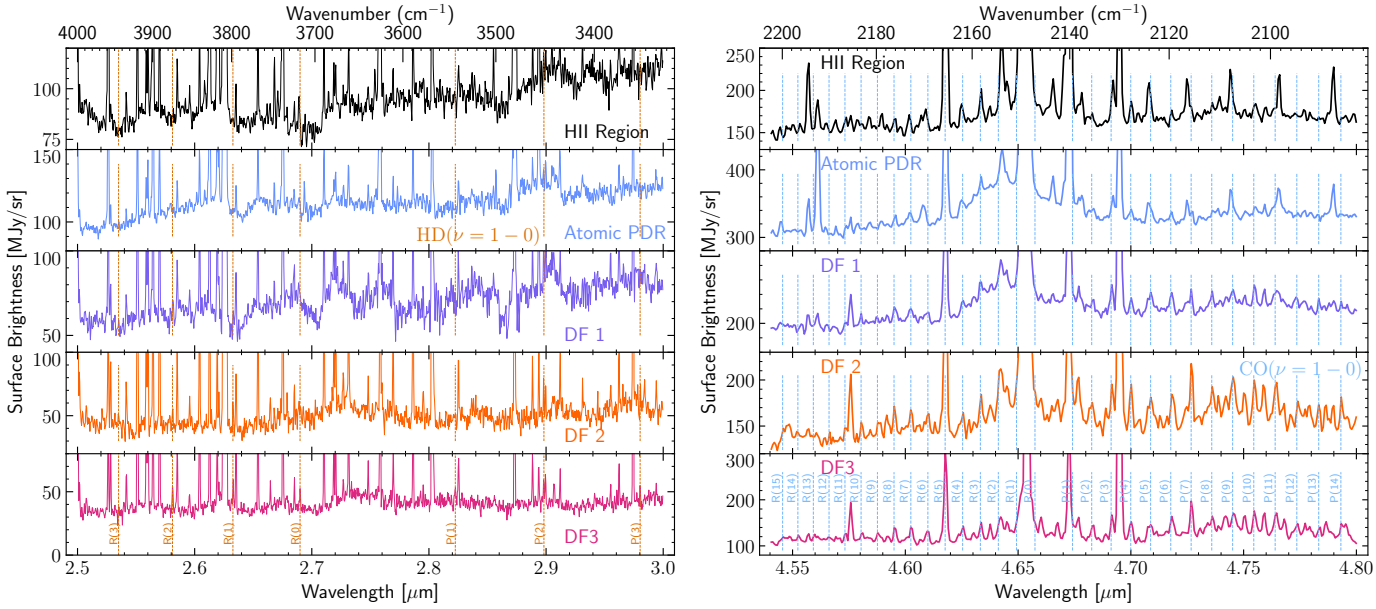

Fig. 3. Detection of the HD v = 1–0 ro-vibrational lines at ~2.6 μm (left) and of the CO v = 1–0 band centred at 4.7 μm in the molecular PDR (right). For the CO v = 2–1 band detection, see Fig. B.1.

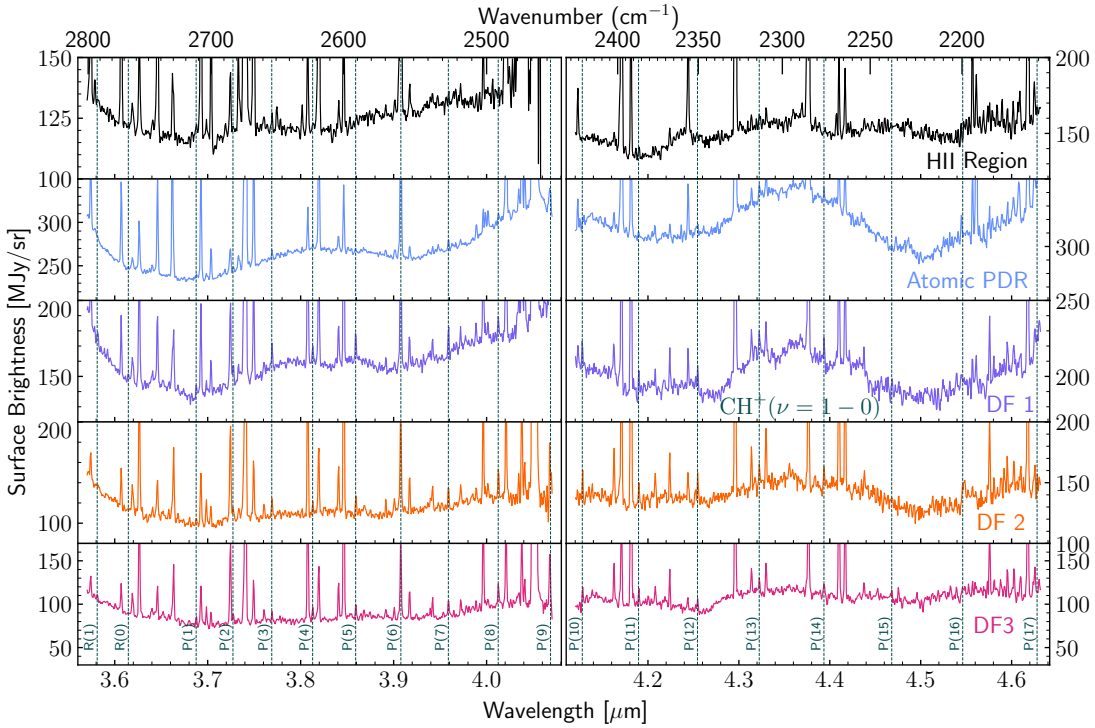

Fig. 4. Detection of the CH^+ v = 1–0 ro-vibrational lines in the atomic PDR, DF 1, DF 2, and DF 3.

lines than *R*-branch lines (nearly undetected), a spectroscopic behaviour previously reported and explained by Neufeld et al. (2021) towards the planetary nebula NGC 7027. For a detailed analysis of the CH^+ v = 1–0, we refer the reader to Zannese et al. (in prep.).

We observe weak continuum emission with increasing surface brightness towards longer wavelengths. The continuum emission does not increase in surface brightness towards the shortest wavelengths, indicating there is not a strong contribution from scattered light from young massive stars such as θ^1 Ori C. The Orion Nebula hosts many low and intermediate mass stars (Hillenbrand & Carpenter 2000) which can contribute to the observed continuum emission (by scattering). In addition, the observations are consistent with a continuum contribution from stochastically heated very small grains and/or blended overtone and combination bands from PAHs (see Sect. 5.1). A detailed breakdown of the various continuum contributors will be investigated in a forthcoming paper (Onaka et al. in prep.).

The observations also display strong aromatic infrared bands (AIBs; Fig. 5). The strong 3.29 μm AIB along with weaker bands at 3.25, 3.40, 3.46, 3.52, 3.56 μm are perched on top of a broad plateau (see also Geballe et al. 1989; Sloan et al. 1997). We report

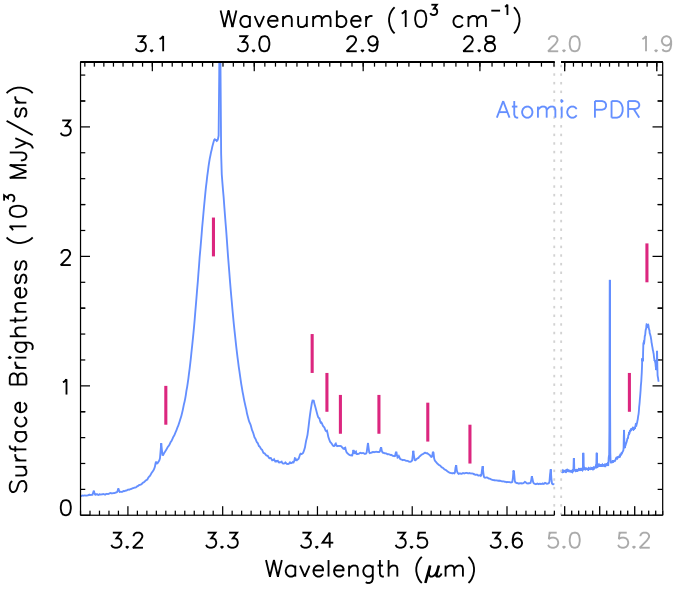

Fig. 5. Components of the AIB emission detected in the atomic PDR.

that the 3.40 μm band is composed of three sub-components centred at 3.395, 3.403, and 3.424 μm. An additional AIB band is (partially) detected at 5.236 μm. This band has a blue shoulder peaking near 5.18 μm. While the bands at ∼3.4 μm are aliphatic in nature (see Sect. 6.6), we refer to these bands as the AIBs in the remainder of the paper.

While the detection of weak broad features is very challenging given the current calibration (Sect. 3.2), Fig. 6 reveals broad structures in the 3.5–5.2 μm range[11]. All templates, except the H II region template, show enhanced emission (with respect to a linear continuum) from ∼3.1 μm to ∼4.9 μm. We rule out an artificial decrease in flux near 4.5 μm, which is much less pronounced in the H II region template, because the template spectra match the MIRI-MRS continuum (starting at 4.9 μm) very well indicating the flux levels near 5 μm are accurate. Consequently, the templates tentatively show a lack of emission or an absorption feature near 4.5 μm. We are unaware of any known absorption feature near 4.5 μm of similar width and thus favour the interpretation of a lack in emission. If born out, such an extended emission (band) has not been seen before, likely due to the lower angular resolution and incomplete wavelength coverage, and, in some cases, low data quality, and may arise from blended overtone and combination bands from PAHs (Allamandola et al. 1989). A detailed investigation of its characteristics will be presented in a forthcoming paper. The templates show an asymmetric band (with a red wing) centred at 4.644 μm and potentially an asymmetric band (with a red wing) centred at 4.746 μm (see also Appendix H.2). The CD stretching mode in deuterated PAHs, occurs between 4.54 and 4.75 μm (Hudgins et al. 2004; Buragohain et al. 2015; Yang et al. 2020, 2021; Allamandola et al. 2021). In particular, the CD stretch in PAHs to which D atoms are added (DPAHs) occurs near 4.6 μm (2170 cm^{-1}), whereas the CD stretch in deuterated methyl groups near 4.7 μm (2130 cm^{-1}). This band has been observed in Orion and a few other H II regions (Peeters et al. 2004; Onaka et al. 2014, 2022; Doney et al. 2016), although the band profile could not be resolved due to the low angular and spectral resolution. The atomic PDR and, perhaps, DF 1 also show two broad emission bands centred near 3.8 μm (with a width of ∼0.5 μm) and near 4.35 μm. These bands coincide with a nitrile (-CN) stretch at 4.38 μm (2280 cm^{-1}) and at 4.52 μm (2220 cm^{-1}), and the CD stretch for PAHs in which a peripheral H atom is replaced by a D atom (PADs), near 4.4 μm (4.3–4.5 μm range; Hudgins et al. 2004; Allamandola et al. 2021)[12]. Lastly, DF 3 shows a potential band in absorption near 4.27 μm that could arise from the C=O antisymmetric stretching mode in CO_2 ice. However, the presence of CO_2 ice in the PDR is unlikely given the physical conditions in the dissociation front (e.g. hot gas temperature, warm grains, low A_V) and the apparent lack of H_2O ice. Improved data reduction and/or further observations may have to confirm the reality of this feature.

4.2. Reference line list

To facilitate the identification of detected lines in the present observations as well as in future JWST observations, we prepared a line list based on model calculations using the Cloudy (Ferland et al. 2017) and Meudon PDR codes (Le Petit et al. 2006). A detailed description of these model calculations can be found in Berné et al. (2022). These model calculations include lines with intensities greater than 5×10^{-10} W m^{-2} sr^{-1}. After the data arrived, we expanded the line list to include all detected lines. The resulting line list includes hydrogen recombination lines with the upper principal quantum number up to 50 and all the lines of molecular hydrogen listed in Roueff et al. (2019). We also include [Fe III], [Ni II], and [Ni III] lines, which were not included in the Cloudy simulation but are detected in the ionised region (see also Van De Putte et al. 2024). O I and N I fluorescence lines are added with the criteria that the Einstein-A coefficients are larger than 5×10^5 s^{-1} and 0.9×10^5 s^{-1} for N I and O I, respectively. The criteria are chosen to include all detected lines. For molecular lines, we include the rovibrational lines of HD up to $v = 3$ and those of CO with $v = 1$–0 and 2–1. Some of these transitions are also detected in the molecular PDR. In addition, the lines of CH^+ and OH are included; the latter is detected in the proplyd 203–506, which is located within the NIRSpec mosaic (Berné et al. 2023; Zannese et al. 2023). Finally, the list also contains several dust bands, including strong absorption bands of ice species, major AIBs, and C_{60}.

The line list contains the transition wavelength in vacuum, assignment of the transition, upper level energy, and Einstein A-coefficient. Atomic transition data are taken from the atomic line database at University of Kentucky (van Hoof 2018)[13]. For molecular hydrogen, we refer to Roueff et al. (2019). We adopt the CO and HD data from the HITRAN (Gordon et al. 2022)[14]. We used the data of Changala et al. (2021) for CH^+ and the OH data collected by Tabone et al. (2021) and Zannese et al. (2024) using Yousefi et al. (2018) and Brooke et al. (2016). Values in Brieva et al. (2016) are used for C_{60}, while the data in Sect. 6.6 (Gaussian decomposition) and Chown et al. (2024) are taken for the AIBs shortwards of 17 μm while the data from Smith et al. (2007) are taken for the AIBs longwards of 17 μm. For the ice species, we refer to Gibb et al. (2004) and Boogert et al. (2015).

The present line list contains nearly 7000 lines and dust bands, which are potentially detectable by NIRSpec and

[11] We note that the NRS1 detector covers wavelengths up to 3.983–4.099 μm, whereas the less reliable NRS2 detector covers wavelengths larger than 4.086–4.203 μm depending on the IFU virtual slit. However, no artefacts are known at the positions of these structures (per the JWST helpdesk).

[12] We note that this also coincides with an aldehyde (-CHO) stretch at 3.8 μm (2600 cm^{-1}), however, this would also give a C=O stretch near 5.9 μm that is not detected (Champion et al. 2017).

[13] https://www.pa.uky.edu/~peter/newpage/

[14] https://hitran.org

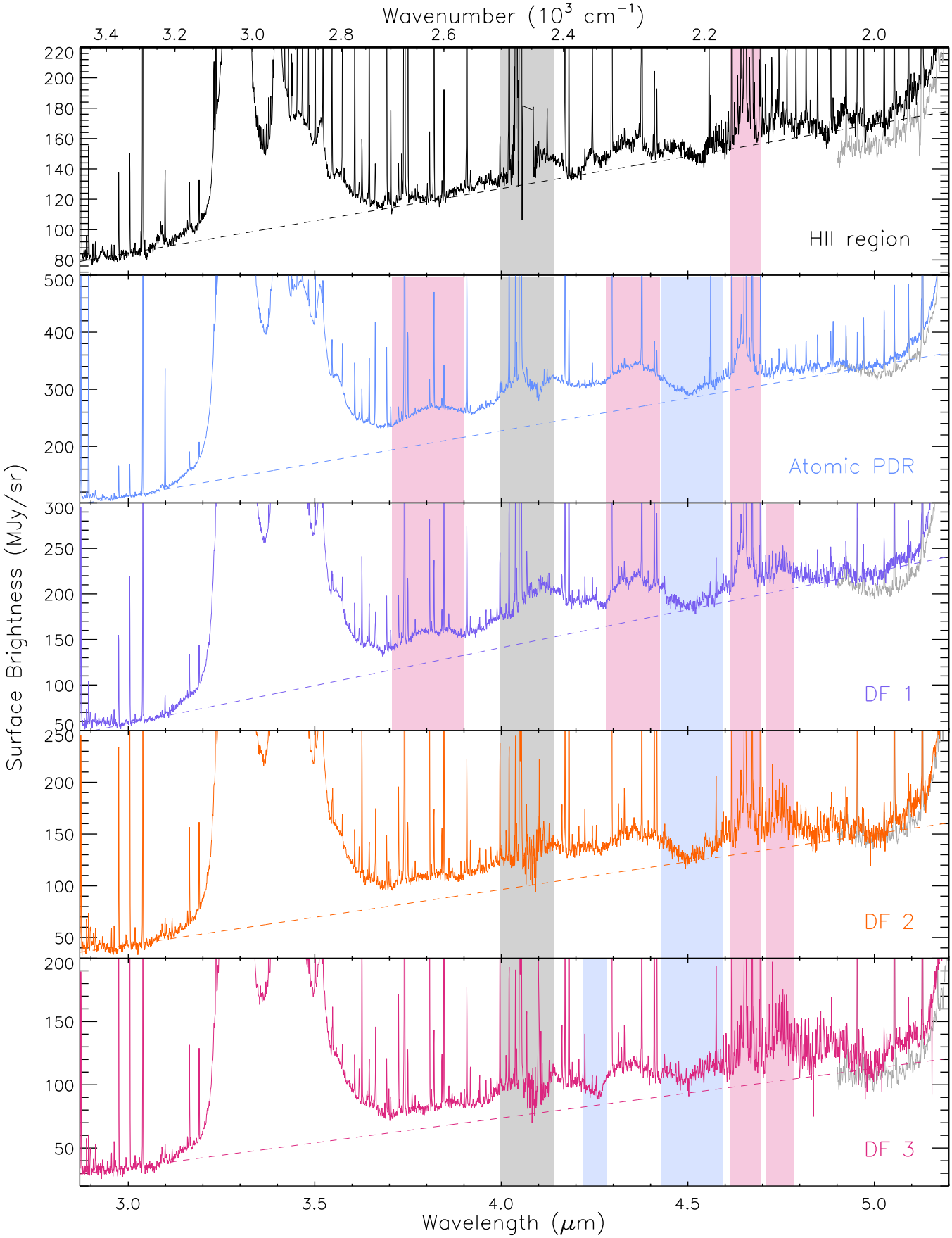

Fig. 6. Illustration of excess broadband emission between 3 and 5 μm. Close to the wavelength gap, fluxes are often unreliable (Sect. 3.2; indicated by the grey shaded area). The MIRI spectra are shown in light grey. The dashed lines show a linear continuum matched with the data near 2.98 and 4.99 μm. Red (blue) shaded boxes indicate tentative emission (absorption) bands. See Sect. 4.1 for a discussion.

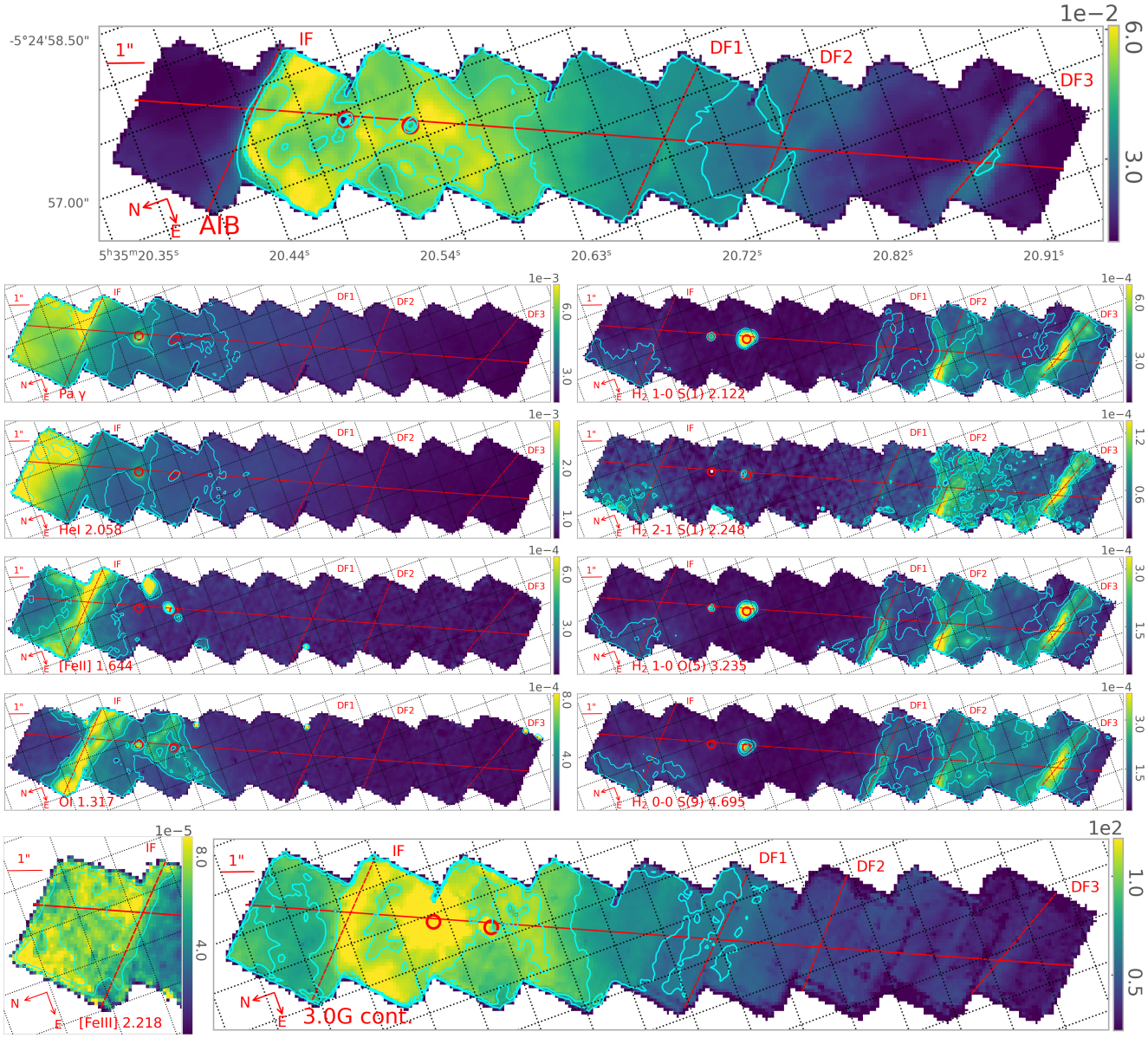

Fig. 7. Bar as seen in selected transitions in units of erg cm^{-2} s^{-1} sr^{-1}. No extinction correction is applied. Starting at the top, we show an image of the total AIB emission (i.e. sum of all AIB components in the 3.2–3.7 μm range). Following that, (from top to bottom) we show Pa γ, He I 2.058 μm, [Fe II] 1.644 μm, O I 1.317 μm, and [Fe III] 2.218 μm in the left column and H_2 1–0 S(1), H_2 2–1 S(1), H_2 1–0 O(5), H_2 0–0 S(9), and the continuum from the Gaussian decomposition at 3 μm (MJy sr^{-1}) in the right column. We set the colour range from the bottom 0.5% to the top 99.5% intensity levels of the data for each map (across the entire NIRSpec mosaic), excluding values of zero, edge pixels, and the two proplyds (as well as the surrounding region of the proplyds for the continuum). White pixels inside the mosaic indicate values of zero reflecting issues with the data. The nearly horizontal red line indicates the NIRSpec cut and the nearly vertical red lines indicate from left to right the IF and the DFs (DF 1, DF 2, DF 3). The two proplyds are indicated by the circles. Across the entire NIRSpec mosaic, contours show the 52, 75, and 90% intensity levels of the data for AIB, 65, 80, 98% for Pa γ and He I 77.9, 90.2, 96% intensity levels for O I 1.317 μm and [Fe II] 1.644 μm, 87.7, 94.9% intensity levels for [Fe III] 2.218 μm, 60, 90, 98% intensity levels for H_2 (excluding H_2 2–1 S(1), which uses 80, 90, 98% intensity levels), and the 50, 68, 85% intensity levels for the continuum at 3 μm. We note that a smoothing is applied to the [Fe III] 2.218 μm contour levels.

MIRI/MRS observations. The list is available in the science enabling products at the PDRs4All website [15]. We note that there still remain several unidentified lines in the spectra (see also Van De Putte et al. 2024).

5. Spatial variation of gas and dust tracers

Figures 7 and 8 show maps of the intensity variation of selected gas and dust tracers. Surface brightness profiles along a cut across the NIRSpec mosaic (depicted in Fig. 1, PA=155.79°) are shown in Fig. 9[16]. We discuss the Bar PDR in Sect. 5.1 and the emission associated with the two proto-planetary disks in Sect. 5.2.

5.1. Variations in the Bar

A layered structure is observed as we move away from θ^1 Ori C. The ionisation front (IF), the atomic PDR as traced by AIB emission, and the H_2 emission peak at increasing distances,

[15] https://pdrs4all.org

[16] See acknowledgments for data availability.

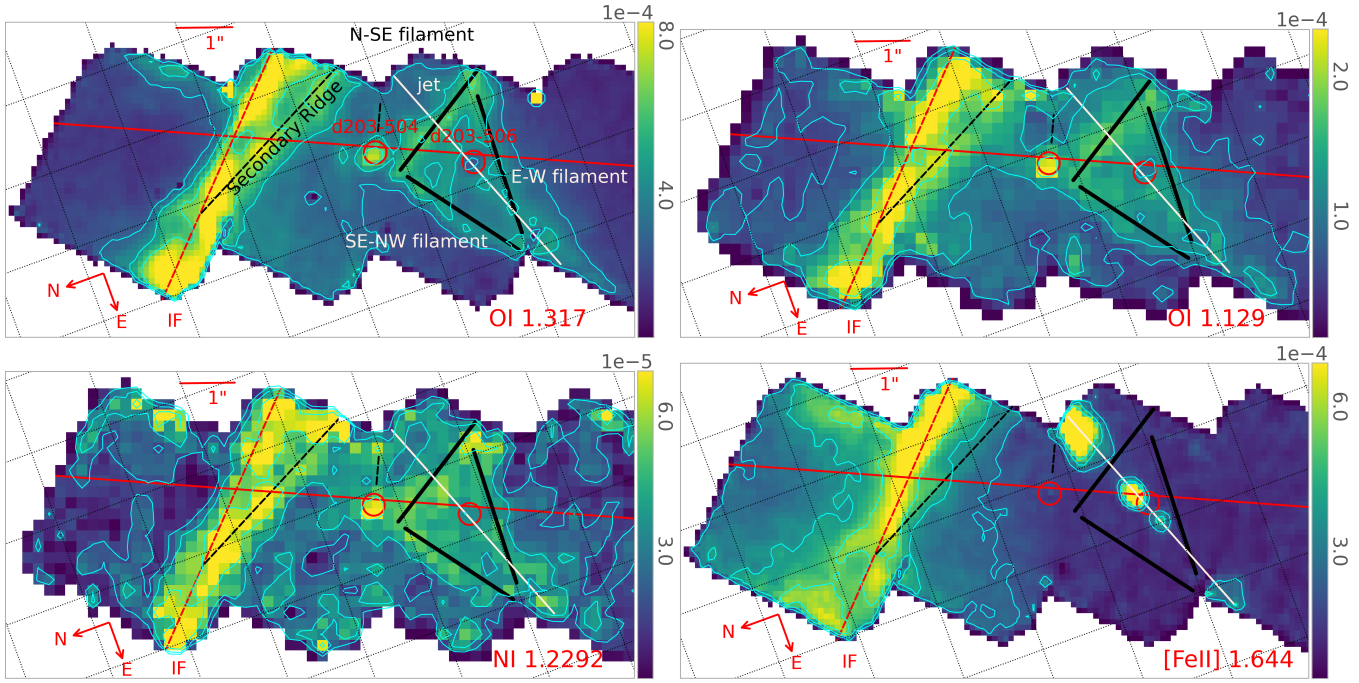

Fig. 8. Maps of O I 1.317 μm, 1.129 μm (top) as well as N I 1.2292 μm and [Fe II] 1.644 μm (bottom) across part of the NIRSpec mosaic (see the O I 1.317 μm and [Fe II] 1.644 μm maps in Fig. 7 for the full mosaic). Similar filamentary structure beyond the IF is seen in the three fluorescent lines but not in the [Fe II] 1.644 μm line. We set the colour range from the bottom 0.5% to the top 99.5% intensity levels of the data for each map (across the entire NIRSpec mosaic), excluding values of zero, edge pixels, and the two proplyds. White pixels inside the mosaic indicate values of zero reflecting issues with the data. The nearly horizontal red line indicates the NIRSpec cut and the nearly vertical red line indicates the IF. The dashed black line crossing the IF indicates the secondary ridge. The two proplyds are indicated by the circles, the jet associated with proplyd 203–504 by a white solid line and the filaments by black lines. Contours show the 77.9, 90.2, and 96% intensity levels of the data for O I 1.317 μm, 70, 85, and 97% intensity levels for O I 1.129 μm and 55, 81, and 96% intensity levels for N I 1.2292 μm, and 80, 90.2, and 96% intensity levels of the data for [Fe II] 1.644 μm (across the entire NIRSpec mosaic).

consistent with earlier studies (e.g. Tielens et al. 1993; Marconi et al. 1998; Walmsley et al. 2000; Goicoechea et al. 2015; Habart et al. 2024). However, given the angular resolution of NIRSpec, we can now observe and resolve this anatomy at sub-arcsec scales across the 0.97–5.27 μm wavelength range, which reveals filaments and ridges not seen before. For the following discussion, we define the IF by the peak intensity of the [O I] 6300 Å and [Fe II] 1.644 μm emission lines at 0.228 pc (113.4″; PA=46.21°) from θ^1 Ori C and the dissociation fronts (DFs) by the maximum intensities of the H_2 emission at 0.250, 0.257, and 0.267 pc (124.4″, 127.9″, 133.2″) from θ^1 Ori C (see below). We use the physical parameters given in Table 2 and Fig. 14 (in Sect. 6.3.2) for the different regions in the Bar.

The H I recombination lines trace the H II region. Their emission is detected throughout the mosaic, consistent with the presence of a foreground H II region in front of the atomic and molecular PDR (Fig. 14, in Sect. 6.3.2). Overall, the H I recombination lines show the same morphology. The H I emission is strongest in the H II region, peaking slightly before the IF (by 0.1″ or 0.02×10^{-2} pc) and then decreasing steeply up to $\sim 0.9 \times 10^{-2}$ pc (~4.5″) from the IF, before levelling off at longer distances. In addition to this overall morphology with distance from θ^1 Ori C, the H I emission shows structure on smaller scales in the H II region (in front of the IF) and its peak intensity near the IF is enhanced in the south-western half compared to that in the north-eastern half. Further structure is observed near the proplyds (see Sect. 5.2).

The AIB emission traces the atomic PDR. The transition from the H II to the H I region, as traced by the AIB emission, is very sharp, with a change in surface brightness of up to ~65% over a distance of ~1″. The AIB emission remains roughly constant up to $\sim 1.3 \times 10^{-2}$ pc (~6.5″) from the IF, after which it gradually decreases. It exhibits local maxima near the proplyds (Sect. 5.2). Additional local maxima are detected near the three dissociation fronts, but these maxima are slightly displaced with respect to the dissociation fronts by 0.02, 0.06, and 0.04×10^{-2} pc (0.1″, 0.3″, and 0.2″) towards the south for DF 1, DF 2, and DF 3, respectively. The AIB emission is highly structured across the atomic PDR. Specifically, the emission just past the IF is highly variable and shows additional local maxima at a distance of ~2″ from the northern part of the IF covered by the mosaic, in the S-SE direction of proplyd 203–504, and south of prolyd 203–506 (by about 0.2–1.2″). Lastly, in front of the IF, the AIB emission originating from the background face-on PDR, OMC-1, is enhanced in the eastern half of the FOV. This enhanced emission is part of a larger structure seen in the NIRCam AIB image (Fig. 1, red colour) and is not correlated with the foreground extinction (see Sect. 6.1). This suggests that the background PDR, OMC-1, displays an irregular surface that is affecting the amount of UV-excitation of the AIB carriers, as previously noted by, for example, Salgado et al. (2016).

The H_2 emission traces the dissociation fronts. The morphology of the H_2 lines (H_2 0–0 S(9), 1–0 S(1), 2–1 S(1), and 1–0 O(5) at 4.695, 2.122, 2.248, and 3.235 μm, respectively) are consistent with one another. H_2 emission is observed throughout the mosaic, with higher intensities found in the lower half of the mosaic that trace the molecular PDR. Enhanced emission is also observed in the molecular PDR at 2.21, 2.92, and 3.97×10^{-2} pc (11.03″, 14.55″, and 19.80″) from the IF, which subsequently

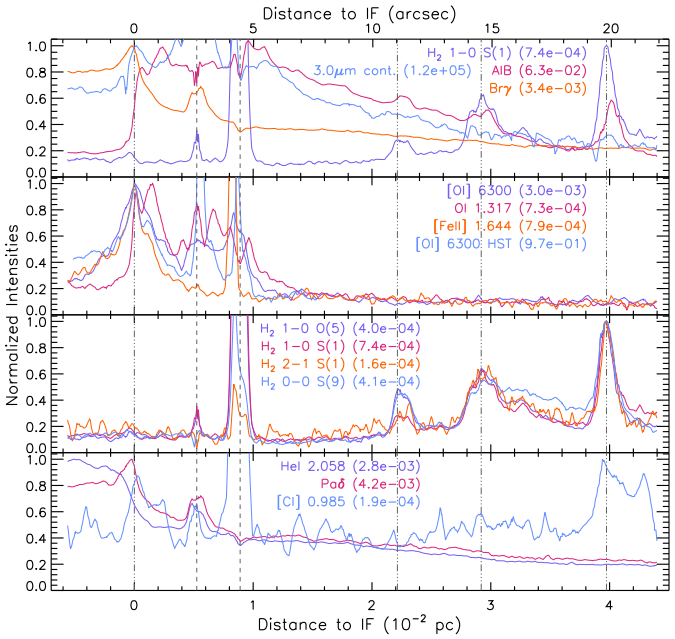

Fig. 9. Normalised line intensities as a function of distance to the IF (0.228 pc or 113.4″ from θ^1 Ori C) along a cut crossing the NIRSpec mosaic (see also Figs. 1 and 7 for the location of the cut). Normalisation factors are listed between brackets for each intensity. As the cut is not perpendicular to the IF and distances are given along the cut, a correction factor of cos(19.58°)=0.942 needs to be applied to obtain a perpendicular distance from the IF. No extinction correction is applied. For reference, we show the extinction corrected [O I] 6300 Å emission observed by Weilbacher et al. (2015) in purple and the [O I] 6300 Å emission observed by Bally et al. (2000) in light blue along the same cut. The dash-dot-dot-dot vertical lines indicate the position of the IF, DF 1, DF 2, and DF 3 respectively from left to right. The dashed vertical lines indicated the location of the proplyds 203–504 (left) and 203–506 (right). Units are erg cm^{-2} s^{-1} sr^{-1} except for the 3.0 μm continuum which is in MJy sr^{-1} and the HST [O I] 6300 Å emission which is in counts s^{-1}.

defines three dissociation fronts in the edge-on PDR. The intensity of these four H_2 lines peak at DF 3, followed by DF 2 and DF 1. Towards the northern part of the atomic PDR, we detect enhanced H_2 emission in the eastern half of the mosaic. Additionally, as for the AIB emission, in the region in front of the IF, we detect enhanced H_2 emission in the eastern half of the mosaic. We note that this emission is originating from the background face-on PDR in the molecular cloud, OMC-1.

The peak [Fe II] 1.644 μm emission is co-spatial with the peak [O I] 6300 Å emission. This is consistent with observations with MUSE by Weilbacher et al. (2015, extinction-corrected) and by HST from Bally et al. (2000, not extinction-corrected), indicating [Fe II] is an excellent tracer of the IF. The drop in [Fe II] intensity away from the IF is sharper than the drop in the MUSE [O I] 6300 Å intensity due to the lower angular resolution of the latter. The IF towards the west of the mosaic is more pronounced (i.e. larger intensity variation over a smaller area) than towards the east, consistent with the sharper transitions seen along a cut perpendicular to the bar, but west of the NIRSpec mosaic (Habart et al. 2024). On smaller spatial scales, both tracers exhibit almost identical profiles along the IF.

The [Fe III] 3.229 μm emission is detected in front of the IF and thus inside the H II region. The sharp drop in [Fe II] intensity towards θ^1 Ori C is likely caused by the transition from Fe II to predominantly Fe III in front of the IF.

The overall morphology of the He I emission lines is the same, although small differences are observed between the measured transitions (see Sect. 6.2). He I emission is observed throughout the mosaic, peaking closest to θ^1 Ori C, and displays a different spatial profile compared to that of the H I emission. Closest to θ^1 Ori C, its intensity is roughly constant or decreases slightly with distance from θ^1 Ori C. We note that the NIRSpec mosaic covers only a small part of the Huygens H II region and, thus, likely misses the real He I emission peak. Subsequently, it drops rapidly. This sudden decrease in intensity starts before the IF, where the H I intensity starts to increase. In contrast to [Fe II] and H I , this rapid drop is less sharp and already transitions to a slow steady decline at 0.15×10^{-2} pc (0.74″) after the IF.

The O I 1.317 μm emission peaks just beyond the IF and, overall, drops off sharply with increasing distance from the IF. This transition arises from O I in the neutral gas that is UV-pumped to its upper level, resulting in peak emission just beyond the IF. We do not observe enhanced emission in the direction of θ^2 Ori A (located to the east of the mosaic), suggesting that θ^1 Ori C is the main source of UV radiation. The structure seen in the [Fe II] emission along the IF is mimicked (but offset) by the O I 1.317 μm emission. The latter also exhibit a secondary, slightly weaker, ridge south of the primary ridge, at a small angle with the primary ridge (about 14 degrees), as well as enhanced emission towards the eastern edge of the IF, neither of which are prominently seen in [Fe II] or [O I] 6300 Å, albeit both show slightly enhanced emission near the peak of the secondary ridge (also offset, Fig. 8). The O I 1.317 μm emission displays filamentary structure between 3–6″ south of the IF, south of the proplyd 203–504, and surrounding the proplyd 203–506 (Fig. 8). These filaments' projections resemble a triangle with the strongest filament (N-SE filament) being parallel to the secondary ridge. These filaments are not seen in [Fe II] emission, which traces the IF. However, the SE-NW and the N-SE filaments do show weak emission in [O I] 6300 Å (Bally et al. 2000) and enhanced AIB emission is seen in part of the SE-NW filament. Two other fluorescent transitions within our wavelength coverage, the O I 1.129 μm and N I 1.2292 μm transitions, exhibit the same spatial distribution as the O I 1.317 μm emission (Fig. 8). The filamentary structure in the SE-NW direction towards proplyd 203–504 is associated with this proplyd (Sect. 5.2). While the lower half of the filamentary structure directed in the E-W direction may be aligned with the southern jet from proplyd 203–506 as seen in [Fe II], the top half is clearly offset from this jet by ∼16 degrees. We note this filament is slightly bent.

The spatial distribution of the [C I] 0.985 μm line is unique (Fig. 9): the observed variations in its intensity are only half of those seen in other tracers (excluding the proplyds) and it exhibits a 'flat' profile with local maxima just beyond the IF, and at the proplyds, DF 2, and DF 3 (though not at DF 1). We thus confirm that the C I originates in the neutral gas beyond the IF. The [C I] line shows enhancements at 2 out of the 3 H_2 dissociation fronts, similar to the results of Walmsley et al. (2000), but over a much larger distance scale. In contrast to Walmsley et al. (2000, due to their lower angular resolution), [C I] 0.985 μm exhibits a local maximum just beyond the IF (co-spatial with the double ridge seen in O I 1.317 μm), which is absent in H_2 and reflects the much smaller scale size near the IF.

Lastly, the continuum emission at 3 μm is strong in the H II region (see Figs. 7 and 9) due to the enhanced contribution of free-free emission and free-bound emission. An increase in intensity occurs near the IF, resulting in a local peak, co-spatial with the O I 1.317 μm peak emission. The continuum emission

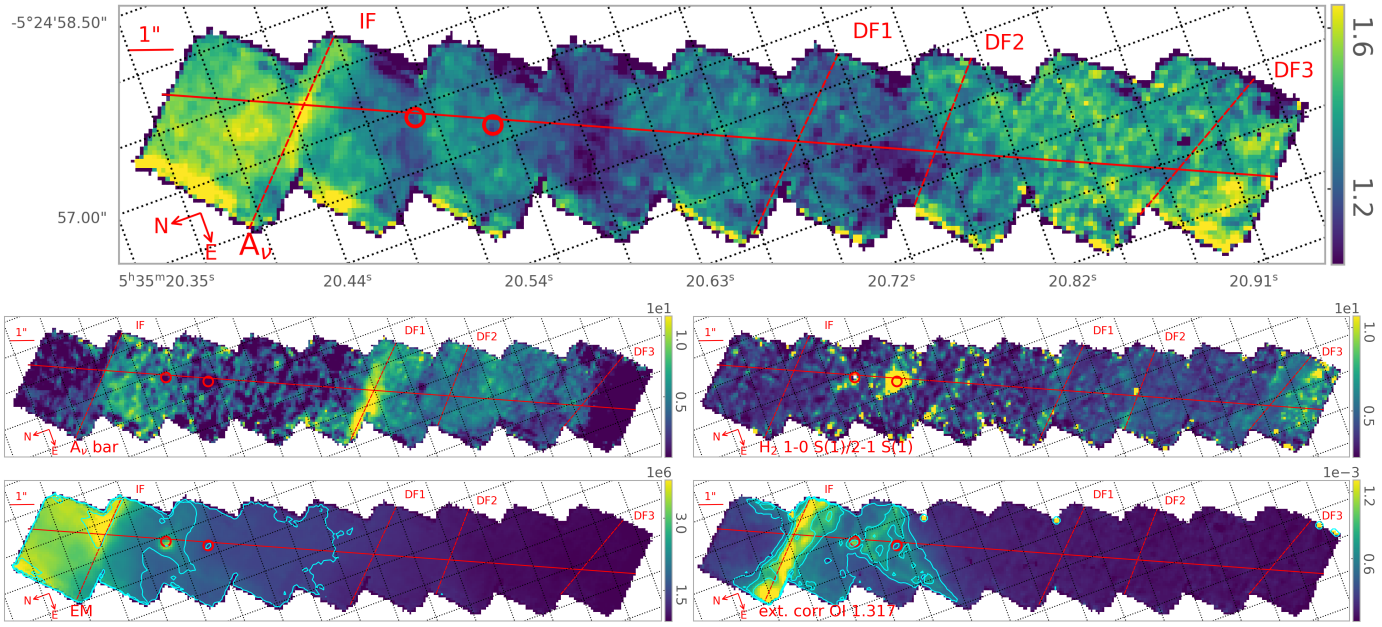

Fig. 10. Maps of the visual line of sight foreground extinction A_V (Sect. 6.1, top), the visual line of sight internal PDR extinction $A_{V_{\rm bar}}$ (Sect. 6.4, middle left), the H_2 1–0 S(1)/2–1 S(1) ratio (Sect. 6.4, midle right), the Emission Measure (EM; in units of pc cm^{-6}, Sect. 6.1, bottom left), and the extinction corrected O I 1.317 μm (ext. corr. O I 1.317 μm; in units of erg cm^{-2} s^{-1} sr^{-1}, bottom right). We set the colour range from the bottom 0.5% to the top 99.5% of data for each map, excluding values of zero, edge pixels, and the two proplyds. White pixels inside the mosaic indicate values of zero reflecting issues with the data. The nearly horizontal red line indicates the NIRSpec cut and the nearly vertical red lines indicate from left to right the IF and the DFs (DF 1, DF 2, DF 3). The two proplyds are indicated by the circles. Contours show the 55, 78, and 98% of the data for EM, and 77.9, 90.2, and 96 for O I 1.317 μm (see acknowledgments for data availability).

remains strong throughout the atomic PDR and displays small-scale variations that mimic those seen in the AIB emission (see also Appendix C). This indicates that the continuum emission in the PDR is dominated by emission from stochastically heated very small grains and/or by blended overtone and combination bands of PAHs, consistent with previous reports (Sellgren 1984; Allamandola et al. 1989). In addition, very strong continuum emission is detected towards the proplyd 203–504[17]. The continuum emission slowly decreases deeper into the molecular PDR due to the geometrical dilution of the radiation field.

5.2. Variations in protoplanetary disks

Two proto-planetary disks are present within the NIRSpec mosaic: the bright proplyd 203–504 and the silhouette disk 203–506 (Fig. 1, Bally et al. 2000). The 203–504 proplyd shows strong emission from H I recombination lines, He I, the fluorescent O I and N I lines, [C I] 0.985 μm, and H_2, and enhanced AIB emission. A filamentary structure starting at this proplyd and extending towards the SE direction is seen in the H I recombination lines. This SE-NW filament has been reported by Bally et al. (2000) in Hα and [O I] 6300 Å, being identified as a monopolar jet associated with the proplyd. The fluorescent lines also show a filamentary structure associated with this jet, but while this emission is parallel to the filament seen in H I , it is offset to the west by ∼0.2″. No enhanced [Fe II] emission is observed in this filament. Enhanced emission in the H I recombination lines is also seen towards the SSW of the proplyd.

The proplyd 203–506 is discussed in detail by Berné et al. (2024) and Berné et al. (2023). In addition to these authors' results, we report that the proplyd exhibits strong emission in [O I] 6300 Å and [C I] 0.985, and the disk is seen in absorption in He I and the fluorescent O I and N I lines. The [Fe II] emission is bright perpendicularly to the major axis of the silhouette disk 203–506, and on both sides, tracing the launching zone of a faint collimated jet observed before in [O I] 6300 Å HST images (Bally et al. 2000). Extending in the jet direction, towards the north-west and south-east, we observe enhanced [Fe II] emission, with the north-west component being much brighter than the south-east component. This is suggestive of a Herbig-Haro object being associated with the proplyd jet.

6. Deriving physical parameters

6.1. H I recombination lines

The H I recombination lines provide an estimate of the foreground extinction by comparing the observed ratios with those from case B recombination theory assuming an electron temperature of 10 000 K[18], an electron density of n_e = 1000 cm^{-3} and no radiation field (Prozesky & Smits 2018). We use the ratio of Paschen δ and Brackett γ. Both lines are among the strongest H I lines observed with detector NRS1 and have a large wavelength difference. We adopt the NIR extinction curve from Gordon et al. (2023) for an R_V = 5.5 (Cardelli et al. 1989). The resulting foreground visual extinction, A_V, varies between roughly 0.9 and 1.9 magnitude, corresponding to c(Hβ)[19]

[17] The 'extended' 3 μm continuum emission near proplyd 203–504 are the wings of the point spread function (PSF).

[18] Here we have adopted an electron temperature for our analysis of 10 000 K. Adopting a temperature instead of 9000 K (8500 K) would increase the theoretical Br γ/Pa δ line ratio by ∼1.4% (2.2%) resulting in an average decrease in A_V of 3.5% (5.2%).

[19] c(Hβ) = $\log(\frac{I_{0,H\beta}}{I_{\rm obs,H\beta}})$ with $I_{0,H\beta}$ the surface brightness in the absence of extinction and $I_{\rm obs,H\beta}$ the observed surface brightness.

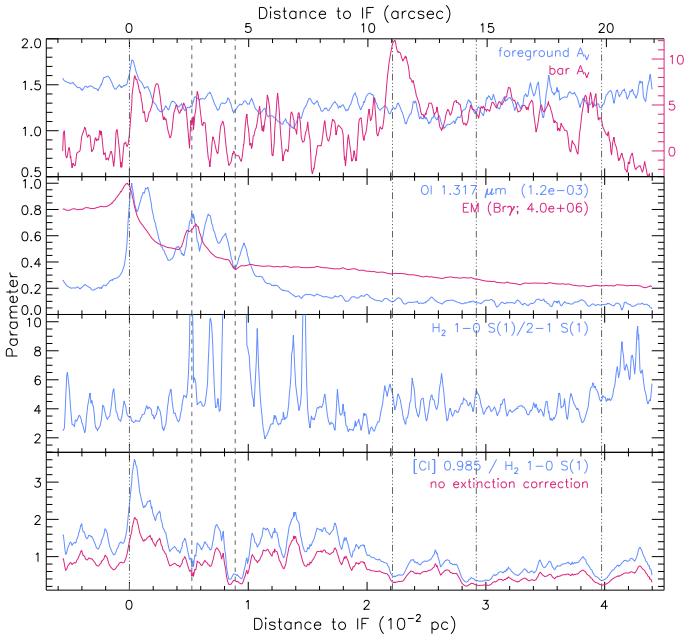

Fig. 11. Foreground extinction (top panel, left y-axis), internal PDR extinction (top panel, right y-axis), normalised O I 1.317 μm line intensity and emission measure (second panel), and line intensity ratios (lower two panels) as a function of distance to the IF (0.228 pc or 113.4″ from θ^1 Ori C) along a cut crossing the NIRSpec mosaic (see Fig. 1). Normalisation factors are listed between brackets where applied. As the cut is not perpendicular to the IF and distances are given along the cut, a correction factor of cos(19.58°)=0.942 needs to be applied to obtain a perpendicular distance from the IF. Foreground extinction correction is applied to determine bar A_V ($A_{V_{\rm bar}}$) and for the line intensities and ratios depicted in blue colour. The dash-dot-dot-dot vertical lines indicate the position of the IF, DF 1, DF 2, and DF 3 respectively from left to right. The dashed vertical lines indicated the location of the proplyds 203–504 (left) and 203–506 (right) (see acknowledgments for data availability).

of 0.4–0.8 when using the extinction curve of Blagrave et al. (2007, Figs. 10 and 11). To first order, the derived foreground extinction decreases slightly with distance from θ^1 Ori C up to about a distance of $\sim 2.6 \times 10^{-2}$ pc (~13″) from the IF, after which it slowly increases. It is also slightly structured, with weak local minima near, roughly, 0.4, 1.4, and 2.6×10^{-2} pc (~2″, ~7″, and ~13″) from the IF. The derived extinction values are overall consistent with Weilbacher et al. (2015), but the morphology differs slightly. Specifically, neither the increase in the extinction past roughly $\sim 2.6 \times 10^{-2}$ pc (~13″) from the IF nor the local minima are observed by Weilbacher et al. (2015). In addition, Weilbacher et al. (2015) derived a slightly increased extinction at the western side of the NIRSpec mosaic in the atomic PDR. These discrepancies likely results from the combination of 1) the lower angular resolution observations of Weilbacher et al. (2015, seeing of 0.67″ to 1.25″) resulting in a spatial averaging weighted by the emissivities, and 2) remaining systematic artefacts in the data set that are not captured by the comparison of these line fluxes in the individual dither observations (which agree within 0.5%).

A caveat of the presented extinction analysis is the following. The extinction is a summation of absorption and scattering out of the line of sight. For the Bar, we have an extended background light source and the extinction is due to foreground extended dust. If the background light source and dust layer are both uniformly distributed, the light scattered outside the line of sight will be compensated by the light scattered in the line of sight for a spherically symmetric, unresolved source. Therefore, the net attenuation will only be due to absorption. However, the actual situation is more complex. Both the background light source and the dust are distributed heterogeneously and it is impossible to estimate the actual geometry. But in general, the attenuation will be reduced by the light scattered into the line of sight (cf. Code 1973). While the general trend of the determined extinction, A_V, should not be affected very much, it does affect the quantitative value of A_V obtained from the standard extinction curve, which is estimated from observations of background stars. As the albedo is still around ~0.5 in the NIR, the absorption will only be a half of extinction. The spectral dependence is also different between the absorption and scattering. However, this should not make a large difference because of the short spectral range considered and small attenuation in question. Despite this caveat, we use these derived values for the foreground extinction to the Bar and employ the NIR extinction curve for an $R_V = 5.5$ from Gordon et al. (2023)[20].

WeAs obtain an estimate of the emission measure, EM, from the Brackett γ surface brightness using Eq. (D.1). The emission measure ranges within $0.84–4.15 \times 10^6$ pc cm^{-6} (Figs. 10 and 11; see Table 1 for the five templates). The obtained EM in front of, and at the IF are consistent with those reported by Walmsley et al. (2000) for similar regions north-east of the NIRSpec mosaic (their positions A and B). Assuming a depth of the ionised bar of 20″ (0.05 pc; Walmsley et al. 2000), we obtain a rms electron density of the order of 9000 cm^{-3}.

6.2. HeI recombination lines

The distinct radial profiles for the He I and H I recombination lines (Figs. 9 and 12) indicate, for the first time, that the He and H ionisation fronts are clearly separated in the Huygens region. While the location of the H-IF is well defined (i.e. peak H I emission at 0.2274 pc or 113.276″ from θ^1 Ori C), the location of the He-IF is somewhat uncertain as the NIRSpec radial profiles do not extend very deep into the Huygens region. However, the He I 1.70 μm intensity remains fairly constant up to about 15″ away from the IF (Marconi et al. 1998). Hence, we quantify the displacement between the H-IF and He-IF by the distance between the peak emission of the H I and He I recombination lines and find a displacement of approximately 0.5×10^{-2} pc or 2.5″ (Fig. 12). Only the He I 1.083 μm emission gives a slightly smaller displacement of 0.36×10^{-2} pc (1.8″).

These results are consistent with Cloudy modelling (Ferland et al. 2017) of the Orion Nebula. We adopt the model parameters derived from the detailed fits of the optical lines originating from the ionised gas by Shaw et al. (2009) and Pellegrini et al. (2009)[21]. In a radial direction from θ^1 Ori C, this model predicts the H IF at a distance of ~0.254 pc and a displacement between

[20] This extinction curve has A_λ/A_V values of 5.075×10^{-1}, 2.711×10^{-1}, 1.736×10^{-1}, 1.258×10^{-1}, 9.838×10^{-2}, 7.995×10^{-2}, 6.695×10^{-2}, 5.747×10^{-2}, and 5.037×10^{-2} at 1.0, 1.5, 2.0, 2.5, 3.0, 3.5, 4.0, 4.5, and 5.0 μm respectively and 1.508×10^{-1} at 2.2 μm.

[21] It should be noted that the analysis from Shaw et al. (2009) and Pellegrini et al. (2009) required the models to reproduce the projected distance of the IF, which was defined based on the peak emission of [S II] at a projected distance from θ^1 Ori C of 111″. These authors adopt a distance of 437 pc for the Bar and thus the IF is located at a projected distance of 0.235 pc. In this paper, we instead define the IF by the peak intensity of the [O I] 6300 Å and [Fe II] 1.644 μm emission lines at 113.4″ or 0.228 pc from θ^1 Ori C (given the adopted distance of 414 pc). This small difference should, however, not considerably affect the spatial offset between the He and H ionisation front.

Table 1. Physical conditions derived for the five templates.

		Sect.	H II region	Atomic PDR	DF 1	DF 2	DF 3
A_V [(1)]		6.1	1.5	1.3	1.2	1.2	1.4
$A_{V_{\rm bar}}$ [(2)]		6.4	–	2.84	8.55	3.67	1.28
$A_{V_{\rm bar},I}$ [(3)]		6.4	0	5.49	36.1	7.44	2.30
EM (Brγ)	(10^6 pc cm^{-6})	6.1	3.3	2.3	1.2	1.1	0.9
T (C I)	(K)	6.5, G	~2500	~2300	~2900	~6800	~5600
EM×$T_3^{-0.6}$ (C I)	(cm^{-6} pc K$^{-0.6}$)	6.5, G	1034±18	2635±40	725±11	938±15	1589±17
EM (C I)	(pc cm^{-6})	6.5, G	1772^{+247}_{-240}	4334^{+602}_{-539}	1370^{+451}_{-401}	2953^{+790}_{-576}	4477^{+472}_{-350}
3.4/3.29 AIB [(4)]		6.6.1	0.11	0.09	0.10	0.15	0.18
4.64/ΣAIB [(5)]	(10^{-3})	6.6.1	8.2	6.3	6.1	2.8	2.4
4.64/3.29 AIB	(10^{-3})	6.6.1	16.0	12.1	11.9	6.0	5.6
4.64/3.40 AIB	(10^{-2})	6.6.1	20.5	22.5	15.8	5.4	4.1
FWHM 3.29 AIB	(cm^{-1})	6.6.2	39.3	37.4	38.1	41.2	42.4

Notes. We provide the H_2 excitation temperatures and column densities in Table 4. [(1)]foreground extinction; [(2)]internal PDR extinction calculated using the foreground formalism (see Fig. 14); [(3)]internal PDR extinction calculated using the intermingled formalism; [(4)]ratio of the integrated intensities of the (3.39+3.40+3.42)/(3.29) AIBs using the Gaussian decomposition method. [(5)]ΣAIB refers to the sum of all Gaussian AIB components in the 3.2–3.7 μm range.

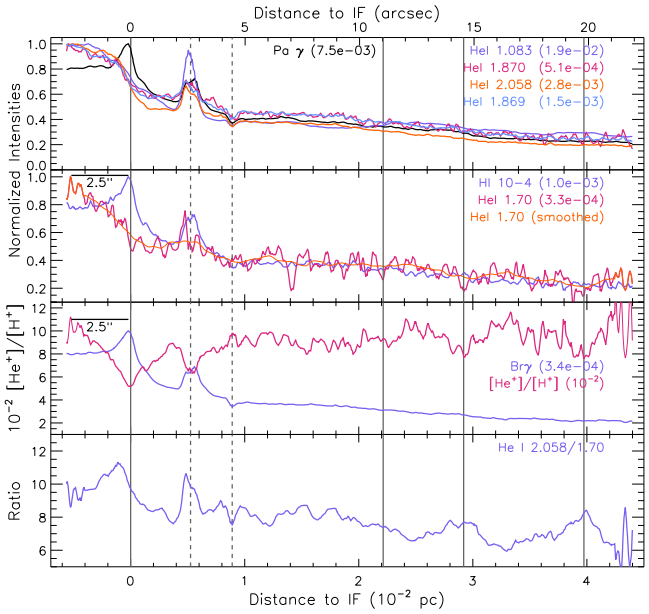

Fig. 12. Analysis of the He I and H I radial profiles as a function of distance to the IF (0.228 pc or 113.4″ from θ^1 Ori C) along a cut crossing the NIRSpec mosaic (see Fig. 1). As the cut is not perpendicular to the IF and distances are given along the cut, a correction factor of cos(19.58°)=0.942 needs to be applied to obtain a perpendicular distance from the IF. Top two panels: observed normalised line intensities of selected transitions. Normalisation factors are listed between brackets. No extinction correction is applied. Units are in erg cm^{-2} s^{-1} sr^{-1}. Third panel: the [He$^+$]/[H$^+$] abundance. The normalised Br γ radial profile is shown for reference. Normalisation factors are listed between brackets. Bottom panel: the He I 2.058/1.70 radial profile. The dash-dot-dot-dot vertical lines indicate the position of the IF, DF 1, DF 2, and DF 3, respectively, from left to right. The dashed vertical lines indicated the location of the proplyds 203–504 (left) and 203–506 (right).

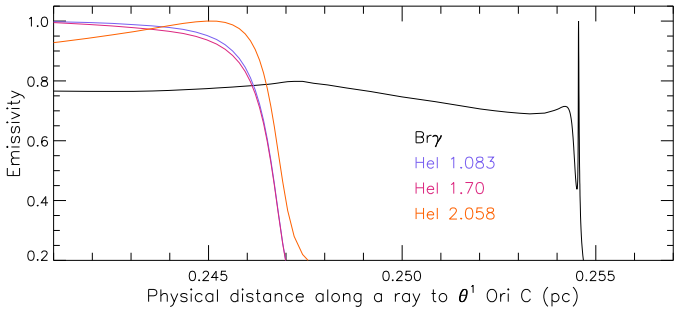

Fig. 13. Emissivity profile of selected transitions as a function of the physical distance along a ray from θ^1 Ori C and perpendicular to the Bar given by a Cloudy model employing the physical parameters derived by Shaw et al. (2009) and Pellegrini et al. (2009). See Sect. 6.2 for details.

the emissivity of selected H and He transitions of ~0.007 pc (Fig. 13). We note that the latter distances are physical distances along a ray into, and perpendicular to, the Bar from θ^1 Ori C as we did not model the corresponding radial surface brightness profiles of selected transitions as a function of the projected distance from θ^1 Ori C. These differences result in an offset between the model IF and our observations. We conclude therefore that the model calculations are in good agreement with the He I and H I observations reported here.

Based on the radial profiles of He I 1.70 μm and H I 10-4, we can estimate the [He$^+$]/[H$^+$] abundance following Marconi et al. (1998, see Appendix E). Figure 12 shows the radial profile along the NIRSpec cut. Over most of the radial profile, the [He$^+$]/[H$^+$] abundance is fairly constant. However, due to NIRSpec's angular resolution, we also detect two strong dips. The dip at the IF reflects the displacement of the H-IF and He-IF, while the second dip is co-spatial with the proplyd 203–504. We note that the He I emission near this proplyd depends on the transition considered. Away from the IF and this proplyd, we derive a [He$^+$]/[H$^+$] abundance of 0.094 ± 0.009. While previous observations did not resolve the difference in the H and He ionisation structure in the Huygens region, these studies obtain a similar [He$^+$]/[H$^+$] abundance because of spatial averaging (e.g. Osterbrock et al. 1992; Esteban et al. 1998, 1994; Marconi et al. 1998; Baldwin et al. 2000; Walmsley et al. 2000; Blagrave et al. 2007). Recent refinements in the atomic data

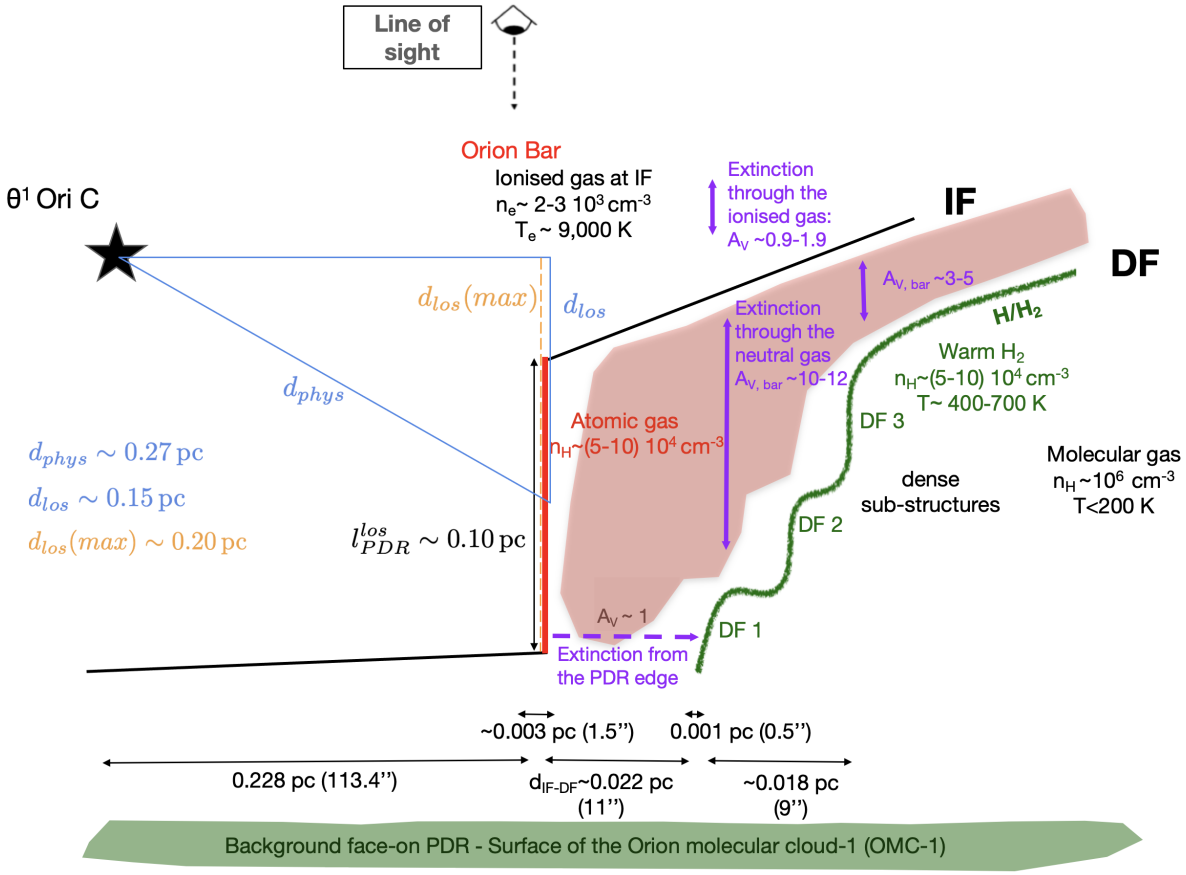

Fig. 14. Schematic overview of the Bar as inferred from JWST and other observations (e.g. Jansen et al. 1995; Wen & O'dell 1995; O'Dell 2001; Pellegrini et al. 2009). It shows the main features discussed in this paper and Habart et al. (2024, based on NIRCam and MIRI imaging). Given the complexity of the PDR surface, parameters derived in this paper are specific for the NIRSpec mosaic. We note that for clarity, the dimensions perpendicular to the bar are not to scale; the true spatial scales are explicitly given in the annotations. In addition, the sketch does not include foreground material, that includes a layer of ionised gas O'Dell et al. (2020) and, closer to the observer, layers that are grouped together under the designation as the Veil (e.g. Rubin et al. 2011; Boersma et al. 2012; van der Werf et al. 2013; Pabst et al. 2019, 2020).

(Del Zanna & Storey 2022) may necessitate a new analysis of the [He$^+$]/[H$^+$] abundance ratio to take full advantage of the high quality of the NIRSpec data.

We furthermore confirm the observed He I 2.058/1.70 ratio as detected by Marconi et al. (1998). This ratio ranges between about 7–10 (Fig. 12). These authors argue that one can compare this ratio with the model predictions of Smits (1996), as the He I 1.70 μm transition arises from the same upper level as the 4471 Å transition used for normalisation in the model calculations. The observed value is significantly enhanced with respect to the model prediction, which Marconi et al. (1998) potentially attributes to the neglect of collisional effects and line trapping.

Lastly, we can obtain an estimate of the electron temperature, T_e, from the He I line ratios 2.1649/2.1137 and 2.1649/2.118 based on the diagnostic diagram of Martín-Hernández et al. (2003, their Fig. 7b). We find an electron temperature, T_e, of about 9000–9500 K and an optical depth of the 2^3S metatstable level, τ_{3890}, of ~0 for each of the template spectra except for DF 1 for which we find an electron temperature, T_e, of about 8000 K.

6.3. OI and NI fluorescent emission

6.3.1. Spatial and spectral characteristics

The fluorescent lines of O I at 1.129 and 1.317 μm arise from the partially neutral gas in the ionisation front from UV-pumping by 1027 and 1040 Å photons, respectively, followed by radiative decay. In addition, there are multiple indirect routes to pumping the upper levels of these lines. For example, Henney (2021) reported that roughly half of the pumping of the O I 8446 Å fluorescence line arises from more excited levels. Hence, a detailed investigation is warranted to assess the relative importance of the various pumping routes. Assuming solely pumping by the strongest UV resonance lines, similar intensities are expected for both IR transitions. Yet, the O I 1.317 μm intensity is, on average, about 3 times the O I 1.129 μm intensity in the IF and the filamentary structure in the atomic PDRs (i.e. where the O I 1.317 μm intensity >15σ). This is in contrast with previous results. Indeed, Marconi et al. (1998) reported that the 1.129 μm line is 1) equal in strength to the 1.317 μm line at two positions – from which they concluded that pumping of the upper level of the 1.129 μm transition by resonantly scattered Lyman β photons (1026 Å) is negligible – and 2) stronger than the 1.317 μm line at one position, which we do not see anywhere in the NIRSpec mosaic. Likewise, Walmsley et al. (2000) observed similar 1.129 and 1.317 μm line intensities at two positions, while a third position exhibited a stronger 1.317 μm intensity, albeit with a lower factor than observed in the NIRSpec data (1.317/1.129 ~ 1.4). As these observations probe different positions of a highly structured PDR, seeing variations across the Bar is perhaps not that surprising. However, the origin of the enhanced O I 1.317/1.129

Table 2. Parameters employed or derived for the Orion Bar.

Parameter	Value	Reference
Distance	414 ± 7 pc [(a)]	Menten et al. (2007)
	1″= 0.002 pc	
Projected distance, $d_{\rm proj}$, between θ^1 Ori C and the IF [(b)]	0.228 pc	Sect. 5.1
Physical distance, $d_{\rm phys}$, between θ^1 Ori C and the IF	~0.27 pc	Sect. 6.3.2
Transverse size $l^{\rm los}_{\rm PDR}$	~0.10 pc	Sect. 6.3.2
Line-of-sight distance, $d_{\rm los}$, between θ^1 Ori C and the IF		Sect. 6.3.2
Average	~0.15 pc	
Minimum	~0.05 pc	
Maximum	~0.20 pc	
Projected distance between He-IF and H-IF [(c)]	0.5×10^{-2} pc; 2.5″	Sect. 6.2
Projected distance between IF and DF d_{IF-DF} [(c,d)]	$(2.2, 2.9, 4.0) \times 10^{-2}$ pc	Sect. 5.1
	11.0″, 14.5″, 19.8″	
G_0 at IF	$\sim(2.2–7.1) \times 10^4$	Sect. 6.3.2, Appendix F
Width IF at peak G_0	$(0.22–0.34) \times 10^{-2}$ pc	Sects. 5.1, 6.3
	1.1″ – 1.7″	
Condition for face-on PDR to dominate G_0	$d_{\rm proj} \geq 0.24$ pc	Sect. 6.3.1
FUV dust cross-section σ_H	6.5×10^{-22} cm^2 / H	Cardelli et al. (1989); Blagrave et al. (2007) Schirmer et al. (2022)
$R_V = A_V/E(B-V)$	5.5	Cardelli et al. (1989); Blagrave et al. (2007)
A_V/N_H	3.5×10^{-22} mag/cm^{-2}	Cardelli et al. (1989); Blagrave et al. (2007)
Total IR emission $L_{\rm IR}$	9.5×10^3 L$_\odot$	Salgado et al. (2016)
Foreground extinction A_V	0.9–1.9 mag	Sect. 6.1
Emission measure EM (Brγ)	$(0.84–4.15) \times 10^6$ pc cm^{-6}	Sect. 6.1
Rms electron density $n_{e,\rm rms}$ near IF (Brγ)	~9000 cm^{-3}	Sect. 6.1
Density at the IF n_e [(d)]	$2–3 \times 10^3$ cm^{-3}	Weilbacher et al. (2015)
Temperature at the IF T$_e$ [(d)]	$\sim 9 \times 10^3$ K	Weilbacher et al. (2015)
Density in atomic PDR n_H (AIB emission) [(d)]	$(5–10) \times 10^4$ cm^{-3}	Habart et al. (2024, Sect. 5.1)
Density from NIR H$_2$ n_H	$(3.5) \times 10^4$ to 10^5 cm^{-3}	Sect. 6.4
Temperature at the DF T	~400–700 K	Van De Putte et al. (2024) Allers et al. (2005)
Emission measure EM ([C I] 0.984 μm)	$(1.1–2.8) \times 10^5$ pc cm^{-6}	Sect. 6.5

Notes. [(a)]See Habart et al. (2024) for a discussion on the adopted distance. [(b)]IF is defined by the peak emission of the [O I] 6300 Å and [Fe II] 1.644 μm emission. [(c)]Projected distance along the NIRSpec cut. As the cut is not perpendicular to the IF, a correction factor of cos(19.58°)=0.942 needs to be applied to obtain a perpendicular distance from the IF. [(d)]Given the complexity of the PDR surface, parameters given are specific for the NIRSpec FOV. For average values across the entire Bar, see Habart et al. (2024).

ratio observed here and in one position of Walmsley et al. (2000) is unclear and requires further investigation.

The observed O I 1.317 μm intensity decreases with distance from the ionisation front (Figs. 7 and 9). The location of the cut, crossing both the primary and secondary ridge, results in a very sharp, double-peaked profile just beyond the ionisation front. In addition, its radial profile shows multiple peaks between 0.34 and 1.07×10^{-2} pc from the IF (between 1.7″ and 5.3″), followed by a slow drop at larger distances. We note that the observed O I 1.317 μm intensity follows the [O I] 6300 Å intensity to some degree (Fig. 9). The ionisation front has a typical H I column density of 6×10^{18} cm^{-2} (Tielens 2005, Eq. (7.25)), corresponding to an optical depth in the O I UV pumping lines of ~30 (Marconi et al. 1998). Hence, the strongest UV resonance lines that pump the O I near-IR lines (i.e. 1027 and 1040 Å photons for respectively the 1.129 and 1.317 μm lines) are on the logarithmic part of the curve of growth in the PDR itself. We note that indirect pumping of these lines may involve weaker UV lines in different parts of the curve of growth. We attribute the multiple peaks to the presence of undulations in the Bar surface. The subtle differences in the intensity distribution of the O I 1.317 μm line and the [O I] 6300 Å line may reflect local acceleration zones of the gas in the ionisation front that Doppler shift unattenuated stellar photons into the UV pumping wavelengths of O I 1.317 μm ([O I] 6300 Å emission is due to collisional excitation). We note that for an intrinsic line width of 3 km s^{-1}, an acceleration by 1 km/s will increase the UV pumping photon flux by 30%. In addition, this area is known to host many collimated velocity flows (such as HH203, 204, and 528, e.g. Méndez-Delgado et al. 2021). Some of the observed difference may be related to these flows. We attribute the gradual decrease in both the O I 1.317 μm and the [O I] 6300 Å intensity beyond 1.07×10^{-2} pc from the IF (5.3″; Fig. 9) to the change over from an edge-on to a face-on geometry of the ionisation front, coupled with the geometric dilution of the incident UV field intensity. This transition from edge-on to face-on geometry occurs over a very small distance (~1″, 6×10^{15} cm). Lastly, we ascribe part of the prominent triangular region of enhanced O I 1.317 μm at $0.6–1.2 \times 10^{-2}$ pc (3–6″) behind the ionisation front (Fig. 8) to a local gas acceleration zone. As there is no counterpart in the [O I] 6300 Å line for the E-W filament, this acceleration must occur inside the PDR itself.

6.3.2. Bar geometry & strength of the FUV radiation at the PDR surface

It is well recognised that, on a global (10's of arcsec) scale, the Bar shows the expected stratification of an edge-on PDR with a clearly separated ionisation front, atomic region, H_2 dissociation front, and molecular zone on the sky (Tielens et al. 1993; Tauber et al. 1994; Hogerheijde et al. 1995; Bernard-Salas et al. 2012). This is well supported by these high resolution NIRSpec imaging data as well as by JWST NIRCam and MIRI imaging observations (Habart et al. 2024), Keck observations (Habart et al. 2023), and recent ALMA studies of the molecular emission (Goicoechea et al. 2016). Both this NIRSpec study (Fig. 7) and the other studies reveal that on a local (~arcsec) scale the Bar is highly structured as the FUV radiation field penetrates a clumpy PDR region. We expect that the width of the ionisation front as measured in the [O I] 6300 Å line and the near-IR O I (e.g. 1.317 μm) fluorescence lines is dominated by this small-scale structure. In the past, the observed width of these tracers has been interpreted in terms of a inclination angle of the Bar with respect to the line of sight (e.g. Marconi et al. 1998; Walmsley et al. 2000; Salgado et al. 2016) but this is really untenable given, for example, the structured appearance of the O I emission (Fig. 8), the H_2 dissociation fronts in the NIRSpec, NIRCam, and Keck maps (Fig. 7, Habart et al. 2023, 2024), and the ALMA HCO^+ maps (Goicoechea et al. 2016). The O I data can be used to derive a strict upper limit to the inclination of ~4° (e.g. Marconi et al. 1998; Walmsley et al. 2000, see Appendix F for details) but as exemplified by the NIRSpec maps (Fig. 7), there is no large-scale curvature associated with the Bar and it is essentially an edge-on, limb-brightened PDR.

We can use the obtained values for the optical depth at 100 μm from Salgado et al. (2016) to derive the geometry of the Bar. These authors observed the SED of the dust emission in the Bar over its entire wavelength range and were able to fit this SED with two modified blackbodies assuming optical thin emission. The Bar is very pronounced in the optical depth map of the warm component, τ_{warm}, with $\tau_{warm} \sim 1 \times 10^{-2}$ (Fig. 8 in Salgado et al. 2016). With the ratio of the extinction at 100 μm to the Hydrogen column density, A_{100}/N_H, being equal to 6.2×10^{-25} magn cm^{-2} H – atom^{-1} for an R_V of 5.5 (Draine 2011), we obtain $N_H = 1.75 \times 10^{22}$ H – atoms cm^{-2} which results in estimate of the transverse size of l^{los}_{PDR} of 0.10 pc for a density, n_H, of 5×10^4 cm^{-3}. This is consistent with model predictions of the Bar geometry (e.g. Tielens et al. 1993; Pellegrini et al. 2009). Using the observed size of the Bar (0.32 pc), the obtained transverse size of l^{los}_{PDR} then provides an estimate of the absorbing area A_{abs} of 0.033 pc^2 assuming a rectangular absorbing area. The obtained absorbing area then in turn provides an estimate of the physical distance between θ^1 Ori C and the IF, d_{phys}, for a given stellar luminosity from $A_{abs} = L_{IR}/(L_\star/(4\pi d^2_{phys}))$ as the total IR emission is a measure for the amount of stellar radiation absorbed by the Bar (e.g. Salgado et al. 2016). We adopt the higher stellar FUV luminosity of 2.7×10^5 L$_\odot$ employed by Salgado et al. (2016), as the lower stellar FUV luminosity does not provide physical results[22]. We obtain a physical distance between the θ^1 Ori C and the IF, d_{phys}, of 0.27 pc. Given the physical size of the IF, we assume this distance reflects the physical distance from the mid-point of the IF to θ^1 Ori C (Fig. 14). Given a projected distance between θ^1 Ori C and the IF, d_{proj}, of 0.228 pc, this constraints the distance between θ^1 Ori C and the mid-point of the IF projected along the line of sight, d_{los}, to 0.15 pc (Fig. 14). Consequently, θ^1 Ori C is located at a distance of 0.10 pc in front of the start of the IF along the line of sight and the depth of the Bar (end-point) from θ^1 Ori C along the line of sight is 0.20 pc (Fig. 14).

Finally, we can use the obtained values for the absorbing area, A_{abs}, to derive the strength of the FUV radiation field, G_0, following Salgado et al. (2016, Sect. 4.1). These authors equate the observed total IR emission to the product of the strength of the FUV radiation field, G_0, and the area at the surface of the PDR absorbing stellar radiation, A_{abs}. Employing the total IR emission reported by these authors, this results in a G_0 of 7.1×10^4. This value is consistent with Tielens & Hollenbach (1985b), who derived G_0 from an analysis of the [O I] and [C II] atomic fine-structure lines observed towards the Bar PDR, and slightly higher than the G_0 of 2.6×10^4 reported by Marconi et al. (1998), who derived G_0 based on their observations of the near-IR O I fluorescent lines. We further note that this G_0 is consistent with values derived from the NIRSpec O I 1.317 μm line assuming that the Bar is inclined at a 4° angle (see Appendix F).

6.4. Rotationally and vibrationally excited H_2 emission

H_2 emission is observed throughout the mosaic (see Fig. 7). We detect a large number of ro-vibrational lines in our data. For a detailed inventory of the observed H_2 lines and the spatial distribution of their emission, we refer the reader to Sect. 4.1 and Appendix B, and Sect. 5.1, respectively. We report the measured fluxes for selected H_2 lines detected in the five templates in Table 3. We note that the H_2 line intensity is strongest in DF 3, followed by DF 2, DF 1, atomic PDR, and H II region. This variation in intensity is also observed in the surface brightness line cut across the NIRSpec mosaic presented in Fig. 9. Moreover, there is an increase in H_2 emission at the position of the two proplyds. The in-depth analysis of the H_2 emission in proplyd 203–506 is discussed in Berné et al. (2024). Here, we focus on the H_2 emission observed in the five templates. We highlight that the H_2 emission observed in the H II region originates from the background face-on PDR in OMC-1 (see Fig. 14). The emission from this background face-on PDR was previously observed with Herschel in other PDR tracers, particularly in high-J CO, CH^+ lines (Parikka et al. 2018) and [O I] 63 and 145 μm and [C II] 158 μm (Bernard-Salas et al. 2012), as well as, with *Spitzer* in AIB emission (Knight et al. 2022). In contrast, the H_2 emission observed in the atomic PDR and the three dissociation fronts originates from the edge-on PDR in the Bar itself.

The H_2 lines are powerful tools to probe the physical conditions of the emitting region. We use the observed lines to probe the extinction within the PDR and density throughout the mosaic. While we estimate the foreground visual extinction, A_V, using the H I recombination lines (Sect. 6.1), we use the H_2 lines to measure the extinction in the neutral H I region of the bar using the foreground and intermingled formalisms, referred to as $A_{V_{bar}}$ and $A_{V_{bar},I}$ respectively. The foreground formalism assumes that the dust is in front of the region emitting H_2, whereas the intermingled formalism assumes that the dust is mixed with the gas emitting H_2. Comparison of the ratio of lines that arise from the same upper v and J state with the corresponding intrinsic flux ratio gives a measure of amount of extinction within the PDR ($A_{V_{bar}}$ and $A_{V_{bar},I}$). We use the ratio of the H_2 lines 1–0 S(1) and 1–0 O(5), which originates from the same upper level, corrected

[22] The physical distance is smaller than the projected distance when adopting the lower stellar FUV luminosity.

Table 3. Excerpt of intensities (observed and corrected for extinction using foreground and intermingled formalisms) and column densities of selected H_2 lines in v=0 and v=1 states as observed in the five templates.

Template	Line	Wavelength	Observed intensity	Extinction corrected intensity		Column density	
		(μm)	($\times10^{-5}$ erg cm^{-2} s^{-1} sr^{-1})			($\times10^{15}$ cm^{-2})	
				Foreground	Intermingled	Foreground	Intermingled
H II region	0–0 S(8)	5.0531152	$2.570^{2.649}_{2.491}$	$2.770^{2.855}_{2.685}$	–	$2.736^{2.820}_{2.652}$	–
H II region	0–0 S(9)	4.6946139	$6.290^{6.407}_{6.173}$	$6.816^{6.943}_{6.689}$	–	$4.131^{4.208}_{4.054}$	–
H II region	0–0 S(10)	4.4097910	$1.310^{1.378}_{1.242}$	$1.427^{1.502}_{1.353}$	–	$0.567^{0.596}_{0.537}$	–
H II region	0–0 S(11)	4.1810772	$3.350^{3.500}_{3.200}$	$3.670^{3.834}_{3.506}$	–	$1.008^{1.053}_{0.963}$	–

Notes. The complete table is available at the CDS.

Table 4. Column densities and excitation temperatures obtained from fitting the excitation diagrams of the H_2 lines observed towards the H II region, the atomic PDR, DF 1, DF 2, and DF 3 (Fig. 15).

	Foreground formalism		Intermingled formalism	
H_2 series	N_{H_2} ($\times10^{18}$ cm^{-2})	T (K)	N_{H_2} ($\times10^{18}$ cm^{-2})	T (K)
		H II region		
0–0 S	0.19 ± 0.05	2753 ± 172	–	–
1–0 Q	0.24 ± 0.14	2391 ± 376	–	–
1–0 O	3.59 ± 6.45	1135 ± 335	–	–
1–0 S	0.40 ± 0.10	2034 ± 107	–	–
1–1 S	0.08 ± 0.03	3813 ± 223	–	–
		Atomic PDR		
0–0 S	0.12 ± 0.04	3393 ± 224	0.12 ± 0.05	3396 ± 224
1–0 Q	0.61 ± 0.35	1996 ± 284	0.62 ± 0.36	1996 ± 284
1–0 O	11.5 ± 15.7	969 ± 207	10.9 ± 16.2	967 ± 207
1–0 S	0.96 ± 0.32	1598 ± 109	0.99 ± 0.33	1592 ± 108
1–1 S	0.13 ± 0.08	3527 ± 413	0.14 ± 0.09	3531 ± 414
		DF 1		
0–0 S	0.58 ± 0.09	3033 ± 119	0.89 ± 0.15	3105 ± 121
1–0 Q	9.83 ± 2.96	1477 ± 88	17.8 ± 5.36	1481 ± 88
1–0 O	10.7 ± 11.0	1326 ± 259	22.9 ± 20.35	1273 ± 238
1–0 S	5.07 ± 3.07	1617 ± 206	10.5 ± 6.49	1534 ± 189
1–1 S	0.27 ± 0.04	3699 ± 100	0.40 ± 0.06	3795 ± 100
		DF 2		
0–0 S	0.73 ± 0.09	2996 ± 84	0.75 ± 0.10	3001 ± 84
1–0 Q	4.10 ± 2.54	1728 ± 204	4.26 ± 2.64	1728 ± 204
1–0 O	8.23 ± 8.62	1437 ± 309	8.66 ± 9.09	1432 ± 306
1–0 S	5.46 ± 2.94	1723 ± 193	5.77 ± 3.12	1712 ± 191
1–1 S	0.40 ± 0.08	3631 ± 124	0.41 ± 0.08	3638 ± 124
		DF 3		
0–0 S	0.89 ± 0.10	2852 ± 57	0.89 ± 0.10	2852 ± 57
1–0 Q	6.18 ± 5.61	1527 ± 218	6.21 ± 5.63	1527 ± 219
1–0 O	16.7 ± 27.8	1151 ± 320	16.7 ± 28.0	1151 ± 320
1–0 S	14.0 ± 12.1	1180 ± 163	14.1 ± 12.2	1179 ± 163
1–1 S	0.65 ± 0.13	3156 ± 110	0.65 ± 0.13	3157 ± 110

Notes. Except for the H II region, all the H_2 lines in the excitation diagrams are first corrected for foreground visual extinction and subsequently for extinction within the PDR using the foreground and intermingled formalisms. In the H II region, the lines are only corrected for the foreground visual extinction.

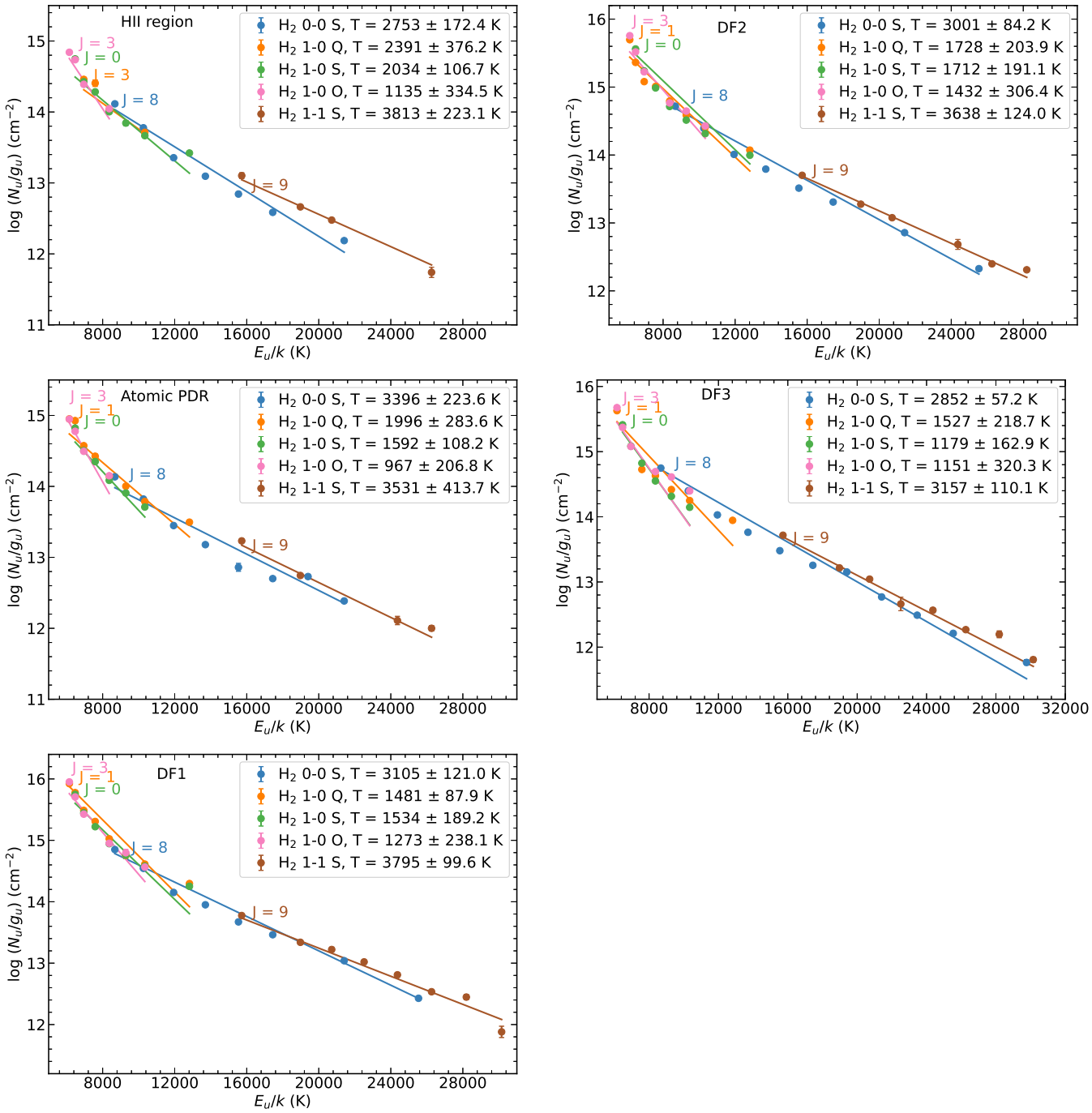

Fig. 15. Excitation diagrams of H_2 lines observed towards the H II region, atomic PDR, DF 1, DF 2, and DF 3. With the exception of H II region, the H_2 lines in the excitation diagrams are first corrected for foreground visual extinction and subsequently for extinction within the PDR using the intermingled formalism. In H II region the lines are only corrected for the foreground visual extinction. The excitation diagrams for the 0–0 S, 1–0 Q, 1–0 S, 1–0 0, and 1–1 S levels of H_2 are fitted using a single temperature component of the gas, and the individual fits are represented by solid lines. The resulting temperature and column densities obtained from the fits are listed in Table 4.

for foreground extinction, to estimate the internal PDR extinction. Table 1 shows the $A_{V_{\rm bar}}$ and $A_{V_{\rm bar},I}$ values obtained for the five templates using both the foreground and intermingled formalisms. Moreover, in Fig. 11, we present the line cut across the mosaic of $A_{V_{\rm bar}}$. We note that the internal PDR extinction is highest in the DF 1, followed by DF 2, the atomic PDR, and DF 3. In the H II region, the internal PDR extinction is ~ 0. The high value of the internal PDR extinction in DF 1 implies that DF 1 is further along the line of sight than DF 2 and DF 3. Therefore, the column density along the line of sight increases for DF 1, which is more distant from the observer (but closer in projected distance from the ionisation front). The measured flux for the H_2 lines corrected for the foreground and internal PDR extinction in the five templates is presented in Table 3.

The H_2 line ratio of 1–0 S(1)/2–1 S(1) is sensitive to the density. We present a line cut across the mosaic of this ratio in Fig. 11. This ratio exhibits values ranging from ~ 3–5 across the mosaic and begins to increase beyond DF 3. Furthermore, this

ratio has large values in the vicinity of proplyds. To get a quantitative measure of the density, we fitted the H_2 lines corrected for the foreground and internal PDR extinction as well as the H_2 line ratio of 1–0 S(1)/2–1 S(1) observed in the five templates employing the Meudon PDR Code [23]. The Meudon PDR code (Le Petit et al. 2006) can fit the observed line intensities to grids of model PDRs. In this paper, we employ the isochoric model to estimate the gas density. For the isochoric model, which assumes a constant gas density, we first fit all the H_2 line intensities corrected using both the foreground and intermingled formalisms, and then the ratio of 1–0 S(1)/2–1 S(1) obtained with both formalisms, keeping the radiation field and gas density as free parameters. We fix the cloud size expressed as visual extinction A_V to 10 for all the fits. Furthermore, since the H_2 emission in the atomic region and the dissociation fronts belongs to the edge-on PDR, whose brightness at the PDR surface mimics those of an edge-on PDR seen under an inclination ranging from 1–8° (Sect. 6.3.2), we correct the observed fluxes associated with these regions for this geometrical effect. Adopting an inclination angle of 4°, we divide the observed fluxes by a factor of 14 (a geometrical factor in line intensities of $1/\sin(\theta)$ where θ is the inclination angle of the PDR. For $\theta = 4°$, the factor is equal to 14). We highlight that this is a pure geometrical factor that underestimates the real flux. We find that the extinction correction formalism (i.e. foreground or intermingled) does not influence the fit results. The best-fit model, considering all lines, results in a gas density of 3.5×10^4 cm^{-3} in the H II region, $10^3 - 3.5 \times 10^3$ cm^{-3} in the atomic PDR, $10^4 - 3.5 \times 10^4$ cm^{-3} in DF 1 and DF 2, and 10^4 cm^{-3} in DF 3. When considering the line ratio, the best-fit model results in a gas density of $3.5 \times 10^4 - 10^5$ cm^{-3} in the H II region, $10^3 - 3.5 \times 10^3$ cm^{-3} in the atomic PDR, 3.5×10^4 cm^{-3} in DF 1 and DF 2, and 10^4–3.5×10^4 cm^{-3} in DF 3. We remind the reader that the H_2 emission in the H II region originates from the background face-on PDR in OMC-1 (see Fig. 14). Finally, it is worth pointing out that adopting an inclination angle of 8° leads to gas densities from the model fits that are consistently higher by a factor of about 3 compared to an inclination angle of 4°.

We furthermore analyse the H_2 excitation diagrams resulting. Figure 15 presents the excitation diagrams for each template spectrum, where we plot the upper state energy of the transition (E_u/k) versus the normalised column density (N_u/g_u), where N_u is the upper state column density and g_u is the statistical weight of the upper state energy level. We create these excitation diagrams using the H_2 fitting tool in the Photodissociation Region Toolbox (PDRT; Pound & Wolfire 2023)[24]. The tool allows for fitting a one- or two-temperature model and the ortho-to-para ratio (OPR). Here, we analyse the excitation diagrams of $v = 0$ and $v = 1$ vibrational levels for which lines are strong. To get an estimate of the excitation temperature and column density in the five templates, we fitted the excitation diagram of the 0–0 S, 1–0 Q, 1–0 S, 1–0 O, and 1–1 S series independently. We find that using a single temperature and the LTE OPR value of 3 gives the best fit results. We further note that for lines in the $v = 0$ and 1 vibrational series analysed here, the dominant excitation mechanism is radiation – IR radiative cascade of FUV-pumped H_2– rather than collisions. Therefore, the temperatures resulting from these diagrams represent the excitation temperatures rather than the gas temperature. The excitation temperatures and the column densities obtained from fitting the excitation diagrams are presented in Table 4. Lastly, we note that the excitation temperatures obtained from the excitation diagrams in DF 2 and DF 3 are similar to each other but distinct from that in DF 1 implying that the physical properties of DF 2 and DF 3 differ from those of DF 1. A forthcoming paper will analyse the H_2 excitation diagrams based on both the NIRSpec and MIRI IFU PDRs4All observations and thus will include both the collisionally excited levels and FUV pumped levels (Sidhu et al., in prep.).

6.5. CI emission lines

Given the difference between the [C I] 0.985 μm line and the [Fe II] 1.644 μm line delineating the IF and the resemblance between the [C I] 0.985 μm line and the O I 1.317 μm line just beyond the IF, we confirm that the C I originates in the neutral gas beyond the IF. While there is a good resemblance between the [C I] 0.985 μm line and the H_2 emission, enhanced [C I] emission is observed just beyond the IF, similar as for the O I 1.317 μm emission. We find that the ratio of [C I] 0.985/H_2 1–0 S(1) (not corrected for foreground extinction) varies between 0.21 and 2.05 and is <0.9 in the molecular PDR (Fig. 11). This is a much smaller range than observed by Walmsley et al. (2000), who reported ratios between 0.2 and 6, and is likely due to their larger FOV. We also detect C I recombination lines at 1.069 and 1.175 μm (Fig. B.1), which, together with the [C I] 0.983 and 0.985 μm lines, provides an estimate for the electron temperature, T_e, and the gas density, n_H (see Appendix G for details).

First, we can determine whether case A or case B recombination theory applies based on the 1.0696/1.1759[25] line ratio as it is significantly distinct between both cases (Escalante & Victor 1990; Walmsley et al. 2000). However, the observed (extinction corrected) 1.0696/1.1759 line ratios give mixed results (Appendix G). As the observed (extinction corrected) 0.984/1.0969[26] line ratios are consistent with either case A or case B, we estimate the optical depth of a UV resonance line for the high density conditions relevant for the Bar and find it to be optically thick (Appendix G). We thus apply case B recombination theory. The observed extinction corrected 0.984/1.0969 line ratios then results in electron temperatures, T_e, of approximately 2500, 2300, 2900, 6800, and 5600 for, respectively, the H II region, atomic PDR, DF 1, DF 2, and DF 3 templates (Appendix G). Given the uncertainties on the line ratio, the electron temperatures derived for the H II region, the atomic PDR, and DF 1 templates are similar to each other but clearly distinct from those derived for the DF 2 and DF 3 templates (which are also similar to each other within the uncertainties). We note that the emission lines we detect from DF 1 may come from the face-on PDR of the background OMC-1 (Sect. 7). In agreement with the study by Walmsley et al. (2000), the derived electron temperatures are surprisingly high, much higher than temperatures derived from the pure rotational lines of H_2 (~400 K; Allers et al. 2005; Van De Putte et al. 2024) and millimeter-wave carbon recombination lines (mmCRLs; ~500–600 K; Cuadrado et al. 2019).

[23] We note that the Meudon PDR code is part of the interstellar medium database, ISMDB, a web-based fitting tool to fit observations to PDR models. The ISMDB is one of the Science Enabling Products of the PDRS4All ERS programme (Berné et al. 2022), https://pdrs4all.org

[24] The H_2 fitting tool is a Science Enabling Product of the PDRs4All programme, https://pdrs4all.org

[25] The 1.0696 intensity is the sum of the 1.0687 and 1.0696 μm line intensities and the 1.1759 intensity is the sum of the 1.1752 and 1.1758 μm line intensities (Appendix G).

[26] The 0.984 intensity is the sum of the 0.983 and 0.985 μm line intensities (Appendix G).

If all the C I emission results from recombination (see below), these results can be interpret as the carbon NIR recombination lines arising from the hot irradiated surface of small clumps. Unfortunately, as the C I 1.0696 μm line is very weak, we cannot produce a line intensity map of this transition nor a map of the C I electron temperature in order to visually detect clumps. Based on PDR modelling for a typical radiation field, G_0, of 5×10^4 and a wide range of densities (Wolfire et al. 2010, 2022), we conclude that high gas densities ($n \approx 2$–5×10^6 cm^{-3}) are required to reproduce a mean electron temperature, $\langle T_e \rangle = \int T n_e n_{C^+} T^{-0.6} \mathrm{d}z / \int n_e n_{C^+} T^{-0.6} \mathrm{d}z$, of 2000–3000 K, similar to the derived electron temperatures for the H II region, the atomic PDR, and DF 1 templates. However, these model calculations as well as model calculations for a radiation field, G_0, of 1×10^5 and a wide range of densities produce mean electron temperatures, $\langle T_e \rangle$, that are below 4000 K which is significantly lower than those derived for DF 2 and DF 3. The high temperature of the clump reflects the importance of heating by collisional de-excitation of UV pumped H_2 vibrational levels at high densities (Burton et al. 1990). As the dominant cooling transition ([O I] 63 μm) has a critical density of $\sim 3 \times 10^5$ cm^{-3}, cooling cannot keep up with the increased heating and the temperature has to rise to ~5000 K to allow other cooling mechanisms to take over, including through dust radiative cooling and cooling through other (optical) gas lines. Given that the H_2 emission comes from a deeper layer in the PDR with respect to the C I emission, it naturally traces lower temperatures. Moreover, we note that the C I recombination emission is weighted by the carbon emission measure (i.e. proportional to $n^2 L$ with n the gas density and L the depth) and is thus more sensitive to higher density gas whereas the H_2 pure rotational emission is sensitive to the column density, $N = n L$, rather than the density n. The required gas densities to reproduce the C I electron temperature are significantly higher than the gas densities from the NIR H_2 analysis (Sect. 6.4). This suggests then that the H_2 pure rotational lines measure the temperature in the interclump gas and thus do not trace the high density clumps reflecting its sensitivity to the column density, N, rather than the density, n. As the C I emission arises from a very thin layer of a few thousand degree gas, we adopt A_V of 0.5 for this layer (i.e. $N = 1 \times 10^{21}$ cm^{-2}) to derive the gas density, n_H, from the 0.984 μm line intensity (Eq. (G.3)). We obtain densities of 2.1, 5.2, 1.6, 3.5, and 5.3×10^8 cm^{-3} for respectively, the H II region, the atomic PDR, DF 1, DF 2, and DF 3 templates. This is three to four orders of magnitude higher than the gas densities derived from the NIR H_2 analysis (Sect. 6.4). We note that the derived electron temperatures and gas densities for the clumps results in clumps' pressure that much exceeds the pressure of the inter clump medium. Hence, the clumps must be gravitational bound in order to survive or they are transient.

It is clear that the derived C I electron temperatures and densities poses several issues. However, it relies on the assumption that the upper state 2p $^1D_2$ of the 0.982 and 0.985 μm lines is populated solely by radiative recombination and cascade while additional excitation mechanisms would reduce both the derived temperatures and densities. Three other excitation mechanisms are possible. First, ultraviolet absorption and fluorescence via transitions at 1277.245 Å (fluorescence fraction = 0.0106), 1280.135 Å (fluorescence fraction = 0.00695), and 1656.928 Å (fluorescence fraction = 0.000236). Second, direct electron-impact excitation ($e^- + 2p\ ^3P \rightarrow 2p\ ^1D + e^-$; Zatsarinny et al. 2005; Zatsarinny & Bartschat 2013). Third, photodissociation of CO, which occurs via predissociation of far-UV lines (van Dishoeck & Black 1988; Visser et al. 2009; Guan et al. 2021). Combined with recombination, these three excitation mechanisms ensure that the near-IR [C I] lines can be excited not only in the nebula and the ionised carbon zone of the atomic PDR, but also through the neutral carbon layer, and on into the molecular PDR where CO is photodissociated. The relative contribution of these excitation mechanisms and their influence on the C I analysis as described above will be explored in a future paper.

6.6. AIB emission

The components of the 3–4 μm AIB emission in the Bar exhibit variations in intensity, which we discuss in Sect. 6.6.1, and variations in profiles, which we discuss in Sect. 6.6.2. The comparison of the 3–4 μm AIB emission to the mid-IR AIB bands is reported in Chown et al. (2024).

6.6.1. AIB intensity variations

We have performed two spectral decompositions of the AIB emission, which are applied to every pixel of the NIRSpec mosaic. First, we employ an updated version of PAHFIT (Smith et al. 2007; Lai et al. 2020)[27]. In PAHFIT-based models, the AIBs are represented by Drude profiles. Second, we have employed a Gaussian decomposition of the AIB emission in the 3.2–3.7 μm region. The resulting fit for both methods reproduces the observations very well (Fig. 16). In contrast to the PAHFIT method, which uses 7 Drude profiles, the Gaussian decomposition also includes one Gaussian representing the underlying plateau emission and one Gaussian representing the extended red wing of the 3.29 μm AIB. The remaining components are remarkably similar for both decomposition methods. Details on both spectral decompositions are given in Appendix H.1. While neither decomposition method provides a physical decomposition, it allows for a systematic analysis of the AIB emission characteristics. The intensity maps of the AIB components are shown in Fig. 17 and their emission along the cut in Fig. 18.

Most AIBs (all but the 3.40 and 3.42 μm AIBs) mimic the global morphology as seen by the total AIB emission (Fig. 7): a sharp rise at the PDR front, a (broad) plateau in the atomic PDR with a width of about 6.5″ (~1.3×10^{-2} pc), after which a steady decline sets in. This decline levels off towards the south end of the mosaic/cut, reaching brightness levels as observed in the H II region, where the AIB emission originates from the background face-on PDR OMC-1. The latter is in contrast with the 3 μm continuum emission which is much higher in the H II region than in the molecular PDR (see Sect. 5.1). The exceptions to the global AIB morphology are the 3.40 μm AIB and the 3.42 μm AIB (to a slightly lesser extent), which peak in DF 3, instead of the atomic PDR, and show enhanced emission in DF 2 but not in DF 1 compared to the 3.3 μm AIB. The 3.4/3.29 integrated intensity ratio[28] is 0.09–0.11 in the H II region, the atomic PDR and DF 1 templates, whereas values of 0.15 and 0.18 are observed in the DF 2 and DF 3 templates, respectively (for the Gaussian decomposition, Table 1). In addition, while the 3.46 and 3.51 μm AIBs peak in the atomic PDR, these AIBs also show enhanced emission in DF 2 and DF 3, relative to that in the atomic PDR, with respect to the 3.29 μm AIB. Hence, the 3.40, 3.42, 3.56, 3.46, and 3.51 μm AIBs show a less steep increase at the PDR front than the 3.29 μm AIB (of about 4 compared to an increase of about 5 seen in the 3.29 μm AIB emission).

[27] Available at https://github.com/PAHFIT
[28] Calculated by the ratio of the (3.39+3.40+3.42)/(3.29) AIBs.

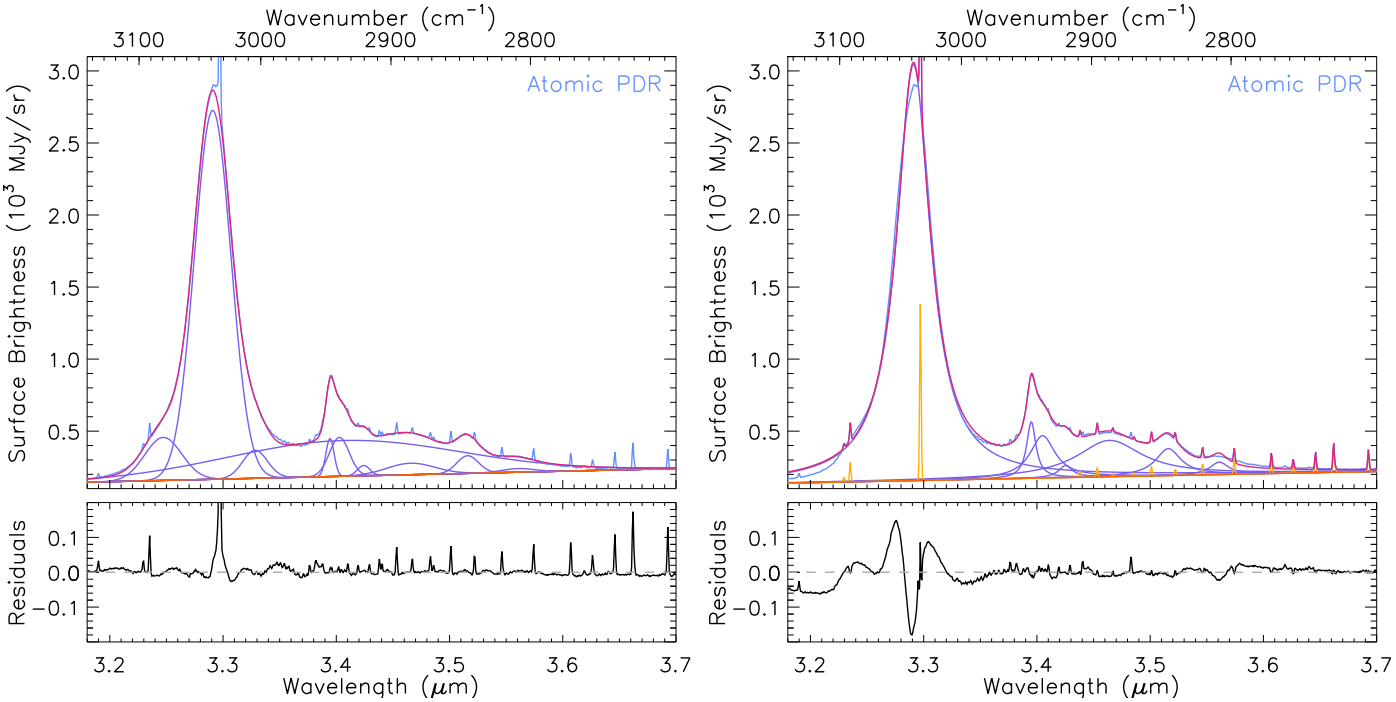

Fig. 16. Spectral decomposition of the AIB emission for the atomic PDR by a Gaussian decomposition (left) and by PAHFIT (right). The dust continuum emission is represented by the orange line, the AIB components by the purple profiles, and emission lines by the yellow Gaussians (for the PAHFIT decomposition; the Gaussian decomposition method removes the lines prior to fitting).

The plateau emission (in the Gaussian decomposition) has a spatial distribution similar to the 3.29 μm AIB, but shows slightly enhanced emission in DF 2 and DF 3 (albeit significantly less than the enhanced emission seen in the 3.40 and 3.42 μm AIBs). Hence, based on its spatial distribution we cannot conclude whether or not the plateau is independent of the superposed features as is observed for the plateaus between 5–10, 10–15, and 15–20 μm (Bregman et al. 1989; Peeters et al. 2012, 2017; Stock & Peeters 2017). Proplyd 203–506 stands out in the AIB maps. Namely, it shows enhanced emission in the 3.40 and 3.42 μm AIBs with respect to the other AIBs, and a 3.3 μm AIB intensity comparable to the lowest seen 3.3 μm AIB intensity in the atomic PDR.

Lastly, we tentatively detect the aromatic CD vibrational mode at 4.35 μm in the atomic PDR and DF 1, and the aliphatic CD vibrational mode at 4.644 μm in potentially all templates (see Sect. 4.1 and Appendix H.2 for details). The aliphatic CD vibrational mode is strongest in the atomic PDR, followed by DF 1, the H II region, DF 2, and is weakest in DF 3 (Table H.2; see Appendix H.2 for details). As the band at 4.35 μm is not well defined (see Sect. 4.1), we refrain from estimating its intensity though we note that it is most easily discerned in the atomic PDR and DF 1 that also exhibit the strongest 4.644 μm band. The ratio of the 4.644 μm band to the total AIB emission in the 3.2–3.7 μm range is 8.2, 6.3, 6.1, 2.8, and 2.4 $\times 10^{-3}$ for the H II region, the atomic PDR, DF 1, DF 2, and DF 3 templates (Table 1) and thus is significantly lower in DF 2 and DF 3 compared to the other templates. A similar pattern is seen in the 4.644/3.29 AIB ratio whereas the 4.644/3.40 AIB ratio is highest in the atomic PDR, closely followed by the H II region, subsequently DF 1 and significantly lower in DF 2 and DF 3 (Table 1). We further note that the excess broadband emission is strongest in the atomic PDR and decreases deeper in the PDR while it is (nearly) absent in the H II region.

6.6.2. Profile variations

Not only do the relative AIB intensities change across the mosaic, so do the AIB band profiles (Fig. 19). The 3.29 μm AIB has a variable width with the full-width-half-maximum (FWHM) ranging from 37.4 cm^{-1} in the atomic PDR to 42.4 cm^{-1} in DF 3 (see Table 1 for FWHM values for all templates). DF 1 shows a band profile similar to that observed in the H II region and the atomic PDR. The extra broadening in DF 2 and DF 3 relative to the other three templates is largely carried by the blue wing. As a consequence, the peak position seems to shift to slightly bluer wavelengths in the DF 2 and DF 3 templates albeit quantifying this shift is hampered by the atomic emission lines (Pfδ, He I recombination lines) superposed on the peak of the AIB. Despite the observed profile variations, all templates exhibit a class A band profile in the classification scheme proposed by van Diedenhoven et al. (2004), and thus showcase profile variability within class A. We note that also the mid-IR AIB band profiles exhibit variations (Chown et al. 2024). Similarly, despite the profile variations, the mid-IR AIBs exhibit a class A band profile except for the 11.2 μm AIB which displays a class A profile in the H II region, the atomic PDR, and DF 1 and a class B profile in DF 2 and DF 3 (Chown et al. 2024).

Profile variations are also detected for the 3.4 μm AIB. This band shows an asymmetric profile with a red wing and consists of three components (at 3.39, 3.40, 3.42 μm, see Table H.1). Comparison of the 3.4 μm AIB profile in the template spectra indicate enhanced emission in the red wing of the 3.40 μm component and thus enhanced broadening of the band in DF 2 and DF 3. Similar to the 3.29 μm AIB profile, DF 1 displays a similar profile to that observed in the H II region and the atomic PDR. Given that numerous H I recombination lines (from the Humphreys series) and H_2 lines are superposed on this AIB,

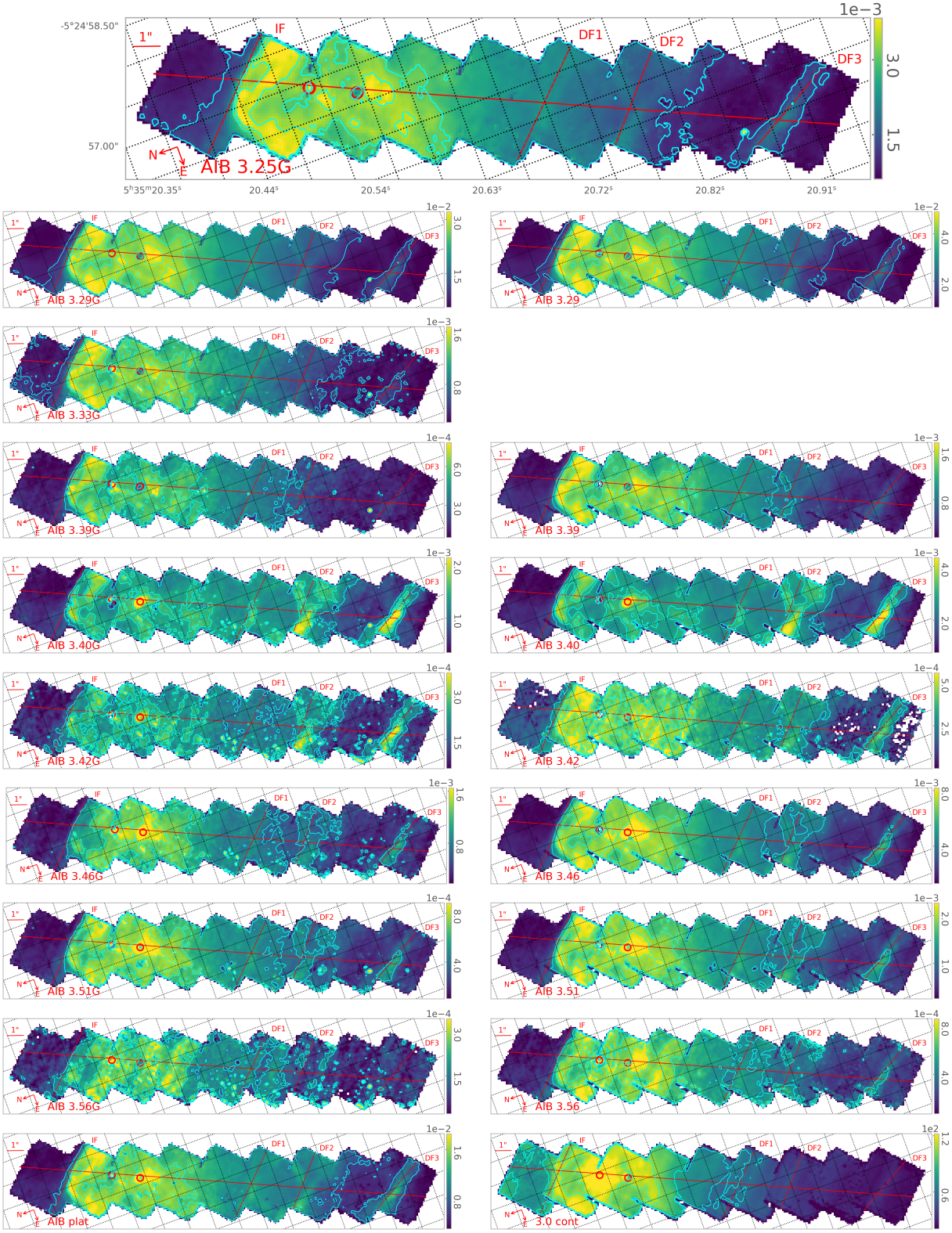

Fig. 17. Spatial distribution of the AIB components in the 3.2–3.7 μm range from the Gaussian decomposition (top and left panels) and PAHFIT decomposition (right panels). 'AIB plat' refers to the plateau emission (bottom panel, left) and '3.0 cont' to the continuum emission at 3.0 μm (bottom panel, right). Units are erg cm^{-2} s^{-1} sr^{-1}, except for the 3.0 μm continuum map, which is in units of MJy sr^{-1}. We set the colour range from the bottom 0.5% to the top 99.5% of data for each map, excluding values of zero, edge pixels, and the two proplyds (as well as the surrounding region of the proplyds for the continuum). White pixels inside the mosaic indicate values of zero reflecting either the component was not used in the fit or issues with the data. The nearly horizontal red line indicates the NIRSpec cut and the nearly vertical red lines indicate from left to right the IF and the DFs (DF 1, DF 2, DF 3). The two proplyds are indicated by the circles. Contours show the 30, 78, 94% of the data for the 3.25G, 3.29/3.29G, and 3.33G components as well as the AIB plat, 50, 78, 93% for the 3.39/3.39G and 3.56/3.56G components, 35, 78, 93% for the 3.40/3.40G and 3.42/3.42G components, 45, 78, 94% for the 3.46/3.46G and 3.51/3.51G components, and 50, 68, 85% for the continuum emission at 3.0 μm. The continuum emission at 3.0 μm from the Gaussian decomposition is shown in Fig. 7.

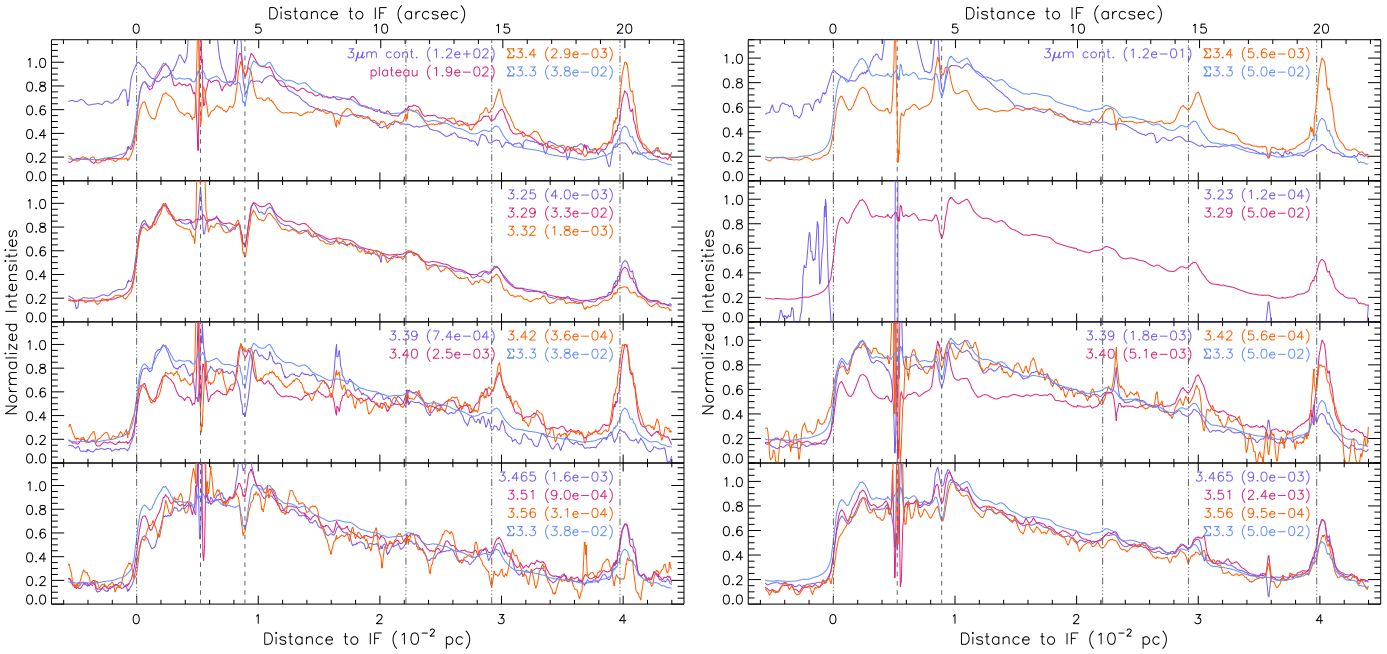

Fig. 18. Normalised AIB and continuum intensities from the Gaussian decomposition (left) and the PAHFIT decomposition (right) as a function of distance to the IF (0.228 pc or 113.4″ from θ^1 Ori C) along a cut crossing the NIRSpec mosaic (see Fig. 1). Normalisation factors are listed between brackets for each intensity. As the cut is not perpendicular to the IF and distances are given along the cut, a correction factor of cos(19.58°)=0.942 needs to be applied to obtain a perpendicular distance from the IF. Σ3.3 reflects the brightness of the 3.25, 3.29, 3.33 μm or 3.23 and 3.29 μm AIBs combined for, respectively, the Gaussian and PAHFIT decomposition. Σ3.4 reflects the brightness of the 3.40, and 3.42 μm AIBs combined. No extinction correction is applied. The dash-dot-dot-dot vertical lines indicate the position of the IF, DF 1, DF 2, and DF 3, respectively, from left to right. The dashed vertical lines indicated the location of the proplyds 203–504 (left) and 203–506 (right). Units are erg cm^{-2} s^{-1} sr^{-1} except for the 3 μm continuum which is in units of MJy sr^{-1}.

a detailed analysis of the 3.4 μm AIB will be performed in a forthcoming paper (Dartois et al., in prep.).

6.6.3. Comparison to previous observations

The spectral inventory of the AIB emission in the 3.2–3.7 μm range is consistent with prior high quality observations of the Orion Bar (Sloan et al. 1997). Likewise, the observed 3.4/3.29 intensity ratios (Table 1) are consistent with earlier reports for the Orion Bar by Geballe et al. (1989) and Sloan et al. (1997). The latter authors also reported a widening (towards the red) of the 3.4 μm AIB into the molecular PDR. To first order, this is consistent with our results but the strength of their 'excess' emission (with respect to the 3.4 μm AIB in the H II region) peaks near 10″ from the IF after which it steadily declines whereas we detect the broadest profile in DF 3 at a distance of 19.8″. In addition, as our observations have unparalleled angular resolution, the radial profiles of the AIB intensities with distance from θ^1 Ori C (Fig. 18) exhibit significant more detail compared to prior observations (Geballe et al. 1989; Sloan et al. 1997).

To our knowledge, the 3.1–4.9 μm broad emission or the 3.8 μm band has not been observed before (Sect. 4.1). In contrast, the bands near 4.4 and 4.6 μm have been detected in the Orion Bar and were attributed to deuterated PAHs (Peeters et al. 2004; Onaka et al. 2014). Following Peeters et al. (2004, i.e. assuming that the integrated absorbance values of the corresponding C-H/C-D modes are similar), we obtain an aliphatic D/H ratio (as probed by 4.64/3.40 bands) of 20.5, 22.5, 15.8, 5.4, and 4.1×10^{-2} in the H II region, the atomic PDR, DF 1, DF 2, and DF 3 templates. This is in contrast to the reported D/H ratio of ∼ 1 reported by these authors. Instead, this derived aliphatic D/H ratio is more in line with the combined aliphatic and aromatic D/H ratio of 0.17 reported by these authors[29]. A quantitative comparison with the results of Onaka et al. (2014) is not possible as these authors applied a different decomposition method[30]. However, these authors reported D/H ratios an order of magnitude lower than those of Peeters et al. (2004). Specifically, they reported an aliphatic D/H ratio (as probed by 4.64/(3.42+3.48) bands) of 0.04 which is of the same order of magnitude as our 4.64/(3.39+3.40+3.42+3.46) ratios using the PAHFIT decomposition (ranging from 0.03 to 0.007, though remember different decomposition methods are used).

6.6.4. Photochemical evolution

The 3 μm region is characteristic for the aromatic and aliphatic C-H stretching mode (e.g. Allamandola et al. 1989). The aromatic CH stretching modes are very susceptible to resonances with combination bands (Maltseva et al. 2015, 2016; Mackie et al. 2015, 2016) and this interaction dominates their profiles (Mackie et al. 2022). Smaller PAHs have more asymmetric profiles, that is, a less steep blue wing and enhanced red wing, reflecting their higher internal energies upon photon absorption (Tielens 2021; Mackie et al. 2022). The observed widening of the asymmetric 3.4 μm band in DF 2 and DF 3 thus may arise

[29] The combined aliphatic and aromatic ratio was probed by the (4.4+4.6)/(3.3+3.4+3.5) using the Gaussian decomposition. Using the nomenclature of this paper, this denominator reflects the sum of all Gaussian components in the 3.2–3.7 μm range except the plateau emission.

[30] These authors used Lorentzian profiles for the 3.29, 3.41, and 3.48 μm bands and did not assume a plateau component.

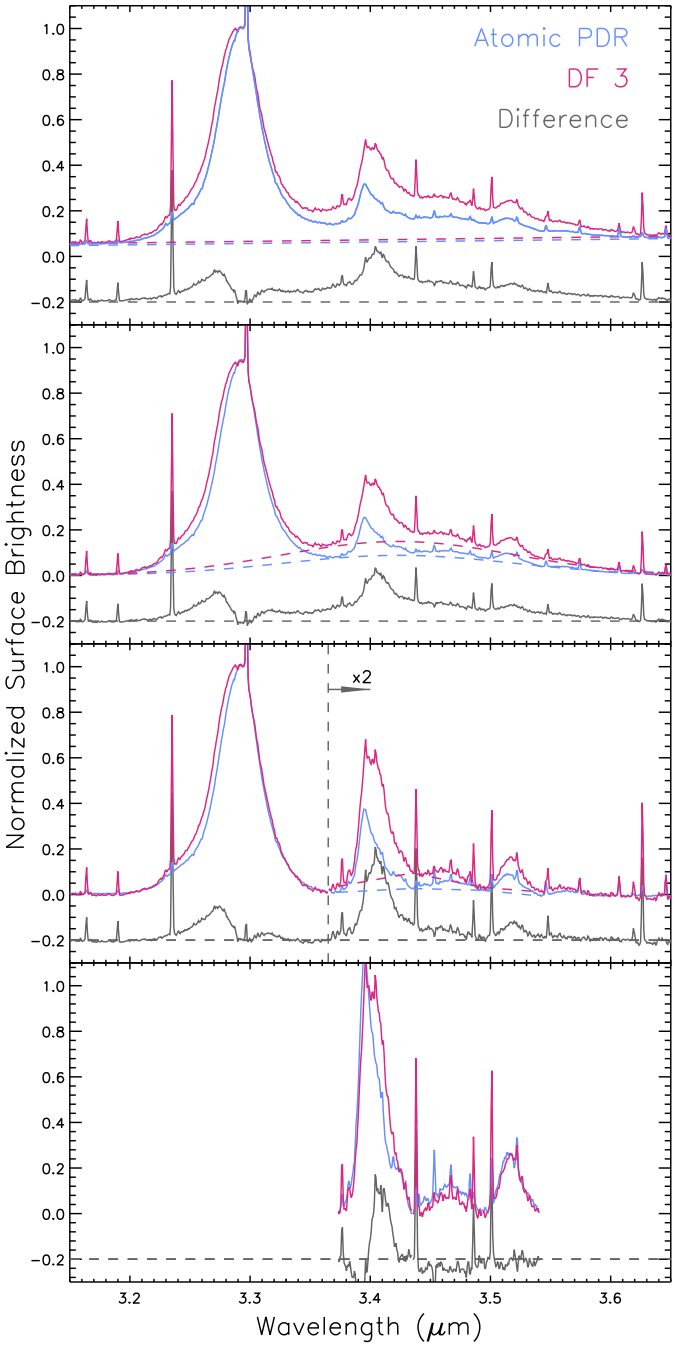

Fig. 19. Comparison of the AIBs in the atomic PDR (blue) and DF 3 (red). The difference in their normalised emission is given in grey and the grey dashed line indicates the zero level for the difference spectrum. Top to bottom: template spectra (solid lines) and their respective linear dust continuum (coloured dashed lines); continuum-subtracted template spectra (solid lines) and their respective plateau emission (coloured dashed lines); (continuum+plateau)-subtracted template spectra (solid lines) and their respective local continua for the weaker AIBs (coloured dashed lines); (continuum+plateau+local continuum)-subtracted template spectra. The template spectra are normalised on the peak intensity of the 3.29 μm AIB in the top three panels, and of the 3.40 μm AIB in the bottom panel.

from an enhanced population of smaller PAHs. The corresponding broadening of the roughly symmetric 3.29 μm band (largely driven by the blue wing) may then arise from the same enhanced population of smaller PAHs. Regions with broader AIB profiles (with respect to the atomic PDR) also show enhanced 3.4/3.29 intensity ratios which traces the aliphatic-to-aromatic ratio (or the degree of aromaticity). The aliphatic-to-aromatic ratio, as traced by the 3.4/3.29 intensity ratio, is known to decrease with increasing intensity of the FUV radiation field (Geballe et al. 1989; Joblin et al. 1996; Sloan et al. 1997; Mori et al. 2014; Pilleri et al. 2015) reflecting that aliphatic bonds are less stable than aromatic ones. Combined with the fact that smaller PAHs are less stable than larger ones, the observations point towards a more fragile population of complex hydrocarbons in DF 2 and DF 3 compared to the complex hydrocarbon population in the H II region (i.e. the background PDR), the atomic PDR, and DF 1. This suggests a UV-driven photochemical evolution of the complex hydrocarbon population that eliminates the more fragile hydrocarbon species near the surface of the PDR which is subjected to a more intense FUV radiation field.

In contrast, the tentative detection of high aliphatic D/H ratios near the surface of the PDR and low ratios deep in the molecular PDR argue against a slow loss of deuterated PAHs as material reaches the surface of the PDR; that is, the presence of PADs in the surface layer of the PDR is not inherited from its past (i.e. from the molecular cloud). Instead, the PAH D enhancement is a local effect that seems to be driven by UV radiation and/or density (as it is strongest in the atomic PDR template). In addition, we note that the aliphatic CD stretch is significantly stronger than the aromatic CD stretch, consistent with prior observations (Peeters et al. 2004; Onaka et al. 2014; Doney et al. 2016) suggesting that the D enhancement is more favourable on aliphatic than aromatic sites. The expected difference in binding energy between hydrogen and deuterium is ~440 cm^{-1} (Allamandola et al. 1989; Wiersma et al. 2020) and, thus, too small to explain the observations. In addition, this energy difference leads to enhanced H scrambling and H loss compared to D while the molecule is exposed to a stronger UV field (Wiersma et al. 2020). Moreover, these authors found that D scrambling favours the migration to a strongly bound aromatic site (instead of an aliphatic site) which could lead to increased aromatic deuteration with respect to aliphatic deuteration. This is in contrast with the observations presented here. It should be noted that the interpretation or possible mechanism to increase aliphatic CD is still speculative and further investigations are warranted. Hence, the PAH D enhancement will be further explored in a forthcoming paper.

7. Discussion

The Bar has served as the template PDR to develop the first PDR models (Tielens & Hollenbach 1985a,b). These theoretical studies predicted a global stratification as a function of depth in the PDR. Tielens et al. (1993) provided the first observational evidence of this stratification and reported an offset between the 3 μm AIB emission, the H_2 1–0 S(1) emission, and the J = 1–0 CO emission. The PDRs4All NIRSpec observations provide a more diverse and detailed picture of the Bar anatomy on spatial scales of 0.075″ – 0.173″. The global stratification (and geometry) as seen with NIRSpec is summarised below, illustrated in Fig. 14, and quantified in Table 2. We note that all distances are quoted along the NIRSpec cut (see Sect. 5.1).

– Closest to θ^1 Ori C, we observe the He-IF at an approximate projected distance of 0.222 pc. The He-IF is resolved and displaced from the H-IF by about 0.4–0.5 × 10^{-2} pc (1.8″–2.5″) in the Huygens region. The NIRSpec mosaic does not cover the peak emission from the He I recombination lines.

– The H-IF is traced by the peak emission of the H I recombination lines (at 113.276″ or d_{proj} = 0.2274 pc from θ^1 Ori C). The sharp decrease towards θ^1 Ori C within the NIRSpec mosaic is likely caused by the gas being accelerated away once it is ionised. The H I recombination line emission decreases away from θ^1 Ori C but does not go to zero due to the foreground H II region (i.e. the H II region in front of the atomic and molecular PDR along the line of sight). As for the He I emission, the NIRSpec mosaic does not cover the peak H I emission within the H II region which, is located about 24″ in front of the H-IF (e.g. Pellegrini et al. 2009).
– The IF is well traced by the [O I] 6300 Å and [Fe II] 1.644 μm emission. We note that this is displaced from the H-IF by 0.1″ or 0.02 × 10^{-2} pc. Enhanced emission of [O I] 6300 Å is also observed in the atomic PDR, which is mostly confined to the region surrounding the proplyds and the filaments. While part of this emission is associated with the proplyds and their jets, the strongest emission is seen in the N-SE filament, which is, to our knowledge, not associated with the proplyds and is parallel to the secondary ridge in the IF. In contrast, the [Fe II] 1.644 μm only shows enhanced emission in the direction of the jet associated with proplyd 203–506. We further note that the N-SE filament is very strong in the O I 1.317 μm emission, but given the lack of enhanced emission in the [Fe II] 1.644 μm line, undulation effects in the surface of the Bar as the prime reason of the observed enhancement in the O I emission can be excluded. Instead, we attribute the enhanced emission to local acceleration zones (Sect. 6.3.1).
– The AIB emission is an excellent tracer of the atomic PDR. The strength of the AIB emission is set by the strength of the FUV radiation field required for the excitation process and the column density of the carriers. The steep increase in its emission (up to 65%) over a very small distance (∼1″) centred at the IF thus indicates the (very sharp) onset of the atomic PDR. Along the NIRSpec cut, the AIB emission remains flat for about 6.5″ or ∼1.3 × 10^{-2} pc, after which it slowly decreases. As the strength of the FUV radiation decreases with depth into the PDR due to dust opacity, the lack of a decrease in AIB emission beyond the onset of the atomic PDR, as well as the small-scale structure observed in the AIB emission, reveals a complexity of the atomic PDR in terms of geometry and small-scale structure that is not captured by 1D PDR models. The AIB emission (primary ridge) peaks at 113.7″ in contrast with earlier studies that reported the AIB emission peaking at 118 and 117″ from θ^1 Ori C (Salgado et al. 2016; Knight et al. 2022). This is attributed to their use of lower angular resolution observations, as well as probing a different location on the Bar. Habart et al. (2024) derived an atomic gas density of 5–10 × 10^4 cm^{-3}. The (maximum) strength of the FUV radiation field impinging on the PDR front can be traced by the fluorescent lines (O I 1.129, 1.317 μm and N I 1.2292 μm) and varies across the PDR front between G_0 = 2.2 to 7.1 × 10^4.
– The transition from the atomic to the molecular PDR is highly structured and displays three dissociation fronts that are parallel to the IF (see also Habart et al. 2024). The rise in the H_2 emission is very sharp (with factors of ∼3, 6, and 10 over a very small distance (0.5″)). These ridges (at a distance of (2.21, 2.92, 3.97) × 10^{-2} pc or 11.03″, 14.55″, 19.80″) represent edge-on portions of the DF, with DF 2 nearly coinciding with the average H_2 emission in the Bar (Habart et al. 2024). Enhanced AIB emission is seen at the three DFs which is lightly displaced from the DFs by (0.02, 0.06, 0.04) × 10^{-2} pc (0.1″, 0.3″, 0.2″), in the direction away from the atomic PDR.

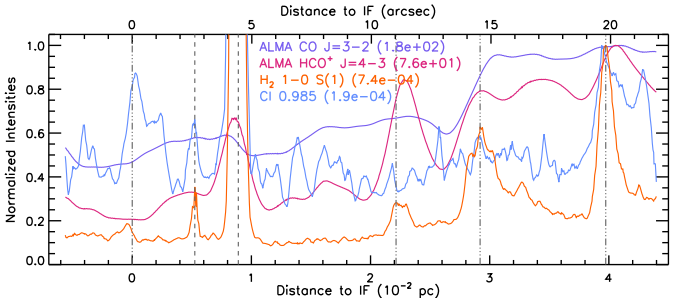

Fig. 20. Comparison of the NIRSpec H_2 1–0 S(1) and C I 0.985 μm observations (in erg cm^{-2} s^{-1} sr^{-1}) with the ALMA observation at 1″ resolution of the HCO^+ J=4–3 line integrated intensity (in K km s^{-1}) and the CO J=3–2 line peak temperatures (T_{peak}, Goicoechea et al. 2016). Shown are normalised line intensities as a function of distance to the IF (0.228 pc or 113.4″ from θ^1 Ori C) along a cut crossing the NIRSpec mosaic (see Fig. 1). As the cut is not perpendicular to the IF and distances are given along the cut, a correction factor of cos(19.58°)=0.942 needs to be applied to obtain a perpendicular distance from the IF. Normalisation factors are listed between brackets for each intensity. No extinction correction is applied. The dash-dot-dot-dot vertical lines indicate the position of the IF, DF 1, DF 2, and DF 3, respectively, from left to right. The dashed vertical lines indicated the location of the proplyds 203–504 (left) and 203–506 (right).

On top of this large-scale morphology/stratification, we observe numerous smaller-scale structures. The typical size of these structures seem to be largest in the ionised gas tracers (a few arcsecs), whereas in the IF, the atomic and molecular PDR structures of sizes of a few 0.1″ are observed. The IF and PDR front is thus highly irregular, non-uniform, and complex. This is also clearly demonstrated in the PDRs4All JWST images (Habart et al. 2024), as well as optical images (e.g. Weilbacher et al. 2015; Henney 2021). As a consequence, all physical parameters, for example, derived in this paper are very precise, but, at the same time, inaccurate due to their dependence on the exact position (on 0.1″ scale) of the intensity of the tracer used to obtain the physical parameter and the incredible small-scale variation observed in these tracers (as well as the assumptions used for the derivation). In addition, assuming the C I emission arises solely from radiative recombination and cascade, the analysis of the C I emission in the template spectra indicates the presence of very high density clumps embedded in a lower-density gas. Based on HCO^+ J=4–3 observations with an angular resolution of ∼1″, Goicoechea et al. (2016) also reported that the gas density near the DF is very inhomogeneous and clumpy with small-scale structure surrounding, and parallel with, the dissociation front (the DF set by these authors corresponds to DF 2). Along the NIRSpec cut, this HCO^+ emission is strongest at DF 3 and displays slightly weaker emission near DF 1 and DF 2, whereas it is considerably weaker towards the H II region and the atomic PDR (Fig. 20).

We further note that DF 1 behaves uniquely compared to DF 2 and DF 3. We summarise:

1. The extinction from the atomic PDR, $A_{V,bar}$, is about 2–4 times higher towards DF 1 than towards DF 2 and DF 3 (Sect. 6.4).
2. While DF 1 is still visible in the AIB emission map, it is indiscernible in the NIRCam F210M filter (Sect. 5.1,

Habart et al. 2024) nor does it exhibit signs of enhanced dust scattered light (Sect. 4.1).
3. DF 2 and DF 3 display a slightly richer molecular inventory, for example, HD v = 1–0 (Sect. 4.1) and the presence of 6.850 and 6.943 μm AIBs (Chown et al. 2024).
4. The characteristics of the AIB emission towards DF 1 are similar to those for the H II region and the atomic PDR, but quite different from those observed in DF 2 and DF 3. Specifically,
   (a) the FWHM of the 3.3 AIB is similar in the H II region, the atomic PDR, and DF 1 (about 38 cm^{-1}), but significantly lower than that of DF 2 and DF 3 (41–43 cm^{-1}, Sect. 6.6). Similar broadening is observed in DF 2 and DF 3 for MIR AIBs (5.25, 6.2, 7.7, 11.2, and 12.7 μm; Chown et al. 2024).
   (b) the aliphatic-to-aromatic ratio, as probed by the 3.4/3.29 AIB, at DF 1 is similar to that of the H II region and the atomic PDR, but 1.5–1.75 times lower than in DF 2 and DF 3 (Sect. 6.6).
   (c) the 11.2 μm AIB displays a class A profile in the H II region, the atomic PDR, and DF 1 and a class B profile in DF 2 and DF 3 (Chown et al. 2024).
   (d) the aliphatic D/H ratio in DF 1 is similar to that in the atomic PDR and about twice that observed in DF 2 and DF 3 (Sect. 6.6).
5. Within the assumptions, the C I emission indicates the presence of clumps. The electron temperature probed in DF 1 is similar to that in the H II region and the atomic PDR whereas it is significantly lower compared to the electron temperature probed in DF 2 and DF 3.
6. The CO J=3–2 emission intensity is considerably lower in DF 1 than in DF 2 and DF 3 (and similar to the atomic PDR and H II region; Fig. 20; Goicoechea et al. 2016).
7. The HCO$^+$ J=4–3 and CO J=3–2 emission velocities at DF 1 have two components, one of which is more consistent with emission from the background molecular cloud, OMC-1, than from the Bar (Goicoechea et al. 2016).

Following Goicoechea et al. (2016), we attribute the small-scale variations to pre-existing, turbulently driven density variations in OMC-1 that were amplified by the passage of the shock driven into this core by the stellar feedback of θ^1 Ori C, perhaps guided by the magnetic field structure that will be enhanced parallel to the shock front. Such small-scale structures can be developed during the passage of the shock due to different types of instabilities (Krasnobaev et al. 2016; Krasnobaev & Tagirova 2017; Riashchikov et al. 2022). It is tempting to speculate that the high density clumps are sites for future star formation, however Goicoechea et al. (2016) concluded that their current mass is not sufficient to make them gravitationally unstable.

Furthermore, based on #1, #2, and #7, Habart et al. (2024) concluded that the DF displays a terraced-field-like structure where the three DFs are portion of the DF observed edge-on and with DF 1 located at a larger distance (from us) compared to DF 2 and DF 3 (see Fig. 14). In addition, based on #6 and #7, Goicoechea et al. (2016) suggested that the CO plumes present between the IF and their DF (i.e. DF 2) could be CO gas flows that are photo-ablated from the molecular PDR into the atomic PDR. The location of DF 1 between the IF and the steep increase seen in the CO J=3–2 emission intensity (#6) thus indicates that the depth in the molecular cloud at DF 1 is smaller than at DF 2 and DF 3 and does not reach the C$^+$/C/CO transition. At the same time, the HCO$^+$ observations indicate that DF 1 (as well as DF 2 and DF 3) is part of the compressed layers (#5, Goicoechea et al. 2016). The distinct AIB properties in DF 1 (similar to those in the H II region and the atomic PDR templates) with respect to those observed in DF 2 and DF 3 then suggests that i) they are characteristic for depths in the PDR shortwards of the C$^+$/C/CO transition, or ii) they are due to an increased (and perhaps dominant) contribution of the atomic PDR to the line of sight emission towards DF 1, or iii) both.

Finally, we note that the Bar is primarily illuminated by θ^1 Ori C. Beyond the Bar, O'Dell et al. (2017) reported that the primary illuminating source is θ^2 Ori A instead. The PDRs4All NIRCam images (Habart et al. 2024, their Fig. 3) suggest that the influence from θ^2 Ori A is limited to its nearby environment in the direction of the Bar because of the high density in that direction (see the enhanced emission in a 'box' surrounding θ^2 Ori A in the F335M (red) and F470N (green) filters). In addition, from a qualitative perspective, our observations do not show any indication of additional or primarily ionisation due to the radiation field of θ^2 Ori A. In fact, the decrease of O I 1.317 μm beyond DF 1 is consistent with a geometrical dilution model centred on θ^1 Ori C (Sect 6.3.1). A similar NIRSpec study of the immediate surrounding of θ^2 Ori A would further clarify the response of the gas to the θ^2 Ori A radiation field. We derived several geometrical distances relevant to obtain a comprehensive 3D picture of the Bar based on the O I 1.317 μm emission (Sect. 6.3.2). As discussed above, these are specific for the NIRSpec mosaic and may change slightly for other positions on the Bar.

8. Conclusions

We present JWST NIRSpec IFU spectral imaging data of the proto-typical PDR in the Orion Nebula, the Bar. Our observations probe the 0.97–5.27 μm at a spectral resolution R of ~2700 and approximately cover 3″ by 25″ at an angular resolution of 0.075″–0.173″. At the distance of the Bar, this is equivalent to 1.5–3.46 × 10^{-4} pc. As such, this unprecedented data set showcases both the large-scale and small-scale structure of the interstellar medium subjected to strong FUV radiation of nearby massive stars. In addition, our mosaic encompasses two proplyds, 203–504 and 203–506, and their associated jets and Herbig-Haro object.

These observations reveal a spectacular richness of spectral lines (~600) and aromatic IR bands on top of weak continuum emission. We detect a forest of atomic and ionic lines as well as numerous H_2 ro-vibrational lines. We furthermore report the detection of:

- H_2 pure rotational lines in the vibrational states v = 0, 1, and 2
- ro-vibrational lines of HD v = 1–0
- ro-vibrational lines of CO v = 1–0, v = 2–1
- ro-vibrational lines of CH$^+$ v = 1–0
- vibrational emission of deuterated aromatic hydrocarbons

Most of these molecular lines are detected for the first time towards a PDR. We provide a line list to facilitate identification of observed lines in future JWST observations. We illustrate the immense diagnostic power provided by the combination of this treasure trove of emission lines and the unprecedented angular resolution through the analysis of the spatial distribution of selected line/band intensities and determine the variations in the physical conditions of the PDR gas and the evolution of complex hydrocarbons.

The observations furthermore reveal the anatomy of the Bar: a large-scale morphology or stratification with distance from θ^1 Ori C and numerous smaller-scale structure, some of which were inaccessible with earlier IR observations. The typical size

of these structures is largest in the ionised gas tracers and smallest for the molecular gas tracers. We highlight in particular:

- the spatially resolved He-IF and the H-IF in the Huygens region for the first time.
- the presence of three dissociation fronts (DFs) which show different characteristics. The increasing internal PDR extinction suggests each of the DFs is located increasingly further from us. Habart et al. (2024) posited that the DF surface is a terrace-field-like structure seen from above in which the 3 DFs are seen as edge-on portions of the DF surface.
- the presence of hot ($T \geq 2000$ K) irradiated surfaces of dense clumps as indicated by the C I emission assuming it solely arises from radiative recombination and cascade.
- the constant density in the atomic PDR.
- the varying aromatic-to-aliphatic ratio and width of the AIBs showcasing the photochemical evolution of the AIB carriers, which is driven by the FUV radiation field.
- the presence of deuterated aromatic hydrocarbons with considerably stronger intensity in the surface layer of the PDR compared to the molecular PDR indicating the D-enhancement is not inherited but rather a local effect.
- enhanced filamentary O I 1.317 μm emission in the jets associated with the two proplyds and in the atomic PDR, which may reflect a local gas acceleration zone.

Our results showcase the complexity of PDRs, and provide very strong constraints on the evolution of the physico-chemical conditions at the critical $H^+/H^0/H_2$ transition and the external boundary conditions of dense molecular condensations. As such, the PDRs4All data set serves as the benchmark to extend PDR models in to the JWST era. The analysis of this data set and the numerous tools developed by the PDRs4All team[31] will assist observers in the analysis of future observations of (unresolved) PDRs, in particular extragalactic objects, while at the same time highlighting the issues encountered when only limited spatial resolution is available.

Acknowledgements. We thank the referee Will Henney for valuable feedback on the manuscript. This work is based on observations made with the NASA/ESA/CSA *James Webb* Space Telescope. The data were obtained from the Mikulski Archive for Space Telescopes at the Space Telescope Science Institute, which is operated by the Association of Universities for Research in Astronomy, Inc., under NASA contract NAS 5-03127 for JWST. These observations are associated with programme #1288 (DOI: 10.17909/pg4c-1737). Support for programme #1288 was provided by NASA through a grant from the Space Telescope Science Institute, which is operated by the Association of Universities for Research in Astronomy, Inc., under NASA contract NAS 5-03127. E.P. and J.C. acknowledge support from the University of Western Ontario, the Institute for Earth and Space Exploration, the Canadian Space Agency (CSA, 22JWGO1-16), and the Natural Sciences and Engineering Research Council of Canada. JRG and SC thank the Spanish MCINN for funding support under grant PID2019-106110GB-I00. C.B. is grateful for an appointment at NASA Ames Research Center through the San José State University Research Foundation (80NSSC22M0107). TO acknowledges support from JSPS Bilateral Program, Grant Number 120219939. MGW acknowledges partial support from JWST Theory grant JWST-AR-01557.001-A. EB, DL, RM, FLP and ER acknowledge support by the Programme National "Physique et Chimie du Milieu Interstellaire" (PCMI) of CNRS/INSU with INC/INP, co-funded by CEA and CNES. Work by YO and MR is carried out within the Collaborative Research Centre 956, sub-project C1, funded by the Deutsche Forschungsgemeinschaft (DFG) – project ID 184018867. I.A. is funded by a fellowship in the Program of Academic Research Projects Management, PRPI-USP. MB acknowledges DST, India for the DST INSPIRE Faculty fellowship. JH acknowledges support from the Chinese Academy of Sciences (CAS), through a grant to the CAS South America Center for Astronomy (CASSACA) in Santiago, Chile. MSK is funded by the Russian Science Foundation, grant 21-12-00373. P.M. acknowledges grants EUR2021-122006, TED2021-129416A-I00 and PID2021-125309OA-I00 funded by MCIN/AEI/ 10.13039/501100011033 and European Union NextGenerationEU/PRTR. NN is funded by the United Arab Emirates University (UAEU) through UAEU Program for Advanced Research (UPAR) grant G00003479. A.P. acknowledges financial assistance from the Banaras Hindu University's IoE grant (R/Dev/D/IoE/Incentive/2021- 22/32439) as well as funding from the SERB, New Delhi through Core Research Grant (CRG/2021/000907) and IUCAA, Pune for associateship. HZ acknowledges support from the Swedish Research Council (contract No 2020-03437).

Data availability: The following data products are provided via the CDS: (1) the five template spectra, (2) the complete version of Table 3 listing the intensities (observed and corrected for extinction using foreground and intermingled formalisms) and column densities of the H_2 lines in $v = 0$ and $v = 1$ states as observed in the five template, and (3) a table with all lines detected in the five template spectra, their identification and their surface brightness (see Appendix B). The following data products are provided via the PDRs4All high-level science products (HLSPs) collection on the Mikulski Archive for Space Telescopes (MAST; `https://mast.stsci.edu/`, DOI: `https://doi.org/10.17909/wqwy-p406`): (1) the NIRSpec cubes, (2) the extraction apertures for the five template spectra and the NIRSpec cut, (3) surface brightness maps of lines and AIBs and maps of physical parameters, (4) surface brightness cuts of lines and AIBs, cuts of physical parameters and the location of the cut, and (5) the reference line list (Sect. 4.2). All links to data products are referenced on the PDRs4All website (`https://pdrs4all.org`).

[31] `https://pdrs4all.org`

References

Abgrall, H., Le Bourlot, J., Pineau Des Forets, G., et al. 1992, A&A, 253, 525
Agúndez, M., Goicoechea, J. R., Cernicharo, J., Faure, A., & Roueff, E. 2010, ApJ, 713, 662
Allamandola, L. J., Tielens, A. G. G. M., & Barker, J. R. 1989, ApJS, 71, 733
Allamandola, L. J., Boersma, C., Lee, T. J., Bregman, J. D., & Temi, P. 2021, ApJ, 917, L35
Allers, K. N., Jaffe, D. T., Lacy, J. H., Draine, B. T., & Richter, M. J. 2005, ApJ, 630, 368
Andree-Labsch, S., Ossenkopf-Okada, V., & Röllig, M. 2017, A&A, 598, A2
Arab, H., Abergel, A., Habart, E., et al. 2012, A&A, 541, A19
Baldwin, J. A., Verner, E. M., Verner, D. A., et al. 2000, ApJS, 129, 229
Bally, J. 2008, in Handbook of Star Forming Regions, Volume I, 4, ed. B. Reipurth, 459
Bally, J., O'Dell, C. R., & McCaughrean, M. J. 2000, AJ, 119, 2919
Bernard-Salas, J., & Tielens, A. G. G. M. 2005, A&A, 431, 523
Bernard-Salas, J., Habart, E., Arab, H., et al. 2012, A&A, 538, A37
Berné, O., Habart, É., Peeters, E., et al. 2022, PASP, 134, 054301
Berné, O., Martin-Drumel, M.-A., Schroetter, I., et al. 2023, Nature, 621, 56
Berné, O., Habart, E., Peeters, E., et al. 2024, Science, 383, 988
Bertoldi, F., & Draine, B. T. 1996, ApJ, 458, 222
Black, J. H., & Dalgarno, A. 1976, ApJ, 203, 132
Blagrave, K. P. M., Martin, P. G., Rubin, R. H., et al. 2007, ApJ, 655, 299
Boersma, C., Rubin, R. H., & Allamandola, L. J. 2012, ApJ, 753, 168
Böker, T., Arribas, S., Lützgendorf, N., et al. 2022, A&A, 661, A82
Boogert, A. C. A., Gerakines, P. A., & Whittet, D. C. B. 2015, ARA&A, 53, 541
Bregman, J. D., Allamandola, L. J., Tielens, A. G. G. M., Geballe, T. R., & Witteborn, F. C. 1989, ApJ, 344, 791
Brieva, A. C., Gredel, R., Jäger, C., Huisken, F., & Henning, T. 2016, ApJ, 826, 122
Brooke, J. S. A., Bernath, P. F., Western, C. M., et al. 2016, J. Quant. Spec. Radiat. Transf., 168, 142
Buragohain, M., Pathak, A., Sarre, P., Onaka, T., & Sakon, I. 2015, MNRAS, 454, 193
Burton, M. G., Hollenbach, D. J., & Tielens, A. G. G. M. 1990, ApJ, 365, 620
Cardelli, J. A., Clayton, G. C., & Mathis, J. S. 1989, ApJ, 345, 245
Champion, J., Berné, O., Vicente, S., et al. 2017, A&A, 604, A69
Changala, P. B., Neufeld, D. A., & Godard, B. 2021, ApJ, 917, 16
Chown, R., Sidhu, A., Peeters, E., et al. 2024, A&A, 685, A75
Code, A. D. 1973, in Interstellar Dust and Related Topics, 52, eds. J. M. Greenberg, & H. C. van de Hulst, 505
Cuadrado, S., Goicoechea, J. R., Pilleri, P., et al. 2015, A&A, 575, A82
Cuadrado, S., Goicoechea, J. R., Cernicharo, J., et al. 2017, A&A, 603, A124
Cuadrado, S., Salas, P., Goicoechea, J. R., et al. 2019, A&A, 625, A3
Del Zanna, G., & Storey, P. J. 2022, MNRAS, 513, 1198
Doney, K. D., Candian, A., Mori, T., Onaka, T., & Tielens, A. G. G. M. 2016, A&A, 586, A65
Draine, B. T. 2011, Physics of the Interstellar and Intergalactic Medium (Princeton University Press)
Egorov, O. V., Lozinskaya, T. A., Moiseev, A. V., & Smirnov-Pinchukov, G. V. 2014, MNRAS, 444, 376
Egorov, O. V., Lozinskaya, T. A., Moiseev, A. V., & Shchekinov, Y. A. 2017, MNRAS, 464, 1833
Elliott, K. H., & Meaburn, J. 1974, Ap&SS, 28, 351

Elmegreen, B. G., & Lada, C. J. 1977, ApJ, 214, 725
Escalante, V., & Victor, G. A. 1990, ApJS, 73, 513
Esteban, C., Vilchez, J. M., & Smith, L. J. 1994, AJ, 107, 1041
Esteban, C., Peimbert, M., Torres-Peimbert, S., & Escalante, V. 1998, MNRAS, 295, 401
Ferland, G. J., Chatzikos, M., Guzmán, F., et al. 2017, Rev. Mex. Astron. Astrofis., 53, 385
Fuente, A., Rodriguez-Franco, A., Garcia-Burillo, S., Martin-Pintado, J., & Black, J. H. 2003, A&A, 406, 899
Gardner, J. P., Mather, J. C., Clampin, M., et al. 2006, Space Sci. Rev., 123, 485
Geballe, T. R., Tielens, A. G. G. M., Allamandola, L. J., Moorhouse, A., & Brand, P. W. J. L. 1989, ApJ, 341, 278
Genzel, R., & Stutzki, J. 1989, ARA&A, 27, 41
Gerin, M., Neufeld, D. A., & Goicoechea, J. R. 2016, ARA&A, 54, 181
Giard, M., Bernard, J. P., Lacombe, F., Normand, P., & Rouan, D. 1994, A&A, 291, 239
Gibb, E. L., Whittet, D. C. B., Boogert, A. C. A., & Tielens, A. G. G. M. 2004, ApJS, 151, 35
Godard, B., & Cernicharo, J. 2013, A&A, 550, A8
Goicoechea, J. R., & Roncero, O. 2022, A&A, 664, A190
Goicoechea, J. R., Teyssier, D., Etxaluze, M., et al. 2015, ApJ, 812, 75
Goicoechea, J. R., Pety, J., Cuadrado, S., et al. 2016, Nature, 537, 207
Goicoechea, J. R., Cuadrado, S., Pety, J., et al. 2017, A&A, 601, A9
Gordon, I. E., Rothman, L. S., Hargreaves, R. J., et al. 2022, J. Quant. Spec. Radiat. Transf., 277, 107949
Gordon, K. D., Clayton, G. C., Decleir, M., et al. 2023, ApJ, 950, 86
Gorti, U., & Hollenbach, D. 2002, ApJ, 573, 215
Großschedl, J. E., Alves, J., Meingast, S., et al. 2018, A&A, 619, A106
Guan, L., Jiang, P., Zhang, G., et al. 2021, A&A, 647, A127
Güdel, M., Briggs, K. R., Montmerle, T., et al. 2008, Science, 319, 309
Habart, E., Dartois, E., Abergel, A., et al. 2010, A&A, 518, A116
Habart, E., Le Gal, R., Alvarez, C., et al. 2023, A&A, 673, A149
Habart, E., Peeters, E., Berné, O., et al. 2024, A&A, 685, A73
Henney, W. J. 2021, MNRAS, 502, 4597
Henney, W. J., Williams, R. J. R., Ferland, G. J., Shaw, G., & O'Dell, C. R. 2007, ApJ, 671, L137
Herrmann, F., Madden, S. C., Nikola, T., et al. 1997, ApJ, 481, 343
Hillenbrand, L. A., & Carpenter, J. M. 2000, ApJ, 540, 236
Hogerheijde, M. R., Jansen, D. J., & van Dishoeck, E. F. 1995, A&A, 294, 792
Hopkins, P. F., Quataert, E., & Murray, N. 2012, MNRAS, 421, 3522
Hudgins, D. M., Bauschlicher, C. W., J., & Sandford, S. A. 2004, ApJ, 614, 770
Hummer, D. G., & Storey, P. J. 1987, MNRAS, 224, 801
Jakobsen, P., Ferruit, P., Alves de Oliveira, C., et al. 2022, A&A, 661, A80
Jansen, D. J., Spaans, M., Hogerheijde, M. R., & Van Dishoeck, E. F. 1995, A&A, 303, 541
Joblin, C., Tielens, A. G. G. M., Allamandola, L. J., & Geballe, T. R. 1996, ApJ, 458, 610
Joblin, C., Bron, E., Pinto, C., et al. 2018, A&A, 615, A129
Kaplan, K. F., Dinerstein, H. L., Oh, H., et al. 2017, ApJ, 838, 152
Kaplan, K. F., Dinerstein, H. L., Kim, H., & Jaffe, D. T. 2021, ApJ, 919, 27
Kim, C.-G., Ostriker, E. C., & Kim, W.-T. 2013, ApJ, 776, 1
Kirsanova, M. S., Sobolev, A. M., Thomasson, M., et al. 2008, MNRAS, 388, 729
Knight, C., Peeters, E., Stock, D. J., Vacca, W. D., & Tielens, A. G. G. M. 2021, ApJ, 918, 8
Knight, C., Peeters, E., Tielens, A. G. G. M., & Vacca, W. D. 2022, MNRAS, 509, 3523
Koenig, X. P., Allen, L. E., Gutermuth, R. A., et al. 2008, ApJ, 688, 1142
Kounkel, M., Covey, K., Suárez, G., et al. 2018, AJ, 156, 84
Kraemer, K. E., Engelke, C. W., Renger, B. A., & Sloan, G. C. 2022, AJ, 164, 161
Krasnobaev, K. V., & Tagirova, R. R. 2017, MNRAS, 469, 1403
Krasnobaev, K. V., Tagirova, R. R., Arafailov, S. I., & Kotova, G. Y. 2016, Astron. Lett., 42, 460
Lai, T. S. Y., Smith, J. D. T., Baba, S., Spoon, H. W. W., & Imanishi, M. 2020, ApJ, 905, 55
Le Bourlot, J., Pineau Des Forets, G., Roueff, E., & Flower, D. R. 1993, A&A, 267, 233
Le Petit, F., Nehmé, C., Le Bourlot, J., & Roueff, E. 2006, ApJS, 164, 506
Leurini, S., Rolffs, R., Thorwirth, S., et al. 2006, A&A, 454, L47
Lis, D. C., & Schilke, P. 2003, ApJ, 597, L145
Luhman, K. L., Engelbracht, C. W., & Luhman, M. L. 1998, ApJ, 499, 799
Luhman, M. L., Jaffe, D. T., Keller, L. D., & Pak, S. 1994, ApJ, 436, L185
Mackie, C. J., Candian, A., Huang, X., et al. 2015, J. Chem. Phys., 143, 224314
Mackie, C. J., Candian, A., Huang, X., et al. 2016, J. Chem. Phys., 145, 084313
Mackie, C. J., Candian, A., Lee, T. J., & Tielens, A. G. G. M. 2022, J. Phys. Chem. A, 126, 3198
Maltseva, E., Petrignani, A., Candian, A., et al. 2015, ApJ, 814, 23
Maltseva, E., Petrignani, A., Candian, A., et al. 2016, ApJ, 831, 58
Marconi, A., Testi, L., Natta, A., & Walmsley, C. M. 1998, A&A, 330, 696
Martín-Hernández, N. L., Bik, A., Kaper, L., Tielens, A. G. G. M., & Hanson, M. M. 2003, A&A, 405, 175
McLeod, A. F., Dale, J. E., Ginsburg, A., et al. 2015, MNRAS, 450, 1057
Méndez-Delgado, J. E., Henney, W. J., Esteban, C., et al. 2021, ApJ, 918, 27
Menten, K. M., Reid, M. J., Forbrich, J., & Brunthaler, A. 2007, A&A, 474, 515
Mori, T. I., Onaka, T., Sakon, I., et al. 2014, ApJ, 784, 53
Nagy, Z., Van der Tak, F. F. S., Ossenkopf, V., et al. 2013, A&A, 550, A96
Neufeld, D. A., Godard, B., Bryan Changala, P., et al. 2021, ApJ, 917, 15
O'Dell, C. R. 2001, ARA&A, 39, 99
O'Dell, C. R., Kollatschny, W., & Ferland, G. J. 2017, ApJ, 837, 151
O'Dell, C. R., Abel, N. P., & Ferland, G. J. 2020, ApJ, 891, 46
Ojha, D. K., Samal, M. R., Pandey, A. K., et al. 2011, ApJ, 738, 156
Onaka, T., Mori, T. I., Sakon, I., et al. 2014, ApJ, 780, 114
Onaka, T., Sakon, I., & Shimonishi, T. 2022, ApJ, 941, 190
Ossenkopf, V., Röllig, M., Neufeld, D. A., et al. 2013, A&A, 550, A57
Osterbrock, D. E., Tran, H. D., & Veilleux, S. 1992, ApJ, 389, 305
Pabst, C., Higgins, R., Goicoechea, J. R., et al. 2019, Nature, 565, 618
Pabst, C. H. M., Goicoechea, J. R., Teyssier, D., et al. 2020, A&A, 639, A2
Parikka, A., Habart, E., Bernard-Salas, J., Köhler, M., & Abergel, A. 2018, A&A, 617, A77
Parmar, P. S., Lacy, J. H., & Achtermann, J. M. 1991, ApJ, 372, L25
Peeters, E., Allamandola, L. J., Bauschlicher, C. W., J., et al. 2004, ApJ, 604, 252
Peeters, E., Tielens, A. G. G. M., Allamandola, L. J., & Wolfire, M. G. 2012, ApJ, 747, 44
Peeters, E., Bauschlicher, Jr., C. W., Allamandola, L. J., et al. 2017, ApJ, 836, 198
Pellegrini, E. W., Baldwin, J. A., Ferland, G. J., Shaw, G., & Heathcote, S. 2009, ApJ, 693, 285
Pilleri, P., Montillaud, J., Berné, O., & Joblin, C. 2012, A&A, 542, A69
Pilleri, P., Joblin, C., Boulanger, F., & Onaka, T. 2015, A&A, 577, A16
Pound, M. W., & Wolfire, M. G. 2023, AJ, 165, 25
Preibisch, T. & Zinnecker, H. 1999, AJ, 117, 2381
Prozesky, A., & Smits, D. P. 2018, MNRAS, 478, 2766
Reiter, M., McLeod, A. F., Klaassen, P. D., et al. 2019, MNRAS, 490, 2056
Riashchikov, D. S., Pomelnikov, I. A., & Molevich, N. E. 2022, Bull. Lebedev Phys. Inst., 49, 307
Röllig, M., Abel, N. P., Bell, T., et al. 2007, A&A, 467, 187
Roueff, E., Abgrall, H., Czachorowski, P., et al. 2019, A&A, 630, A58
Rubin, R. H., Simpson, J. P., O'Dell, C. R., et al. 2011, MNRAS, 1526
Salas, P., Oonk, J. B. R., Emig, K. L., et al. 2019, A&A, 626, A70
Salgado, F., Berné, O., Adams, J. D., et al. 2016, ApJ, 830, 118
Schirmer, T., Ysard, N., Habart, E., et al. 2022, A&A, 666, A49
Sellgren, K. 1984, ApJ, 277, 623
Sellgren, K., Tokunaga, A. T., & Nakada, Y. 1990, ApJ, 349, 120
Shaw, G., Ferland, G. J., Henney, W. J., et al. 2009, ApJ, 701, 677
Sheffer, Y., Wolfire, M. G., Hollenbach, D. J., Kaufman, M. J., & Cordier, M. 2011, ApJ, 741, 45
Simon, R., Stutzki, J., Sternberg, A., & Winnewisser, G. 1997, A&A, 327, L9
Sloan, G. C., Bregman, J. D., Geballe, T. R., Allamandola, L. J., & Woodward, E. 1997, ApJ, 474, 735
Smith, J. D. T., Draine, B. T., Dale, D. A., et al. 2007, ApJ, 656, 770
Smits, D. P. 1996, MNRAS, 278, 683
Sota, A., Maíz Apellániz, J., Walborn, N. R., et al. 2011, ApJS, 193, 24
Stacey, G. J., Jaffe, D. T., Geis, N., et al. 1993, ApJ, 404, 219
Sternberg, A., & Dalgarno, A. 1989, ApJ, 338, 197
Sternberg, A., & Dalgarno, A. 1995, ApJS, 99, 565
Stock, D. J., & Peeters, E. 2017, ApJ, 837, 129
Stoerzer, H., Stutzki, J., & Sternberg, A. 1995, A&A, 296, L9
Störzer, H., & Hollenbach, D. 1998, ApJ, 495, 853
Tabone, B., van Hemert, M. C., van Dishoeck, E. F., & Black, J. H. 2021, A&A, 650, A192
Tauber, J. A., Tielens, A. G. G. M., Meixner, M., & Goldsmith, P. F. 1994, ApJ, 422, 136
Tauber, J. A., Lis, D. C., Keene, J., Schilke, P., & Buettgenbach, T. H. 1995, A&A, 297, 567
Tielens, A. 2005, The Physics and Chemistry of the Interstellar Medium (Springer Netherlands)
Tielens, A. G. 2021, Molecular Astrophysics (Cambridge University Press)
Tielens, A. G. G. M., & Hollenbach, D. 1985a, ApJ, 291, 722
Tielens, A. G. G. M., & Hollenbach, D. 1985b, ApJ, 291, 747
Tielens, A. G. G. M., Meixner, M. M., van der Werf, P. P., et al. 1993, Science, 262, 86
Van De Putte, D., Meshaka, R., Trahin, B., et al. 2024, A&A, accepted [arXiv:2404.03111]

van der Tak, F. F. S., Nagy, Z., Ossenkopf, V., et al. 2013, A&A, 560, A95
van der Werf, P. P., Stutzki, J., Sternberg, A., & Krabbe, A. 1996, A&A, 313, 633
van der Werf, P. P., Goss, W. M., & O'Dell, C. R. 2013, ApJ, 762, 101
van der Wiel, M. H. D., van der Tak, F. F. S., Ossenkopf, V., et al. 2009, A&A, 498, 161
van Diedenhoven, B., Peeters, E., Van Kerckhoven, C., et al. 2004, ApJ, 611, 928
van Dishoeck, E. F., & Black, J. H. 1988, ApJ, 334, 771
van Hoof, P. A. M. 2018, Galaxies, 6, 63
Vicente, S., Berné, O., Tielens, A., et al. 2013, ApJ, 765, L38
Visser, R., van Dishoeck, E. F., & Black, J. H. 2009, A&A, 503, 323
Walmsley, C. M., Natta, A., Oliva, E., & Testi, L. 2000, A&A, 364, 301
Weilbacher, P. M., Monreal-Ibero, A., Kollatschny, W., et al. 2015, A&A, 582, A114
Wen, Z., & O'dell, C. 1995, ApJ, 438, 784
Wiersma, S. D., Candian, A., Bakker, J. M., et al. 2020, A&A, 635, A9
Williams, J. P., & McKee, C. F. 1997, ApJ, 476, 166
Wolfire, M. G., McKee, C. F., Hollenbach, D., & Tielens, A. G. G. M. 2003, ApJ, 587, 278
Wolfire, M. G., Hollenbach, D., & McKee, C. F. 2010, ApJ, 716, 1191
Wolfire, M. G., Vallini, L., & Chevance, M. 2022, ARA&A, 60, 247
Wyrowski, F., Schilke, P., Hofner, P., & Walmsley, C. M. 1997, ApJ, 487, L171
Yang, X. J., Li, A., & Glaser, R. 2020, ApJS, 251, 12
Yang, X. J., Li, A., He, C. Y., & Glaser, R. 2021, ApJS, 255, 23
Young Owl, R. C., Meixner, M. M., Wolfire, M., Tielens, A. G. G. M., & Tauber, J. 2000, ApJ, 540, 886
Yousefi, M., Bernath, P. F., Hodges, J., & Masseron, T. 2018, J. Quant. Spec. Radiat. Transf., 217, 416
Zannese, M., Tabone, B., Habart, E., et al. 2023, A&A, 671, A41
Zannese, M., Tabone, B., Habart, E., et al. 2024, Nat. Astron., in press https://doi.org/10.1038/s41550-024-02203-0
Zatsarinny, O., & Bartschat, K. 2013, J. Phys. B At. Mol. Phys., 46, 112001
Zatsarinny, O., Bartschat, K., Bandurina, L., & Gedeon, V. 2005, Phys. Rev. A, 71, 042702

[1] Department of Physics & Astronomy, The University of Western Ontario, London ON N6A 3K7, Canada
e-mail: pis@pdrs4all.org
[2] Institute for Earth and Space Exploration, The University of Western Ontario, London ON N6A 3K7, Canada
[3] Carl Sagan Center, SETI Institute, 339 Bernardo Avenue, Suite 200, Mountain View, CA 94043, USA
[4] Institut d'Astrophysique Spatiale, Université Paris-Saclay, CNRS, Bâtiment 121, 91405 Orsay Cedex, France
[5] Institut de Recherche en Astrophysique et Planétologie, Université Toulouse III – Paul Sabatier, CNRS, CNES, 9 Av. du colonel Roche, 31028 Toulouse Cedex 04, France
[6] Space Telescope Science Institute, 3700 San Martin Drive, Baltimore, MD 21218, USA
[7] Department of Astronomy, University of Michigan, 1085 South University Avenue, Ann Arbor, MI 48109, USA
[8] Leiden Observatory, Leiden University, PO Box 9513, 2300 RA Leiden, The Netherlands
[9] Astronomy Department, University of Maryland, College Park, MD 20742, USA
[10] Institut des Sciences Moléculaires d'Orsay, Université Paris-Saclay, CNRS, Bâtiment 520, 91405 Orsay Cedex, France
[11] Instituto de Física Fundamental (CSIC), Calle Serrano 121-123, 28006, Madrid, Spain
[12] NASA Ames Research Center, MS 245-6, Moffett Field, CA 94035-1000, USA
[13] Department of Astronomy, Graduate School of Science, The University of Tokyo, 7-3-1 Bunkyo-ku, Tokyo 113-0033, Japan
[14] Department of Physics, Faculty of Science and Engineering, Meisei University, 2-1-1 Hodokubo, Hino, Tokyo 191-8506, Japan
[15] Instituto de Astrofísica e Ciências do Espaço, Tapada da Ajuda, Edifício Leste, 2° Piso, 1349-018 Lisboa, Portugal
[16] ACRI-ST, Centre d'Etudes et de Recherche de Grasse (CERGA), 10 Av. Nicolas Copernic, 06130 Grasse, France
[17] INCLASS Common Laboratory, 10 Av. Nicolas Copernic, 06130 Grasse, France
[18] LERMA, Observatoire de Paris, PSL Research University, CNRS, Sorbonne Universités, 92190 Meudon, France
[19] UK Astronomy Technology Centre, Royal Observatory Edinburgh, Blackford Hill EH9 3HJ, UK
[20] Observatorio Astronómico Nacional (OAN,IGN), Alfonso XII, 3, 28014 Madrid, Spain
[21] Sterrenkundig Observatorium, Universiteit Gent, Gent, Belgium
[22] Quantum Solid State Physics (QSP), Celestijnenlaan 200d – Box 2414, 3001 Leuven, Belgium
[23] Institut de Planétologie et d'Astrophysique de Grenoble (IPAG), Université Grenoble Alpes, CNRS, 38000 Grenoble, France
[24] Institut de Radioastronomie Millimétrique (IRAM), 300 Rue de la Piscine, 38406 Saint-Martin d'Hères, France
[25] I. Physikalisches Institut der Universität zu Köln, Zülpicher Straße 77, 50937 Köln, Germany
[26] Johns Hopkins University, 3400 N. Charles Street, Baltimore, MD, 21218, USA
[27] Physikalischer Verein – Gesellschaft für Bildung und Wissenschaft, Robert-Mayer-Str. 2, 60325 Frankfurt, Germany
[28] Goethe-Universität, Physikalisches Institut, Frankfurt am Main, Germany
[29] Department of Space, Earth and Environment, Chalmers University of Technology, Onsala Space Observatory, 439 92 Onsala, Sweden
[30] Instituto de Física e Química, Universidade Federal de Itajubá, Av. BPS 1303, Pinheirinho, 37500-903, Itajubá, MG, Brazil
[31] Institute of Mathematics and Statistics, University of São Paulo, Rua do Matão, 1010, Cidade Universitária, Butantã, 05508-090 São Paulo, SP, Brazil
[32] Instituto de Física e Química, Universidade Federal de Itajubá, Av. BPS 1303, Pinheirinho, 37500-903 Itajubá, MG, Brazil
[33] Bay Area Environmental Research Institute, Moffett Field, CA 94035, USA
[34] Australian Synchrotron, Australian Nuclear Science and Technology Organisation (ANSTO), Victoria, Australia
[35] INAF – Osservatorio Astrofisico di Catania, Via Santa Sofia 78, 95123 Catania, Italy
[36] Laboratoire de Physique de l'École Normale Supérieure, ENS, Université PSL, CNRS, Sorbonne Université, Université de Paris, 75005 Paris, France
[37] Laboratory for Atmospheric and Space Physics, University of Colorado, Boulder, CO 80303, USA
[38] Department of Chemistry, University of Colorado, Boulder, CO 80309, USA
[39] Institute for Modeling Plasma, Atmospheres, and Cosmic Dust (IMPACT), University of Colorado, Boulder, CO 80303, USA
[40] Faculty of Aerospace Engineering, Delft University of Technology, Kluyverweg 1, 2629 HS Delft, The Netherlands
[41] Radboud University, Institute for Molecules and Materials, FELIX Laboratory, Toernooiveld 7, 6525 ED Nijmegen, The Netherlands
[42] School of Physics, University of Hyderabad, Hyderabad, Telangana 500046, India
[43] Department of Physics, Wellesley College, 106 Central Street, Wellesley, MA 02481, USA
[44] Anton Pannekoek Institute for Astronomy, University of Amsterdam, The Netherlands
[45] Delft University of Technology, Delft, The Netherlands
[46] Laboratoire de Physique des deux infinis Irène Joliot-Curie, Université Paris-Saclay, CNRS/IN2P3, Bâtiment 104, 91405 Orsay Cedex, France
[47] Department of Chemistry, GITAM school of Science, GITAM Deemed to be University, Bangalore, India
[48] Institut de Physique de Rennes, UMR CNRS 6251, Université de Rennes 1, Campus de Beaulieu, 35042 Rennes Cedex, France
[49] Department of Chemistry, The University of British Columbia, Vancouver, British Columbia, Canada
[50] National Radio Astronomy Observatory (NRAO), 520 Edgemont Road, Charlottesville, VA 22903, USA
[51] European Space Astronomy Centre (ESAC/ESA), Villanueva de la Cañada, 28692 Madrid, Spain
[52] Observatoire de Paris, PSL University, Sorbonne Université, LERMA, CNRS, 75014, Paris, France

[53] Harvard-Smithsonian Center for Astrophysics, 60 Garden Street, Cambridge, MA 02138, USA
[54] Sorbonne Université, CNRS, UMR 7095, Institut d'Astrophysique de Paris, 98bis bd Arago, 75014 Paris, France
[55] Institut Universitaire de France, Ministère de l'Enseignement Supérieur et de la Recherche, 1 rue Descartes, 75231 Paris Cedex 05, France
[56] Department of Physics and Astronomy, Rice University, Houston, TX 77005-1892, USA
[57] Yunnan Observatories, Chinese Academy of Sciences, 396 Yangfangwang, Guandu District, Kunming, 650216, PR China
[58] Chinese Academy of Sciences South America Center for Astronomy, National Astronomical Observatories, CAS, Beijing 100101, PR China
[59] Departments of Chemistry and Astronomy, University of Virginia, Charlottesville, VA 22904, USA
[60] InterCat and Dept. Physics and Astron., Aarhus University, Ny Munkegade 120, 8000 Aarhus C, Denmark
[61] Laboratory Astrophysics Group of the Max Planck Institute for Astronomy at the Friedrich Schiller University Jena, Institute of Solid State Physics, Helmholtzweg 3, 07743 Jena, Germany
[62] Instituto de Astronomia, Geofísica e Ciências Atmosféricas, Universidade de São Paulo, 05509-090 São Paulo, SP, Brazil
[63] Department of Physics and Astronomy, San José State University, San Jose, CA 95192, USA
[64] European Space Agency, Space Telescope Science Institute, 3700 San Martin Drive, Baltimore, MD 21218, USA
[65] Institute of Astronomy, Russian Academy of Sciences, 119017, Pyatnitskaya str., 48 , Moscow, Russia
[66] Department of Earth, Ocean, & Atmospheric Sciences, University of British Columbia, British Columbia V6T 1Z4, Canada
[67] Telespazio UK for ESA, ESAC, 28692 Villanueva de la Cañada, Madrid, Spain
[68] IPAC, California Institute of Technology, Pasadena, CA, USA
[69] LAB, Université de Bordeaux, CNRS, B18N, 33615 Pessac, France
[70] Department of Physics and Astronomy, University of Missouri, Columbia, MO 65211, USA
[71] Max Planck Institute for Astronomy, Königstuhl 17, 69117 Heidelberg, Germany
[72] Chemical Sciences Division, Lawrence Berkeley National Laboratory, Berkeley, CA, USA
[73] Kenneth S. Pitzer Center for Theoretical Chemistry, Department of Chemistry, University of California – Berkeley, Berkeley, CA, USA
[74] AIM, CEA, CNRS, Université Paris-Saclay, Université Paris Diderot, Sorbonne Paris Cité, 91191 Gif-sur-Yvette, France
[75] Institut des Sciences Moléculaires, CNRS, Université de Bordeaux, 33405 Talence, France
[76] Department of Chemistry, Massachusetts Institute of Technology, Cambridge, MA 02139, USA
[77] Instituto de Ciencia de Materiales de Madrid (CSIC), Sor Juana Ines de la Cruz 3, 28049 Madrid, Spain
[78] Department of Physics, PO Box 64, 00014 University of Helsinki, Finland
[79] Steward Observatory, University of Arizona, Tucson, AZ 85721-0065, USA
[80] AstronetX PBC, 55 Post Rd W FL 2, Westport, CT 06880, USA
[81] Department of Physics, College of Science, United Arab Emirates University (UAEU), Al-Ain 15551, UAE
[82] National Astronomical Observatory of Japan, National Institutes of Natural Science, 2-21-1 Osawa, Mitaka, Tokyo 181-8588, Japan
[83] Department of Physics, Institute of Science, Banaras Hindu University, Varanasi 221005, India
[84] University of Central Florida, Orlando, FL 32765, USA
[85] Van't Hoff Institute for Molecular Sciences, University of Amsterdam, PO Box 94157, 1090 GD Amsterdam, The Netherlands
[86] Laboratoire de Chimie et Physique Quantiques LCPQ/IRSAMC, UMR5626, Université de Toulouse (UPS) and CNRS, Toulouse, France
[87] Instituto de Matemática, Estatística e Física, Universidade Federal do Rio Grande, 96201-900 Rio Grande, RS, Brazil
[88] Center for Astrophysics and Space Sciences, Department of Physics, University of California, San Diego, 9500 Gilman Drive, La Jolla, CA 92093, USA
[89] School of Chemistry, The University of Nottingham, University Park, Nottingham NG7 2RD, UK
[90] Astronomy Department, Ohio State University, Columbus, OH 43210, USA
[91] Space Science Institute, 4765 Walnut St., R203, Boulder, CO 80301, USA
[92] Department of Physics, Stockholm University, 10691 Stockholm, Sweden
[93] Department of Physics, Texas State University, San Marcos, TX 78666, USA
[94] Ritter Astrophysical Research Center, University of Toledo, Toledo, OH 43606, USA
[95] School of Physics and Astronomy, Sun Yat-sen University, 2 Da Xue Road, Tangjia, Zhuhai 519000, Guangdong Province, PR China
[96] Star and Planet Formation Laboratory, 0–0 S(RIKEN Cluster for Pioneering Research, Hirosawa 2-1, Wako, Saitama 351-0198, Japan
[97] Institute of Deep Space Sciences, Deep Space Exploration Laboratory, Hefei 230026, PR China
[98] Departamento de Astronomía, Universidad de Chile, Las Condes, 7591245 Santiago, Chile
[99] INAF – Osservatorio Astronomico di Cagliari, via della Scienza 5, 09047 Selargius (CA), Italy

Appendix A: Data reduction

We list our estimate of the cross-calibration factor between NIRCam and NIRSpec in Table A.1 and details about the extraction apertures employed for the five template spectra in Table A.2. The cut employed in the paper connects coordinates (5:35:20.0785, -5:24:57.885) and (5:35:21.0801, -5:25:31.157) (α, δ (ICRS, J2000))[32].

Table A.1. NIRSpec/NIRCam cross-calibration measurements.

Filter	a [(1)]	b [(1)] MJy sr^{-1}
(1)	(2)	(3)
g235h-f170lp		
F187N	0.994±0.001	−19.115±1.150
F210M	0.897±0.003	5.252±0.292
F212N	0.804±0.007	13.579±0.474
Average	0.9797±0.0011	6.3578±0.2432
g395h-f290lp		
F335M	0.8709±0.0009	4.6709±0.4649
F405N	0.9213±0.0038	1.8698±2.6086
Average	0.8992±0.0005	3.0398±0.1748

Notes. [(1)]Cross-calibration is parameterised by $I_\nu^{\rm NIRCam} = aI_\nu^{\rm NIRSpec} + b$. We multiply the F100LP and F170LP cubes by the average value of a for F170LP, and we multiply the F290LP cubes by the average value of a for that grating/filter combination. We do not use b in our analysis.

Table A.2. Extraction apertures used in this paper[33].

Template	Center		Size	PA	Projected distance of centre to θ^1 Ori C	
	α (J2000)	δ (J2000)	$''\times''$	°	pc	$''$
H II region	5:35:20.1545	-5:24:59.646	1.26×2.5	43.738	0.224	111.4
atomic PDR	5:35:20.2307	-5:25:02.555	1.7×2.5	43.738	0.230	114.5
DF 1	5:35:20.5105	-5:25:11.931	1.0×1.6	50.000	0.250	124.7
DF 2	5:35:20.6135	-5:25:14.691	1.0×1.6	38.000	0.257	127.8
DF 3	5:35:20.7095	-5:25:20.351	1.0×2.654	38.000	0.268	133.5

[32] See acknowledgments for data availability.
[33] See acknowledgments for data availability.

Appendix B: Template spectra

The spectral inventory of the five template spectra is shown in Fig. B.1. Line intensities are given in Table B.1, only available in electronic form at the CDS. Column 1 lists the line identification, Column 2 the wavelength in vacuum (μm), Columns 3-17 the wavelength of the peak position of the Gaussian fit, the integrated line intensities and their fit uncertainties in the five templates (in units of erg $cm^{-2}s^{-1}sr^{-1}$). An intensity cutoff of 1×10^{-6} erg cm^{-2} s^{-1} sr^{-1} is applied. We did *not* apply a 3-sigma detection cutoff.

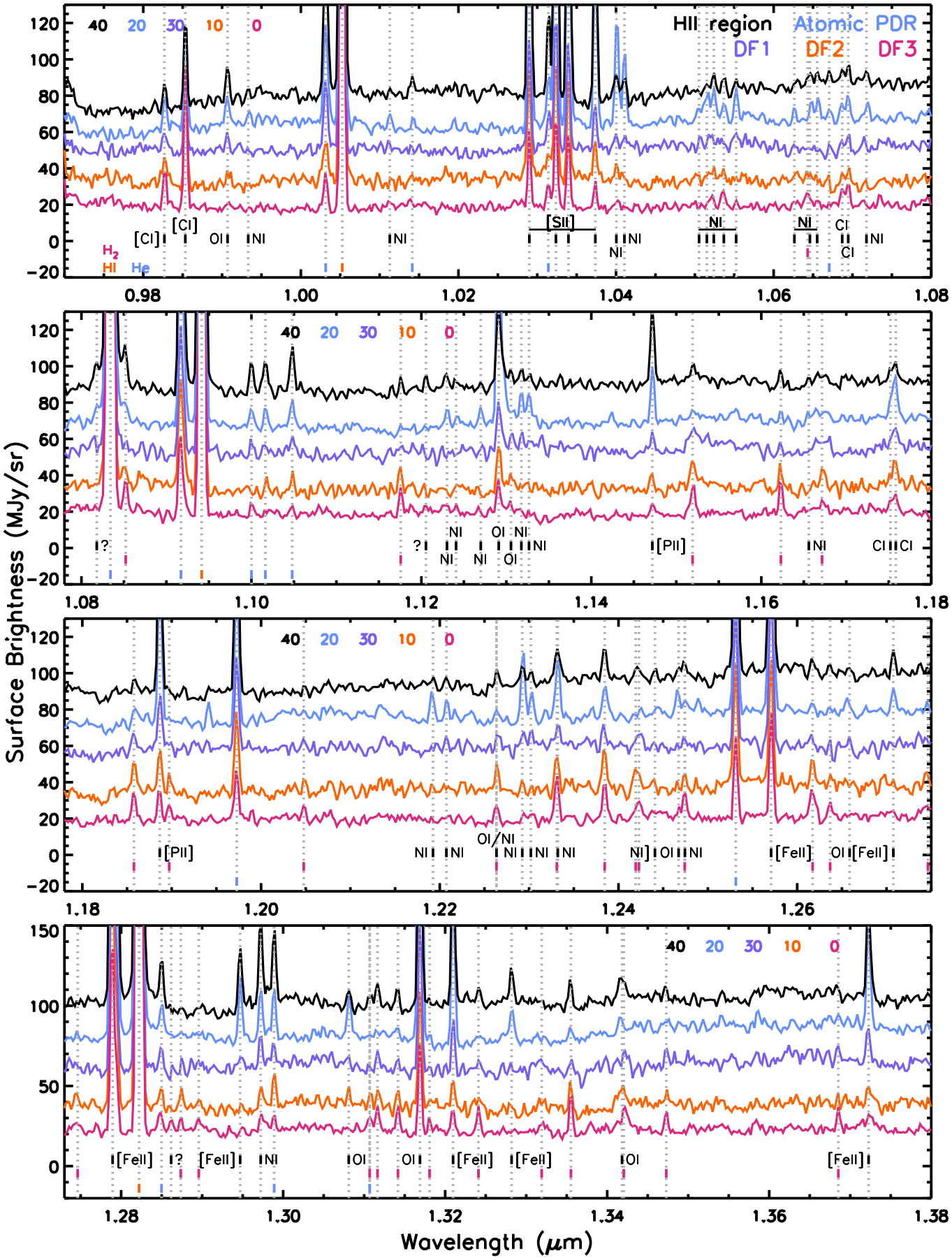

Fig. B.1. Spectral inventory of the five template spectra. Spectra are offset by the numbers given at the top of the panel. Areas susceptible to the wavelength gap are shown in light grey. The colour coding is labelled in the top panel.

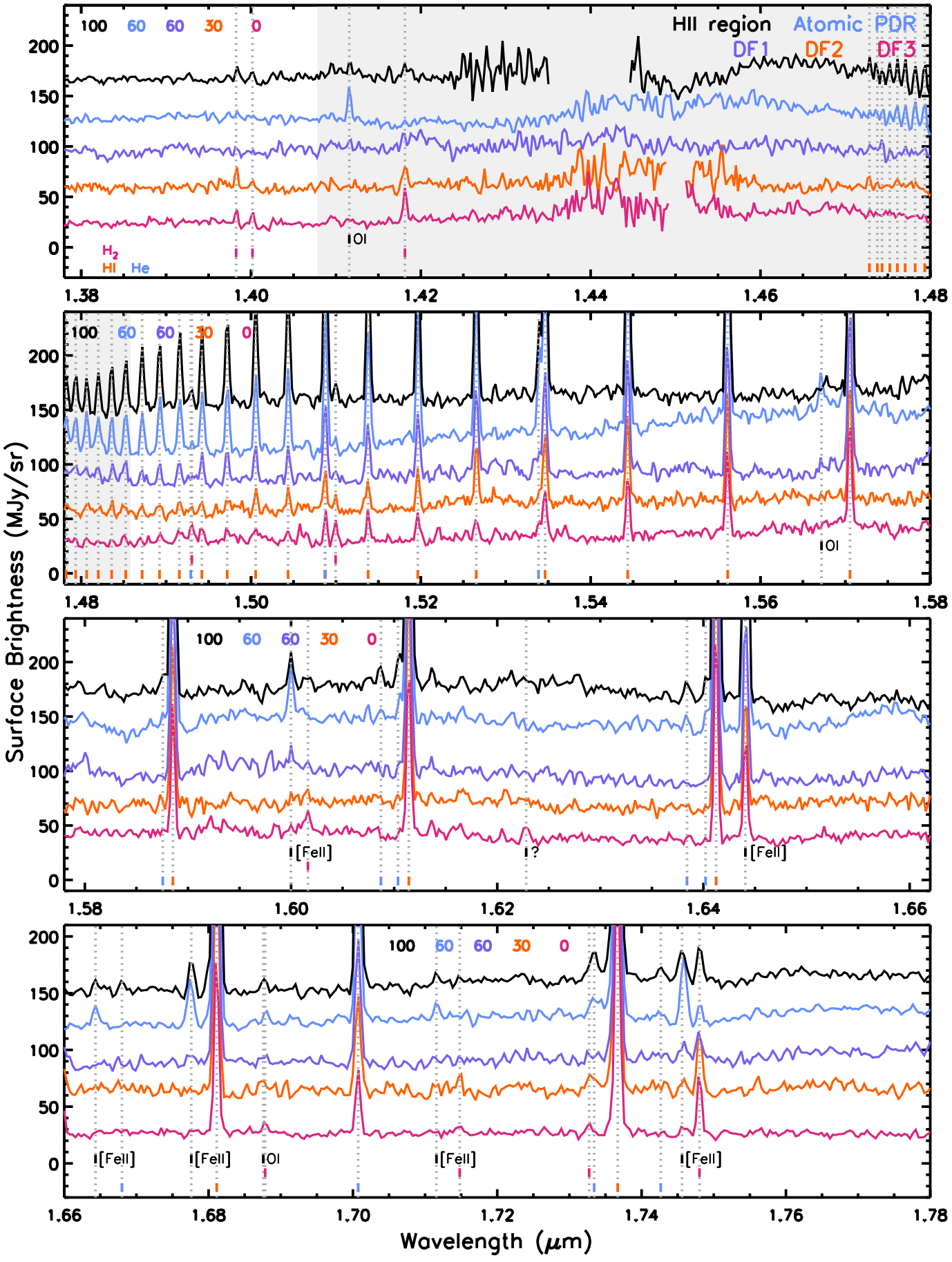

Fig. B.1. continued.

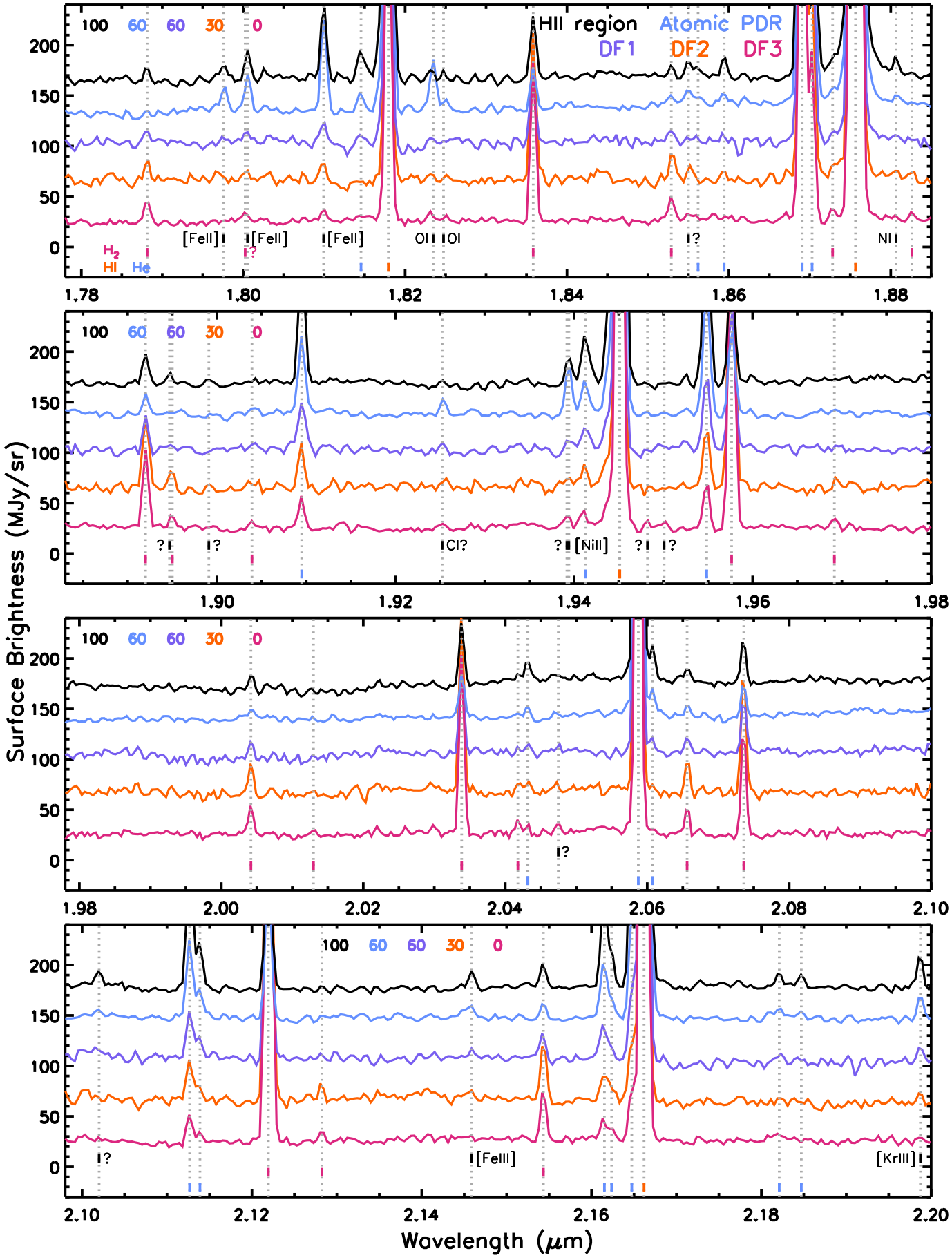

Fig. B.1. continued.

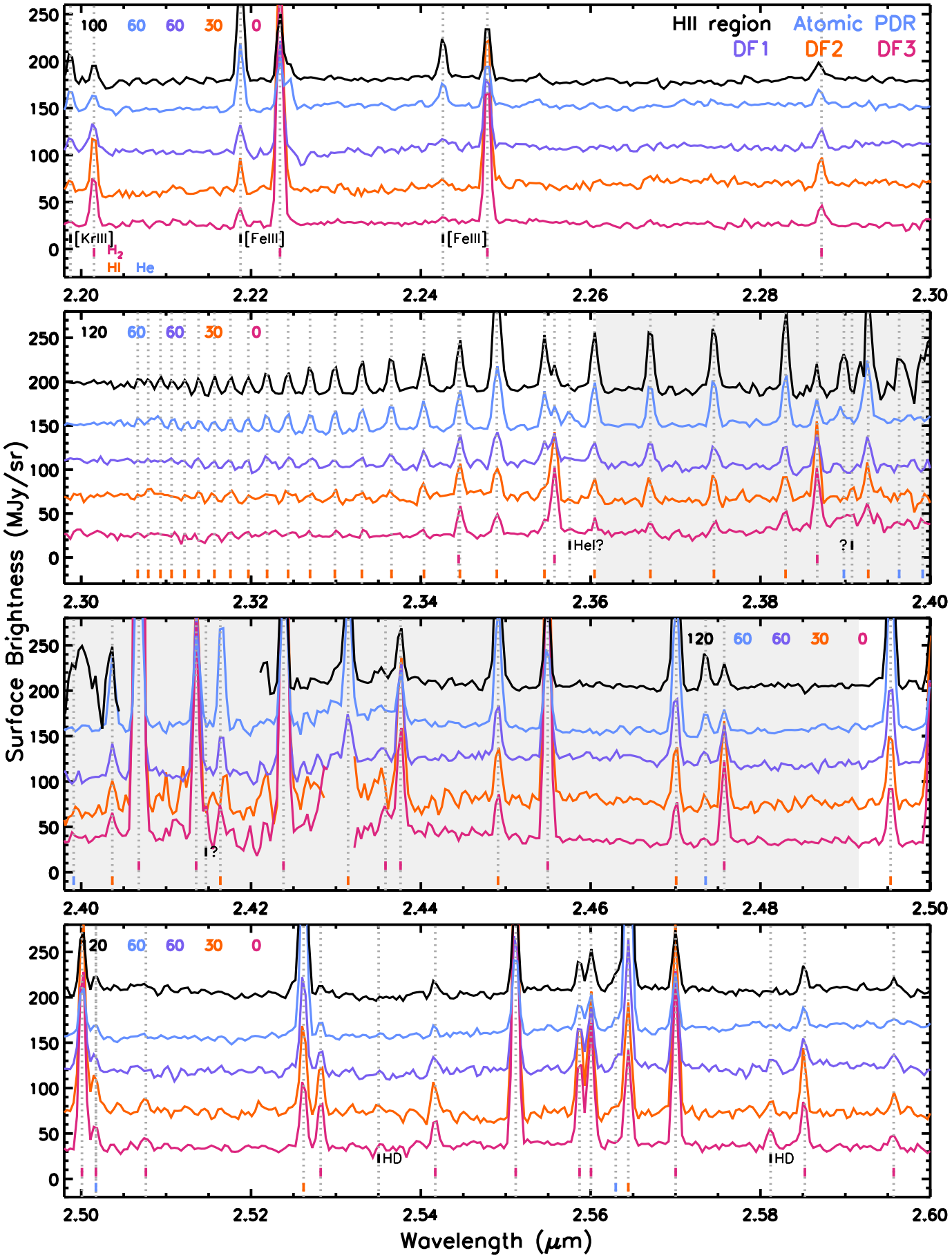

Fig. B.1. continued.

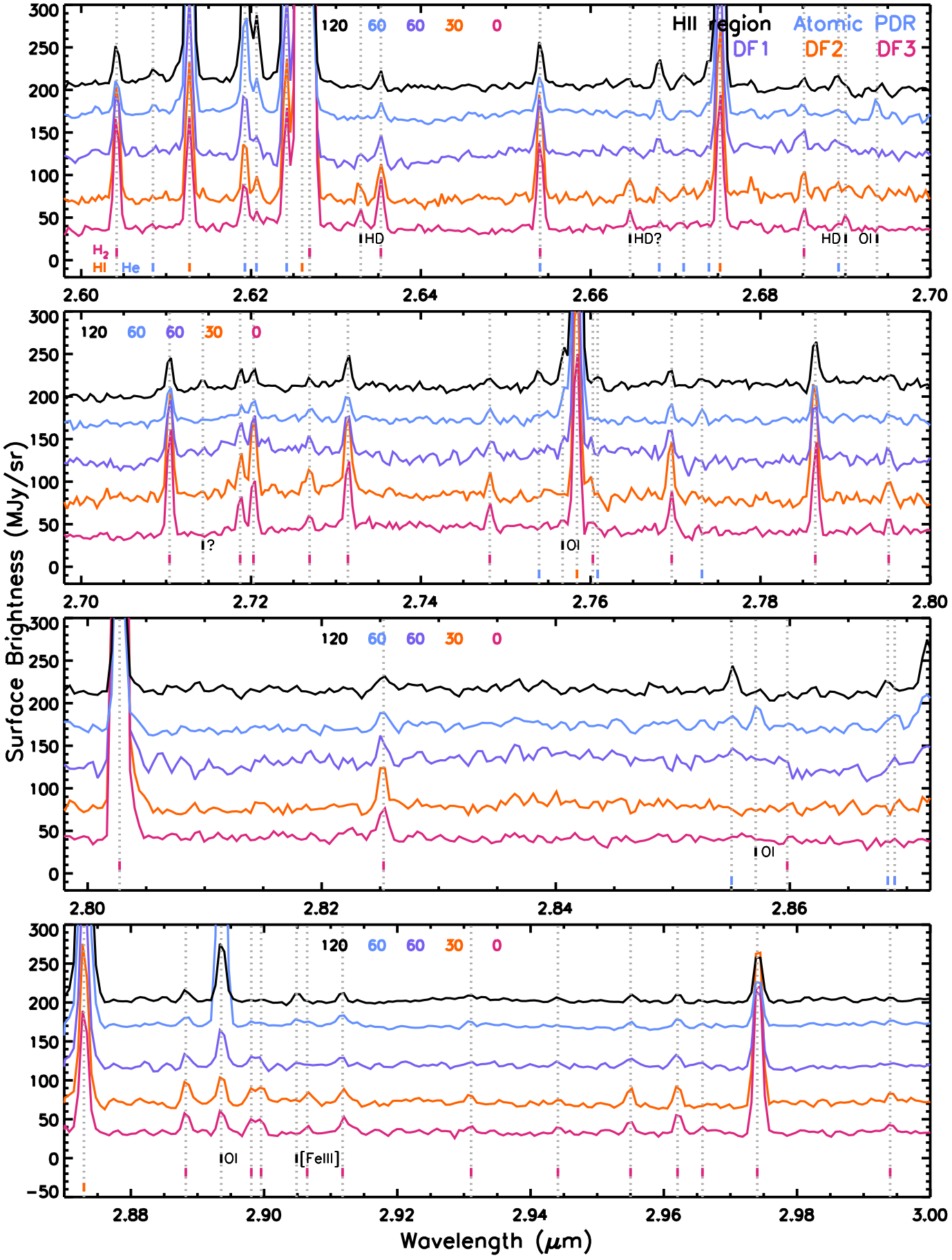

Fig. B.1. continued.

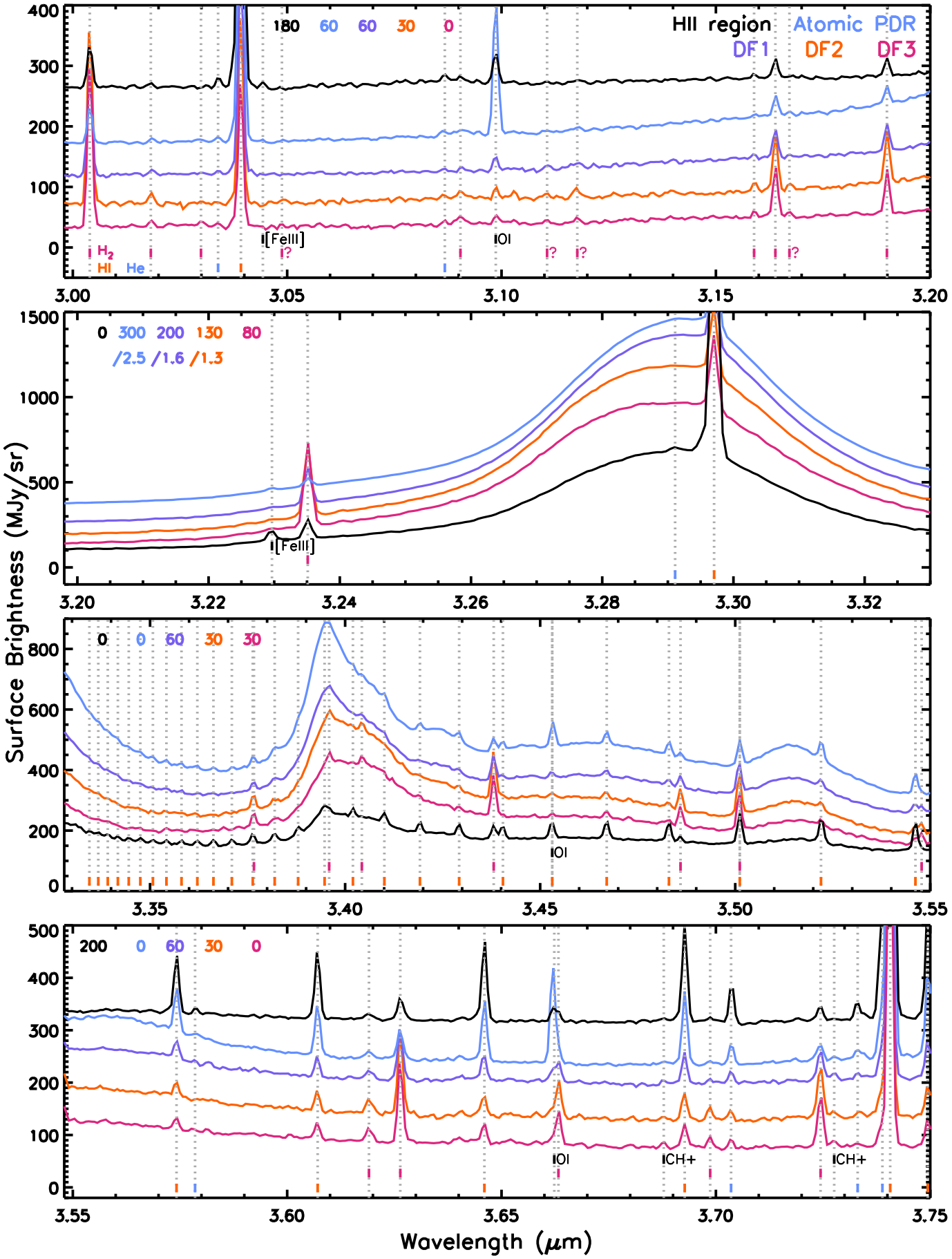

Fig. B.1. continued.

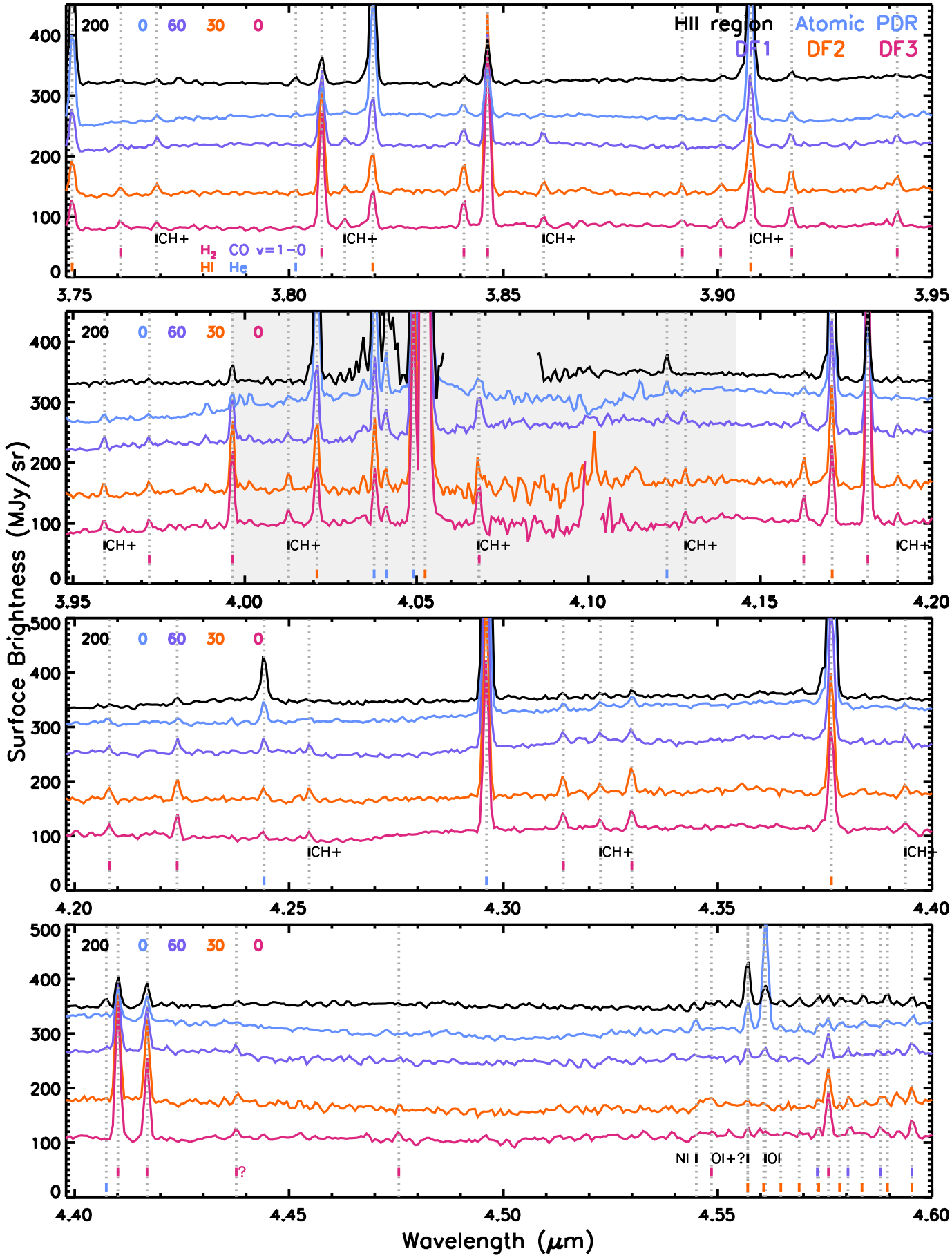

Fig. B.1. continued.

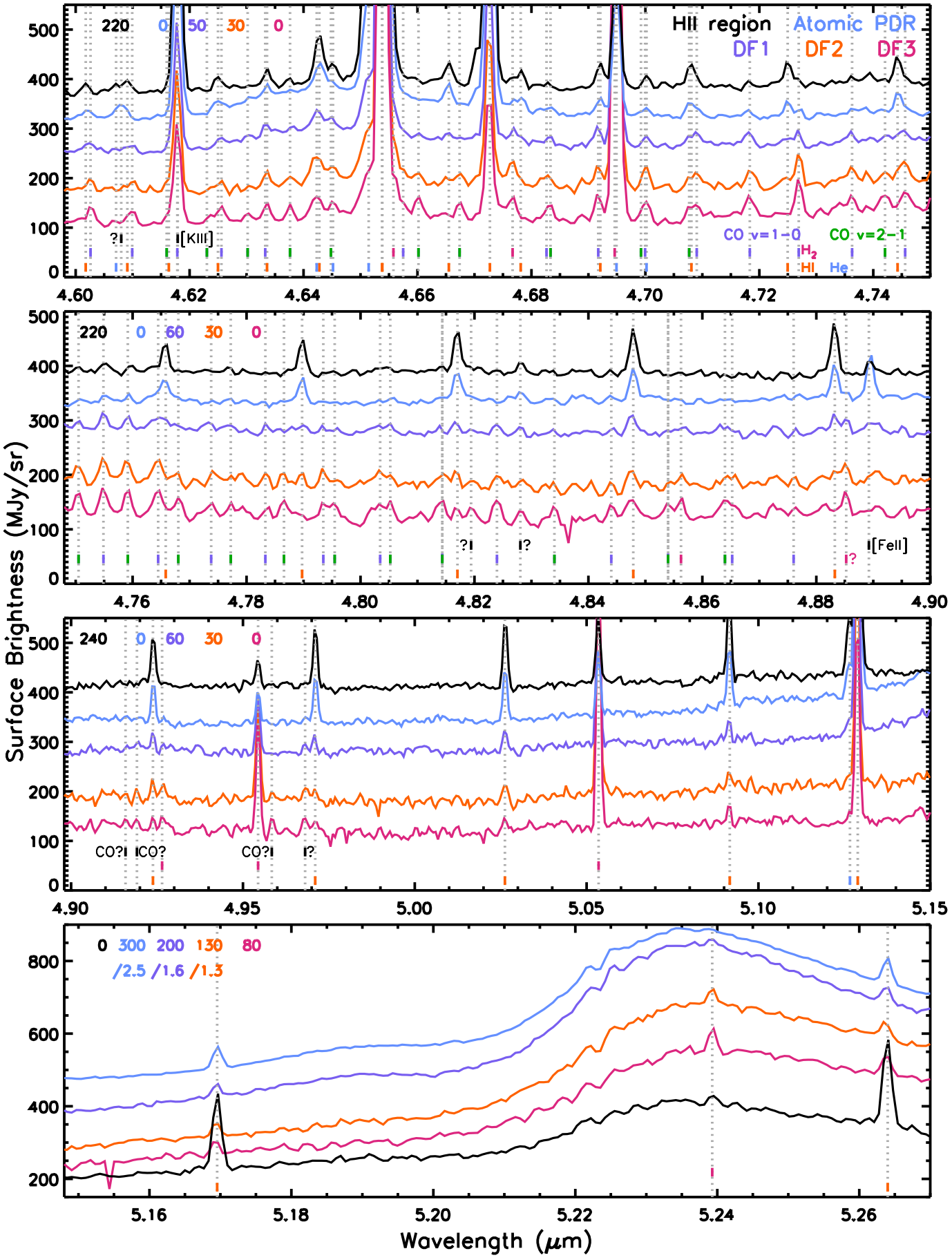

Fig. B.1. continued.

Appendix C: NIR continuum emission

We assess the behaviour of the 3 μm continuum emission by comparing its radial profile with that of Brγ and the total AIB emission (Fig. C.1). We find that the 3 μm continuum emission mimics the total AIB emission much better compared to the Brγ emission implying an origin in stochastically heated very small grains and/or blended overtone and combination bands of PAHs, consistent with previous reports (Sellgren 1984; Allamandola et al. 1989).

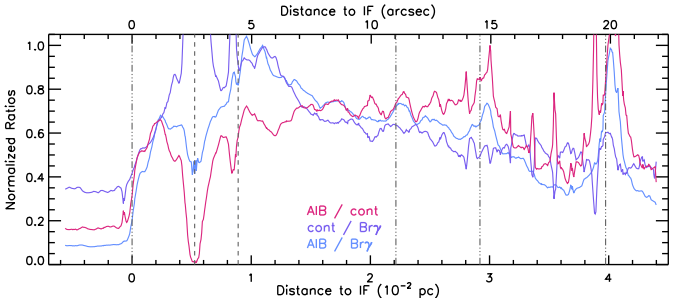

Fig. C.1. Normalised ratios of the 3 μm continuum emission, Brγ emission and total AIB emission as a function of distance to the IF (0.228 pc or 113.4″ from θ^1 Ori C) along a cut crossing the NIRSpec mosaic (see Fig. 1). As the cut is not perpendicular to the IF and distances are given along the cut, a correction factor of cos(19.58°)=0.942 needs to be applied to obtain a perpendicular distance from the IF. No extinction correction is applied. The dash-dot-dot-dot vertical lines indicate the position of the IF, DF 1, DF 2, and DF 3, respectively, from left to right. The dashed vertical lines indicated the location of the proplyds 203-504 (left) and 203-506 (right).

Appendix D: HI recombination lines

The H I recombination lines provide an estimate of the rms density in the ionised gas via:

$$I_\lambda = \frac{hc}{\lambda}\frac{3.086\times10^{18}}{4\pi}\alpha_\lambda^{eff} EM \qquad (\mathrm{erg\,cm^{-2}\,s^{-1}\,sr^{-1}}), \qquad (D.1)$$

with I_λ the intensity of the transition, α_λ^{eff} the effective recombination rate coefficient ($\mathrm{cm^3\,s^{-1}}$) and EM the emission measure ($\mathrm{cm^{-6}\,pc}$). We use α_λ^{eff} from case B recombination theory assuming an electron temperature of 10000 K and an electron density of $n_e = 1000\,\mathrm{cm^{-3}}$ (Hummer & Storey 1987).

Appendix E: [He⁺]/[H⁺] abundance

Based on the He I 1.70 μm and the H I 10-4 emission, Marconi et al. (1998) estimated the [He⁺]/[H⁺] abundance from:

$$\frac{F(\mathrm{He\,I}\,1.70\,\mu\mathrm{m})}{F(\mathrm{H\,I}\,10-4)} = 3.61\frac{[\mathrm{He^+}]}{[\mathrm{H^+}]}, \qquad (E.1)$$

which is based on the model calculations of Smits (1996) and assumes that the He I 1.70 μm is only marginally affected by collisional excitations from the metastable 2^3S state as predicted by Osterbrock et al. (1992).

Appendix F: UV intensity

One can estimate the UV continuum from UV pumped emission lines present in the NIRSpec wavelength range assuming the Bar is viewed at an inclination angle with respect to the line of sight. The O I $3d\,^3D^o - 3p\,^3P$ 1.129 μm and O I $4s\,^3S^o - 3p\,^3P$ 1.317 μm emission result from UV pumping by photons of 1027 and 1040 Å respectively. Hence, their UV intensity can be determined with:

$$I_\nu^{UV} = \frac{4\pi\sin(i)}{Af_b}\frac{\lambda_{\mathrm{IR}}\lambda_{UV}}{cW_\lambda} I(IR) \qquad (\mathrm{erg\,cm^{-2}\,s^{-1}\,Hz^{-1}}), \qquad (F.1)$$

where $I(IR)$ is the observed intensity of the IR line in $\mathrm{erg\,cm^{-2}\,s^{-1}\,sr^{-1}}$, i the inclination of the Bar with respect to the line of sight, W_λ the equivalent width of the UV line, $W_\lambda/\lambda_{UV} = 3.6\times10^{-5}$, f_b the branching ratio or probability of IR emission following a UV photon absorption (see Table 3 and 4 in Walmsley et al. 2000), and A equals 3 for the O I lines as their UV pumping lines are triplets with separation larger than W_λ (Marconi et al. 1998; Walmsley et al. 2000). The N I 1.2292 μm emission is due to both the $3d\,^4P - 3p\,^4S^o$ and $4s\,^4P - 3p\,^4P^o$ transitions and occurs following absorption of UV photons of 953 and 965 Å, respectively. The UV intensity can be estimated in a similar way as for the O I lines, where A equals 1 because its UV pumping lines are a singlet. However, N I has a more complex energy level diagram than O I and, thus, this estimate is less straightforward.

As this fluorescent emission originates from a narrow region in the ionisation front (see Sect. 5), the calculated UV intensity represents the UV radiation emergent from the H II region, where the PDR extinction is negligible. Hence, we only apply a foreground extinction, $exp(-\tau_{f,\lambda})$, with $\tau_{f,\lambda}$ the foreground optical depth as obtained in Sect. 6.1. We adopt an inclination i of 4° (Salgado et al. 2016) and obtain the branching ratio from Walmsley et al. (2000, their tables 3 and 4). Assuming an interstellar radiation field of $1\,G_0 = 1.6\times10^{-3}\,\mathrm{erg\,cm^{-2}\,s^{-1}}$ between 6 and 13.6 eV, corresponding to $8.7\times10^{-19}\,\mathrm{erg\,cm^{-2}\,s^{-1}\,Hz^{-1}}$, the obtained UV line intensity can be converted to a normalised UV intensity, G_0.

Applying this method to the strongest fluorescent line (O I 1.317 μm line; Figs. 10 and 11) and adopting an inclination angle i of 4°, we find that the maximum strength of the FUV radiation field, G_0, ranges between $2.2 - 7.1\times10^4$ across the IF seen in O I 1.317 μm emission (with a median value of 5.9×10^4). Marconi et al. (1998) derived a slightly smaller value for G_0 of 2.6×10^4 from their observations of the near-IR O I fluorescent lines, reflecting a slightly lower 1.317 μm intensity ($\sim1.4\times10^{-4}$ versus a median value of $\sim7.7\times10^{-4}\,\mathrm{erg\,cm^{-2}\,s^{-1}\,sr^{-1}}$ across the IF in our mosaic) measured at a slightly different position. In addition, these authors also adopted a slightly higher extinction value ($A_V = 2$ versus a median value of $A_V \sim 1.64$ here, see Sect. 6.1) and a larger inclination angle i ($\sin(i) = 0.20$ versus 0.07 here).

Appendix G: CI emission lines

The C I emission lines provide the electron temperature, T_e, and gas density, n_H. We detect the forbidden fine-structure lines from $2p\,^1D_2$ to $2p\,^3P_1$ and $2p\,^1D_2$ to $2p\,^3P_2$ at respectively 0.9827 and 0.9854 μm (Fig. B.1). We do not detect the third fine-structure line from $2p\,^1D_2$ to $2p\,^3P_0$ that has a much smaller A value. In addition, we detect the multiplets $3s\,^3P^0$ to $3p\,^3D$ at 1.0696 μm and $3p\,^3D$ to $3d\,^3F^0$ at 1.1759 μm (Fig. B.1; for wavelengths and transition probabilities, see Walmsley et al. 2000).

The observed line intensities for the templates are given in Table G.1. The C I emission in the H II region template likely originates from the background face-on PDR, whereas the C I

Table G.1. C I intensities for the five template spectra.

Wavelength (1)	$I_{Obs.}$ (2)	$g(\tau_{p,\lambda}, \tau_{f,\lambda})$ (3)	$I_{corr.}$ (4)
	H II region		
0.984	1.05±0.02	0.170	6.20±0.11
1.0696	0.28±0.02	0.203	1.41±0.12
1.1759	0.23±0.04	0.248	0.94±0.14
1.0696/1.1759	1.22±0.21		1.50±0.26
0.984/1.0696	3.69±0.32		4.41±0.38
	atomic PDR		
0.984	1.32±0.02	0.083	15.81±0.24
1.0696	0.37±0.03	0.101	3.68±0.28
1.1759	0.41±0.02	0.128	3.23±0.18
1.0696/1.1759	0.90±0.08		1.14±0.11
0.984/1.0696	3.53±0.27		4.30±0.33
	DF 1		
0.984	0.88±0.01	0.202	4.35±0.07
1.0696	0.22±0.04	0.237	0.93±0.18
1.1759	0.30±0.04	0.284	1.07±0.15
1.0696/1.1759	0.73±0.18		0.87±0.21
0.984/1.0696	3.99±0.77		4.67±0.90
	DF 2		
0.984	1.13±0.02	0.201	5.63±0.09
1.0696	0.20±0.03	0.236	0.86±0.12
1.1759	0.26±0.04	0.283	0.92±0.15
1.0696/1.1759	0.78±0.17		0.93±0.20
0.984/1.0696	5.60±0.80		6.56±0.94
	DF 3		
0.984	1.75±0.02	0.184	9.53±0.10
1.0696	0.34±0.02	0.217	1.56±0.09
1.1759	0.21±0.05	0.264	0.79±0.17
1.0696/1.1759	1.63±0.37		1.98±0.45
0.984/1.0696	5.15±0.31		6.09±0.36

Notes. Columns: (1) wavelength (μm). The 0.984 intensity is the sum of the 0.9827 and 0.9854 μm line intensities, the 1.0696 intensity is the sum of the 1.0687 and 1.0695 μm line intensities and the 1.1759 intensity is the sum of the 1.1752 and 1.1758 μm line intensities.; (2) observed intensity (10^{-4} erg cm^{-2} s^{-1} sr^{-1}); (3) $g(\tau_{p,\lambda}, \tau_{f,\lambda})$ as defined in Eq. G.1; (4) extinction corrected intensity (10^{-4} erg cm^{-2} s^{-1} sr^{-1}).

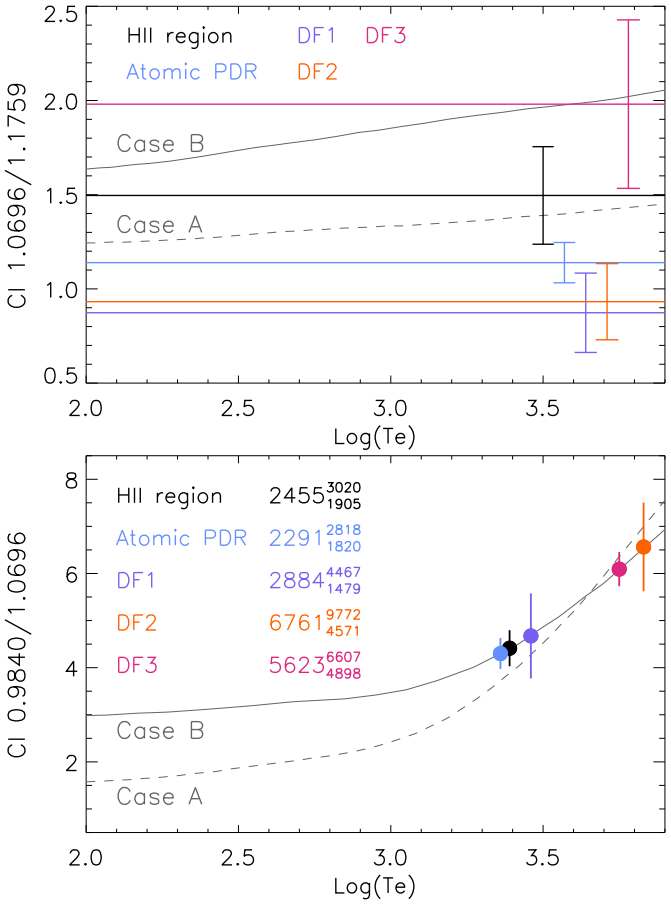

Fig. G.1. Comparison of extinction-corrected C I line ratios with computed ratios taken from Walmsley et al. (2000) that are based on calculations of Escalante & Victor (1990) for both case A and case B recombination theory. Uncertainties on the observed ratios are given by vertical lines that are placed at the derived electron temperature (lower panel) or in the [3.5 – 3.8] x-range (top panel).

emission in the atomic PDR template originates in the edge-on PDR and in the H_2 dissociation front templates it originates in the face-on PDR (see also the discussion in Sect. 5). We adopt an internal extinction of $A_V = 4$ and $A_V = 10$ for, respectively, a face-on and edge-on PDR and apply the foreground extinction derived in Sect. 6.1. The resulting extinction corresponds to:

$$g(\tau_{p,\lambda}, \tau_{f,\lambda}) = exp(-\tau_{f,\lambda}) \frac{1 - exp(-\tau_{p,\lambda})}{\tau_{p,\lambda}}, \quad \text{(G.1)}$$

with $\tau_{p,\lambda}$ and $\tau_{f,\lambda}$ the PDR and foreground optical depths at the wavelength λ, respectively.

The 1.0696/1.1759 line ratio depends primarily on the optical depth of the UV pumping line (Walmsley et al. 2000, their Fig. 14). We compare the observed intensities with their model calculations (Fig. G.1). We find that the extinction corrected 1.0696/1.1759 line ratio indicates case A conditions for the atomic PDR and case B conditions for DF 3. The ratio for the H II region can be consistent with either case A or B whereas the ratio falls below the theoretical curves for case A and B conditions for DF 1 and DF 2. Walmsley et al. (2000) also reported case A conditions based on their observations (not extinction corrected). To investigate this further, we calculate the optical depth of a resonance line (for example 1261 Å line) following Tielens (2021, eq. 4.29) assuming a typical line width of $\Delta v_{FWHM} = 3$ km/s and a neutral carbon fraction of 10^{-5}. The latter was determined using Eq. 9.6 in Tielens (2005) assuming a temperature of 1000 K, a UV radiation field G_0 of 10^4, a density of 3×10^6cm^{-3}, and a visual extinction A_V of 0. We evaluate the optical depth for two scenarios: one adopting a density $n_H = 10^5$ cm^{-3} and a line of sight depth of $L = l^{los}_{PDR} = 0.10$ pc (Sect. 6.3.2), typical values for the Bar, and one adopting a density $n_H = 10^7$ cm^{-3} and a line of sight depth of $L = 10^{-3}$ pc (e.g. Joblin et al. 2018; Goicoechea et al. 2016), typical values for dense clumps reported in the Bar. In both cases we find that the resonance line is optically thick, suggesting case B conditions. The origin of the discrepancy with the result of the 1.0696/1.1759 line ratio will be investigated in a follow-up paper. For the remainder of this analysis, we assume case B conditions.

The (0.983+0.985)/1.0696 line ratio depends primarily on the electron temperature (Walmsley et al. 2000, their Fig. 14). Adopting case B conditions, the extinction corrected line ratio corresponds to electron temperatures of approximately 2500, 2300, 2900, 6800, 5600 for the H II region, the atomic PDR,

DF 1, DF 2, and DF 3 templates respectively (Fig. G.1). Given the uncertainty in the line ratio, the derived temperatures for the H II region, the atomic PDR, and DF 1 templates are consistent with each other. Likewise, the obtained temperature for the DF 2 and DF 3 templates are consistent within their uncertainty and are surprisingly high, similar to the electron temperature of around 4700 K obtained by Walmsley et al. (2000) without correcting for extinction. No combination of foreground extinction (0-2 magn.) and internal extinction (0-15 magn.) results in an electron temperature below 1000 K for the DF 3 template (with the lowest obtained T being ~3800 K for case B).

Lastly, we can obtain an estimate of the density from the [C I] 0.984 μm intensity that is the sum of the [C I] 0.982 and 0.985 μm intensities (Walmsley et al. 2000, Eq. 2):

$$I(0.984) = I_0\, T_3^{-0.6}\, EM\, g(\tau_{p,\lambda}, \tau_{f,\lambda}) \quad (\mathrm{erg\,cm^{-2}\,s^{-1}\,sr^{-1}}), \quad \text{(G.2)}$$

with $I_0 = 6 \times 10^{-7}$ for case B (2.7×10^{-7} for case A), $T_3 = T/1000$ K, EM the carbon emission measure in $\mathrm{pc\,cm^{-6}}$ with $\mathrm{EM} = \int n_e n_{C^+} ds$. As the C I emission arises from a very thin layer of a few thousand degree gas (Sect. 6.5), we adopt A_V of 0.5 for this layer (i.e. $N = 1 \times 10^{21} \mathrm{cm^{-2}}$). Assuming all C is ionised, a C gas phase abundance of 1.6×10^{-4}, case B conditions, Eq. G.2 can be written as:

$$I(0.984) = 2.6 \times 10^{-5} \left(\frac{3000\,\mathrm{K}}{T}\right)^{0.6} \left(\frac{n}{1 \times 10^7 \mathrm{cm^{-3}}}\right) \quad (\mathrm{erg\,cm^{-2}\,s^{-1}\,sr^{-1}}). \quad \text{(G.3)}$$

For the derived foreground extinction (Sect. 6.1), we obtain an extinction correction factor $g(\tau_{p,\lambda}, \tau_{f,\lambda})$ of 0.170, 0.083, 0.202, 0.201, 0.184 for respectively the H II region, atomic PDR, DF 1, DF 2, and DF 3 templates. This is considerably smaller than the value of ~0.3 used by Walmsley et al. (2000) who adopt $A_V = 1.5$ for the PDR extinction. We obtain an emission measure $\mathrm{EM} = A\, T_3^{0.6}$, with A being 1034±18, 2635±40, 725±11, 938±15, and 1589±17 ($\mathrm{cm^{-6}\,pc\ K^{-0.6}}$), respectively, for each of the five templates. Combined with the derived temperature, this results in an emission measure EM of 1772^{+247}_{-240}, 4334^{+602}_{-539}, 1370^{+451}_{-401}, 2953^{+790}_{-576}, 4477^{+472}_{-350} $\mathrm{cm^{-6}\,pc}$ respectively. This results in a gas density, n_H, of 2.1, 5.2, 1.6, 3.5, and $5.3 \times 10^8\ \mathrm{cm^{-3}}$ for respectively, the H II region, the atomic PDR, DF 1, DF 2, and DF 3 templates.

Appendix H: AIB emission

Appendix H.1: AIB decomposition

We have performed two spectral decompositions of the AIB emission, which are applied to every pixel of the NIRSpec mosaic and to the five template spectra. First, we employ an updated version of PAHFIT (Smith et al. 2007)[33]. In PAHFIT-based models, the AIBs are represented using Drude profiles for simplicity[34]. The continuum is fitted to the entire F290LP range (2.87–5.27 μm) using a superposition of fixed-temperature blackbody emission components and the emission lines (see Sect. 4.1) are fitted using Gaussian profiles with a FWHM that is determined by the resolution curve of F290LP. The AIB emission in the NIRSpec range is decomposed into seven components, their peak position and FWHM are listed in Table H.1. The obtained fit reproduces the observations very well (Fig. 16). The component near 3.23 μm cannot be fitted because the blue wing of the 3.29 μm feature is not reproduced well by a single Drude component (the PAHFIT model overestimates the AIB emission shortwards of 3.25 μm). On the other hand, the Drude profiles can reproduce the overlap region between the 3.29 and 3.4 μm AIBs without the requirement for an extra plateau-like component. The 3.4 μm AIB consists of two components with different widths, referred to as the '3.39' and '3.40' components. The AIB

[33] available at https://github.com/PAHFIT. We note that PAHFIT fit the spectrum expressed in μm vs. MJy/sr.

[34] An isolated harmonic oscillator would give a Lorentz profile while an electron gas without restoring force would give a Drude profile.

Table H.1. Fitting parameters used in the decomposition of the AIB emission.

PAHFIT			Gaussian decomposition		
Band	Position	FWHM	Band	Position	FWHM
(1)	(2)	(3)	(4)	(5)	(6)
3.23	3.23	0.026	3.25	3.2465	0.0375
3.29	3.291	0.03762	3.29	3.29027	0.0387
			3.33	3.32821	0.0264
3.39	3.395	0.00995	3.39	3.3944	0.0076
3.40	3.405	0.02691	3.40	3.4031	0.0216
3.42	3.4253	0.015	3.42	3.4242	0.0139
3.46	3.464	0.07012	3.46	3.4649	0.0500
3.51	3.516	0.0271	3.51	3.5164	0.0224
3.56	3.561	0.02	3.56	3.5609	0.0352
			plateau	3.4013	0.2438

Notes. Columns: (1)-(3) PAHFIT decomposition; (4)-(6) Gaussian decomposition; (1) AIB name; (2) peak position (μm); (3) FWHM (μm); (4) AIB name; (5) peak position (μm); (6) FWHM (μm).

Table H.2. Integrated intensities of the AIB components in the five template spectra (10^{-3} erg cm^{-2} s^{-1} sr^{-1}).

Band	H II region	Atomic PDR	DF 1	DF 2	DF 3
PAHFIT					
3.23	0	0	0	0	0
3.29	10.58	45.27	30.43	24.09	15.50
3.39	0.30	1.59	1.05	0.78	0.47
3.40	1.01	3.21	2.86	3.35	2.73
3.42	0.15	0.51	0.32	0.33	0.25
3.46	1.61	6.94	5.16	4.79	3.71
3.51	0.39	1.93	1.43	1.28	1.08
3.56	0.14	0.64	0.53	0.45	0
Gaussian decomposition					
3.25	0.85	3.48	2.23	1.71	1.24
3.29	6.46	28.63	18.84	14.50	9.31
3.33	0.32	1.44	1.00	0.60	0.37
3.39	0.08	0.63	0.37	0.25	0.15
3.40	0.51	1.53	1.42	1.60	1.27
3.42	0.09	0.25	0.18	0.24	0.20
3.46	0.27	1.06	0.84	0.75	0.60
3.51	0.14	0.71	0.50	0.44	0.35
3.56	0.06	0.21	0.17	0.09	0.08
plat	3.89	16.60	11.46	11.00	8.30
Deuterated PAHs[(a)]					
4.64	0.10	0.35	0.22	0.09	0.05
4.75	0.04	0.05	0.09	0.08	0.06

Notes. [(a)]See Appendix H.2 for details on the flux estimates.

emission at wavelengths longer than 3.4 μm consists of a very broadband at 3.46 μm, with two narrower bands at 3.42 μm and 3.51 μm. There is also a noticeable weaker and broad feature at 3.56 μm, but just like the wing on the blue side of 3.29 μm, the wing on the red side of the 3.51 μm band is not fitted as well. The width and power of 3.56 μm AIB were therefore harder to determine. Second, we have employed a Gaussian decomposition of the AIB emission in the 3.2 to 3.7 μm region after subtracting a linear dust continuum emission (determined in the [2.97, 3.03] and [3.65, 3.720] μm wavelength ranges)[35]. Narrow emission lines were removed prior to fitting. We fitted the AIB emission with ten Gaussians that were highly constrained in peak position and FWHM (±0.0005 and ±0.001, respectively; Table H.1). The resulting fit reproduces the observations very well (Fig. 16). We point out that in contrast to the PAHFIT method, one Gaussian represents the underlying plateau emission and one Gaussian represents the extended red wing of the 3.29 μm AIB. The remaining components are comparable between both decomposition methods. The integrated intensity of the AIB components in the five templates for both decomposition methods are given in Table H.2.

Appendix H.2: Deuterated PAHs

While an emission band at 4.646 μm is clearly visible in the H II region, the atomic PDR, and DF 1 templates (Fig. 6), we here investigate its potential presence in the DF 2 and DF 3 templates. This is severely hampered by the detection of gas-phase CO emission in the molecular PDR (Sect. 4.1) which coincides in wavelength with the potential 4.646 μm band. We therefore fit the DF 3 template with an optically thin and optically thick LTE model of ^{12}CO and ^{13}CO to assess whether the 4.6 – 4.8 μm emission (in addition to the continuum emission) can be solely due to CO emission. The optically thin model does not provide a good fit to the data whereas the optically thick model provides a better fit to the data in terms of both the relative intensities and the density of lines. While the CO emission clearly requires more advanced modelling, this simple exercise suggests that the 4.62 – 4.68 μm and 4.71 – 4.79 μm range has additional broadband emission that is not reproduced by the CO models. Next, we extract the (asymmetric) 4.646 μm band profile from the atomic PDR template where the band is strongest. We then scale this 4.646 μm band profile to match the emission in the other templates (Fig. H.1). Given the presence of numerous emission lines in this wavelength range and the uncertainty on the continuum determination, this provides an approximate estimate of its intensity in the five templates which is an upper limit for those templates with strong CO emission. The derived intensities are given in Table H.2. We note that within the uncertainties, the band profile does not vary between the templates.

As the CO model also indicated additional emission in the 4.71 – 4.79 μm range, we applied the same method here to derive rough estimates of this broadband's intensity. In this case, we extract the band profile in the DF 1 template where it is strongest. Similar as for the 4.646 μm band, this 4.746 μm band profile is also asymmetric and, when scaled, matches the observations in all templates, albeit it is relatively very weak in the H II region and atomic PDR templates. For completeness, we give the approximate intensities of this band in Table H.2.

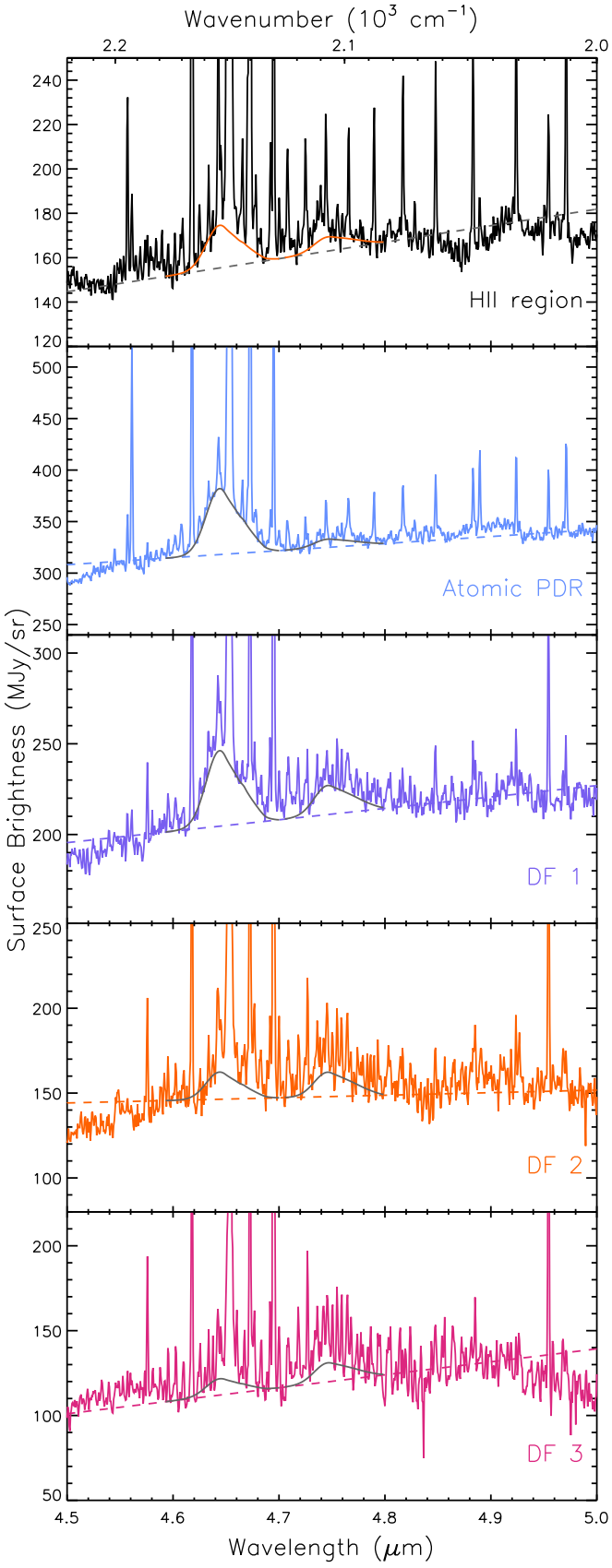

Fig. H.1. Tentative 4.644 and 4.746 μm dust features attributed to deuterated PAHs (Sect. 4.1). Local linear continua are shown by the dashed lines. The 4.646 and 4.746 μm bands are plotted on top of the continuum as a solid line. The same band profile for each feature is used for all templates. See Appendix H.2 for details.

[35] We fitted the spectrum expressed in μm vs. W m^{-2} μm^{-1} sr^{-1}.